Nuclear Spin Dynamics Under Above-Bandgap Optical Pumping in Silicon

by

Rahul Deshpande

A thesis
presented to the University of Waterloo
in fulfillment of the
thesis requirement for the degree of
Doctor of Philosophy
in
Physics (Quantum Information)

Waterloo, Ontario, Canada, 2021

© Rahul Deshpande 2021

Examining Committee Membership

The following served on the Examining Committee for this thesis. The decision of the Examining Committee is by majority vote.

External Examiner	NAME Title	Dr. Andrea Morello Professor, University of New South Wales
Supervisor(s)	NAME Title	Dr. David G Cory Professor, Department of Chemistry, University of Waterloo
Internal Member	NAME Title	Dr. Raffi Budakian Professor, Department of Physics, University of Waterloo
Internal-external Member	NAME Title	Dr. Joseph Emerson Associate Professor, Department of Applied Mathematics, University of Waterloo
Other Member(s)	NAME Title	Dr. Jonathan Baugh Associate Professor, Department of Chemistry, University of Waterloo

Author's Declaration

I hereby declare that I am the sole author of this thesis. This is a true copy of the thesis, including any required final revisions, as accepted by my examiners.

I understand that my thesis may be made electronically available to the public.

Abstract

Phosphorus defects in silicon have been proposed as candidates for quantum information and quantum sensing applications, with proposals utilizing both the donor electron spin as well as the ^{31}P nuclear spin. Initialization of the nuclear spin in its ground state (hyperpolarization) is essential for these applications. Silicon also has a spin-1/2 isotope (^{29}Si) with 4.7% abundance. ^{29}Si nuclear spins have long spin-lattice relaxation times compared to experimental timescales, providing a thermally isolated system whose effective temperature (polarization) can be controlled. This can serve as a test-bed for studying central spin effects and other many-body experiments. However, spin-spin interactions are relatively weak, requiring lower spin temperatures (hyperpolarization) than have been previously achieved in bulk silicon in order to see collective effects. Optical pumping with above-bandgap light (1047 nm) has been shown to drive hyperpolarization processes on the ^{31}P as well as ^{29}Si nuclear spins in lightly doped silicon ($\sim 10^{15}$ cm^{-3}). There are various proposals for the mechanisms driving these processes, some conflicting, with very little experimental confirmation.

In the first part of this thesis, we demonstrate that the ^{31}P nuclear spin hyperpolarization in isotopically enriched ^{28}Si is generated by a phononic cross-relaxation process, which is accelerated and driven by the optical pumping to a different effective temperature compared to the electron spin relaxation (T_1) process . We propose an experiment to hyperpolarize the ^{31}P nuclear spins faster using AC electric fields. In addition to identifying the hyperpolarization process, we use the change in the resonance frequency of the ^{31}P nuclear spin under an Auger recombination driven ionization process to measure the rates of ionization and photoneutralization of the defect site in the presence of above-bandgap light. The method is an example of NMR under chemical exchange. We find a paramagnetic shift on ^{31}P nuclear spins in the ionized defect (D^+) state, which has not been reported previously.

In the second half of the thesis, we investigate the polarization buildup of ^{31}P and ^{29}Si nuclear spins in natural abundance silicon. We demonstrate that the ^{29}Si polarization originates from the ^{31}P defect sites, in a many-body effect where nearby (core) ^{29}Si are

polarized by a cross-relaxation process similar to that driving the ^{31}P polarization, followed by spin diffusion to the rest (bulk) of the ^{29}Si spins. We also experimentally confirm the existence of a ^{31}P - ^{29}Si resonant matching field condition at 6.7 T, where the heteronuclear dipole-dipole interaction is able to exchange polarization efficiently in the excited state manifold of the electron spin, and demonstrate its dependence on the laser power as well as its effect on the ^{31}P nuclear spin polarization. We model the system using quantum simulations on small model spin systems, as well as with simplified rate equations, and show that the rate limiting step is the buildup of polarization of the nearby (core) ^{29}Si spins. We use our knowledge of the defect ionization rates to establish a lower bound on the spin diffusion rate across the diffusion barrier at the defect site, and verify that the data is consistent with these lower bounds. The insights provided by our results suggest future experiments to create highly polarized ^{29}Si ensembles. This might serve as a test-bed for central spin effects and other many-body experiments.

Acknowledgements

This thesis is the product of a long journey, and would not have been possible without the love and support of my family, friends and colleagues.

First, I would like to thank my supervisor, Prof. David Cory, for his guidance, patience and support over the years, without which I would not have had the chance to work on a diverse set of interesting projects. I would also like to offer my thanks to all the members of Cory group that I've had the pleasure of working with. To Troy Borneman and Chris Granade, for helping me settle into life in the group and in Waterloo. The learning process as a new student would have been a lot harder without your help. To Holger Haas and Thomas Alexander, for the days and nights spent on the silicon project, running experiments and building helium lamps. A special thanks to Holger, for countless fruitful discussions and for feedback on this thesis. To George Nichols, for solving every problem I ever had in the lab, and teaching me cryogenics. To Yonatan Hovav, for making the last year of experiments so much more enjoyable, and for your efficiency and enthusiasm in pursuing new ideas. To Alex Mitrovich, Peter Sprenger and Don Carkner, for all your help with machining, electronics and infrastructure respectively. To Razieh Annabestani, Ian Hincks and Mohamad Niknam, for helpful discussions. To Carly, Sara and Heidi, for excellent administrative support. To Julia, Madelaine, Dima, Saba, Zimeng and everyone else, who made the lab a great place to work in.

Life in Waterloo has been wonderful thanks to Julia, Manjit, Aditya, Nikhil, Irene, Nachi, Idhaya, Bipin, Vadiraj, Jeremy, Anand and many others - I consider myself very lucky to have you in my life. And finally, a shout out to Troy, Jakub, Diana, Lemon, Katie, the rest of the Chainsaw crew and Mike Todd, for the best Wednesday nights.

Dedication

To my parents, who made sure that I had all the love and support I needed, despite the hardships they had to face.

Table of Contents

List of Figures

List of Tables

Chapter 1

Introduction

Magnetic resonance utilizes the sensitivity of electron and nuclear spins as a probe into their local environment. It has found a wide variety of applications in physics, chemistry, biology, medical imaging as well as engineering applications, such as in the petroleum industry. New frontiers that have attracted considerable interest are applications towards quantum information and quantum sensing. In particular, defects spins in silicon are considered a promising platform for quantum computing. Silicon provides a clean, controllable magnetic environment, and has the potential to scale up faster by leveraging the expertise developed over decades of research by the semiconductor industry. ^{31}P defect nuclear spins in isotopically enriched ^{28}Si have achieved some of the longest coherence and relaxation times to date in bulk [1] as well as single spin [2] measurements. ^{29}Si spins in silicon also have extremely long relaxation times, even at room temperatures. Nuclear spins with long coherence times may also be used for quantum sensing applications, for e.g. as gyroscopes [3] and magnetometers. However, the long relaxation times and relatively weak coupling of nuclear spins to the environment also present a challenge for initializing them on-demand in a pure state, which increases the sensitivity for sensing applications and is critical for quantum information applications. In magnetic resonance terminology, this is equivalent to generating a near-unity hyperpolarization.

Optical pumping with above-bandgap (1047 nm) light at low temperatures and high magnetic fields has been shown to drive the hyperpolarization of ^{31}P [4] and ^{29}Si nuclear spins [5] in silicon. In this thesis, we develop a framework for understanding the mechanisms driving these hyperpolarization processes, and provide experimental evidence with inductively detected Nuclear Magnetic Resonance (NMR) measurements. Through our experiments, we also demonstrate the use of NMR in probing defect ionization and pho-

toneutralization rates, as well as in measuring small changes in hydrostatic strain through a corresponding linear variation in the hyperfine interaction [6].

1.1 Outline

This section contains an outline of the thesis, along with a statement of contributions.

- The rest of this chapter provides a brief introduction to key concepts such as the fundamentals of NMR, the interaction picture, Bloch equations and infinitesimal strain theory.
- Ch. 2 introduces phosphorus-doped silicon, the wavefunction of the defect electron and its dependence on strain.
- Ch. 3 explores properties of the defect electron spin as well as the ^{29}Si and ^{31}P nuclear spins which are relevant to this thesis.
- Ch. 4 provides a detailed description of the experimental setup as well as data acquisition and processing techniques.
- Ch. 5 explores the process leading to ^{31}P hyperpolarization under above-bandgap optical pumping at low temperatures [4, 7]. We also demonstrate a technique that uses NMR for probing the defect ionization rates, which are driven by the bound exciton formation and recombination process. In order to do this, we use methods developed for studying chemical reaction rates with NMR [8]. The work in this chapter was done in collaboration with Holger Haas and Thomas Alexander.
- Ch. 6 explores the process leading to ^{29}Si polarization under above-bandgap optical pumping. The interplay between the defect electron spin, ^{31}P and ^{29}Si spins is examined in detail, with a theoretical model as well as experimental verification. The work in this chapter was done in collaboration with Yonatan Hovav.
- Ch. 7 explores the hydrostatic strain dependence of the ^{31}P hyperfine interaction.

1.2 Basics of Magnetic Resonance

The fundamental idea behind magnetic resonance is to use an oscillating magnetic field to excite and detect spin transitions. The nuclear and electron spin ensemble has an associated

magnetic dipole moment $\vec{\mu} = \gamma\vec{S}$, where $\vec{S}$ is the spin angular momentum operator and γ is the gyromagnetic ratio, whose value depends on the spin species. In this thesis, we look at the phosphorus donor electron spin as well as phosphorus (^{31}P) and silicon (^{29}Si) nuclear spins. Their gyromagnetic ratios are given by $\gamma_e = 2\pi \times 28,024.951$ MHz/T, $\gamma_P = 2\pi \times 17.235$ MHz/T and $\gamma_{Si} = -2\pi \times 8.465$ MHz/T respectively. In the presence of an applied magnetic field $\vec{B}$, the Hamiltonian is [9]

$$H = -\vec{\mu}.\vec{B} \ . \tag{1.1}$$

The spin angular momentum operator $\vec{S}$ for an ensemble of N spin-1/2 can be written as

$$\vec{S} = \sum_{i=1}^{N} \frac{\hbar}{2}\vec{\sigma}^i \ .$$

Here and for the rest of the thesis, the superscript labels the specific spin subspaces the operator acts on, assuming an identity on the rest of the Hilbert space. For example, $A^i = \mathbb{1}^{\otimes i-1} \otimes A \otimes \mathbb{1}^{\otimes N-i}$ and $A^iB^j = \mathbb{1}^{\otimes i-1} \otimes A \otimes \mathbb{1}^{\otimes j-i-1} \otimes B \otimes \mathbb{1}^{\otimes N-j}$. Therefore, $\vec{\sigma}^i = \mathbb{1}^{\otimes i-1} \otimes \vec{\sigma} \otimes \mathbb{1}^{\otimes N-i}$, where $\vec{\sigma}$ are the Pauli matrices, given by

$$\sigma_x = \begin{pmatrix} 0 & 1 \\ 1 & 0 \end{pmatrix}, \qquad \sigma_y = \begin{pmatrix} 0 & i \\ -i & 0 \end{pmatrix}, \qquad \sigma_z = \begin{pmatrix} 1 & 0 \\ 0 & -1 \end{pmatrix}.$$

As a choice of convention, the static magnetic field will be considered to be along the z-axis ($\vec{B}_0 = B_0\,\hat{z}$), and we set $\hbar = 1$, such that Hamiltonians are in units of angular velocity. Therefore, the Hamiltonian for the ensemble is

$$H = \omega S_z \ , \tag{1.2}$$

where $\omega = \gamma B_0$ is the Larmor precession frequency. Here, we have assumed that the field is homogeneous over the ensemble, such that all spins have the same ω. This is not true in general, and leads to inhomogeneous broadening of the lineshape in ensemble measurements. The evolution of the spin wavefunction is given by the Schrödinger equation

$$\frac{d\,|\psi\rangle}{dt} = -iH\,|\psi\rangle \ . \tag{1.3}$$

In the absence of any other terms in the Hamiltonian, the thermal equilibrium state at temperature T is given by the density matrix

$$\begin{aligned} \rho_T &= \frac{\exp\left(-\beta H\right)}{\mathrm{Tr}(\exp\left(-\beta H\right))} \\ &= \frac{\mathbb{1}^{\otimes N}}{2^N} + \frac{p_T}{2^N}\sum_{i=1}^{N}\sigma_z^i + \frac{p_T^2}{2^N}\sum_{i\neq j}\sigma_z^i\sigma_z^j + ... \\ &= \left(\frac{\mathbb{1} + p_T\sigma_z}{2}\right)^{\otimes N} \ , \end{aligned} \tag{1.4}$$

where $p_T = \tanh\left(\frac{\beta\omega}{2}\right)$, $\beta^{-1} = k_B T$ and $k_B = 2\pi \times 20,837$ MHz K^{-1} is the Boltzmann constant. The expectation value of the angular momentum $\langle S_z \rangle$ of the thermal equilibrium state is Np_T, and p_T is called the thermal polarization. In typical static field values of $\sim 5 - 10$ T, the Hamiltonian term $|H|$ is hundreds of MHz or lower for nuclear spins. This corresponds to a low thermal polarization ($p_T \simeq 10^{-6}$ at 300 K). This leads to a small signal and low sensitivity for inductive detection, as well as poor initialization for quantum information applications. In order to overcome these issues, a wide range of hyperpolarization methods, such as dynamic nuclear polarization (DNP), have been developed. When the spin is in a state with an effective polarization $|\langle S_z \rangle| > N|p_T|$, it is referred to as hyperpolarized. The terms of the density matrix of order p_T^2 and higher are negligible at high temperature thermal polarization values, but become relevant in hyperpolarized systems.

1.2.1 Interaction Picture and Rotating Wave Approximation

The spin state is controlled by applying a time dependent magnetic field B_1 perpendicular to the static field B_0, with an oscillation frequency ω_c. The Hamiltonian is

$$H = \omega S_z + 2\Omega \cos(\omega_c t + \phi) S_x \ , \tag{1.5}$$

where $\Omega = \frac{\gamma B_1}{2}$ is the Rabi frequency and the x-axis is determined by the direction of B_1 as a choice of convention. It is helpful to introduce an interaction picture, where $|\psi'\rangle = \exp(-iH_0 t)|\psi\rangle$. The Schrödinger equation in Eq. 1.3 can now be rewritten as

$$\frac{d|\psi'\rangle}{dt} = -iH'|\psi'\rangle \ , \tag{1.6}$$

where H' is the effective Hamiltonian, given by

$$H' = \exp(iH_0 t) H \exp(-iH_0 t) - H_0 \ . \tag{1.7}$$

This transformation is referred to as going into the interaction frame/rotating frame of H_0. In the case of Eq. 1.5, with $H_0 = \omega_c S_z$, the effective Hamiltonian is

$$H' = \Delta \ S_z + (1 + e^{2i\omega_c t})\Omega (\cos\phi \ S_x + \sin\phi \ S_y) \ , \tag{1.8}$$

where $\Delta = \omega - \omega_c$. The rotating wave approximation (RWA) neglects the oscillating terms, which is justified if it has a frequency much greater than its amplitude. This is typically true in NMR, where the static field is three orders of magnitude stronger than the control fields. The effective Hamiltonian is now given by

$$H' = \Delta \ S_z + \Omega (\cos\phi \ S_x + \sin\phi \ S_y) \ . \tag{1.9}$$

By applying the control field at or close to the resonance frequency ($\Delta \leq \Omega$) for an appropriate duration t_p and phase ϕ, we can generate a unitary of the form $\exp(i\theta S_j)$. In NMR literature, the notation $\theta)_j$ is commonly used as a short hand for this unitary, indicating a rotation by an angle θ about the j-axis.

1.2.2 Measurement Operators

There are multiple ways of describing the measurement in NMR, semiclassical [9, 10] as well as quantum [11, 12]. Here, we present a simplified, semi-classical description.

The Hamiltonian in Eq. 1.2 results in the Larmor precession of the magnetic dipole moment about the z-axis with frequency ω. The oscillating magnetic field produced by this precessing magnetic moment induces a voltage across the coil. This voltage is amplified by the detection circuit. The signal is mixed with two reference signals (phase shifted by 90° from each other) for phase-sensitive detection in the spectrometer receiver. By sharing a reference between the transmitter which generates the control field B_1 and the receiver, and down mixing with the transmitter frequency ω_c, the measurement is performed in the same rotating frame as that of Eq. 1.9.

Since N is large ($> 10^{13}$) in bulk NMR samples, the magnetization of the ensemble of identical spins is proportional to the expectation value of the individual spin angular momentum operator. Therefore, the observed signal is

$$\mathrm{S}(t) \propto \langle \sigma_+ \rangle \ ,$$

where $\langle \sigma_+ \rangle = \mathrm{Tr}(\rho(t)\sigma_+)$ and the density matrix ρ is given by the evolution of the single spin-1/2 Hamiltonian in the rotating frame of $H_0 = \frac{\omega_c}{2}\sigma_z$.

1.2.3 Lindblad Equation for Open Systems

To include Markovian noise processes, we use the Lindblad master equation [13], given by

$$\frac{d\rho}{dt} = -i[H, \rho] + \sum_j \left(L_j \rho L_j^\dagger - \frac{1}{2}\{L_j^\dagger L_j, \rho\} \right) \ , \tag{1.10}$$

where L_j are Lindblad operators corresponding to various noise processes.

The form of Eq. 1.10 is not a homogenous differential equation, unlike the Schrödinger equation. This makes it difficult to write a general solution for all ρ as a single matrix operator, analogous to the unitary operator for closed systems. However, this can be achieved by writing the equation in the Liouville space. This involves writing the $D \times D$ density matrix as a vector $\mathrm{vec}(\rho)$ of length D^2, stacking successive columns one below the other. In this case, Roth's lemma [14] states that $\mathrm{vec}(ABC) = (C^{\mathsf{T}} \otimes A).\mathrm{vec}(B)$, allowing us to write the master equation as

$$\frac{d}{dt}\mathrm{vec}(\rho) = \mathcal{L} \cdot \mathrm{vec}(\rho) \ . \tag{1.11}$$

Here, $\mathcal{L}$ is the Liouville superoperator, given by

$$\mathcal{L} = -i\left(\mathbb{1} \otimes H - H^{\mathsf{T}} \otimes \mathbb{1}\right) + \frac{1}{2}\sum_j \left(2L_j^* \otimes L_j - \mathbb{1} \otimes L_j^\dagger L_j + L_j^{\mathsf{T}} L_j^* \otimes \mathbb{1}\right) \ . \tag{1.12}$$

The time evolution given any initial state can now be calculated as

$$\mathrm{vec}(\rho(t)) = \exp\left(\mathcal{L}t\right) \cdot \mathrm{vec}(\rho(0))$$

for a time-independent $\mathcal{L}$.

1.2.4 Bloch Equations

The Lindblad master equation is applicable for all quantum mechanical systems with a Markovian noise process. In this section, we show that in the specific case of an ensemble of non-interacting spin-1/2 in a static magnetic field B_0 and a perpendicular control field $B_1 \cos(\omega_c t)$, under the influence of T_1 and T_2 processes which act on the spins individually, the master equation is equivalent to the phenomenological description by Bloch [15].

For a single spin-1/2 in the ensemble, the Hamiltonian is

$$H' = \frac{\Delta}{2}\sigma_z + \frac{\Omega}{2}\left(\cos\phi\ \sigma_x + \sin\phi\ \sigma_y\right) \ .$$

The spin-lattice relaxation is modeled with Lindblad operators $\{L_+, L_-\}$, which drive the spin to its thermal equilibrium state ρ_T over the timescale given by T_1. Spin-spin relaxation, which leads to decoherence with time constant T_2 but conserves polarization, is modeled by the Lindblad operator L_z. The operators are

$$L_+ = \sqrt{\frac{1+p_T}{2\mathrm{T}_1}}\sigma_+ \ , \qquad L_- = \sqrt{\frac{1-p_T}{2\mathrm{T}_1}}\sigma_- \ , \qquad L_\mathrm{z} = \sqrt{\frac{1}{2\mathrm{T}_2}}\sigma_z \ .$$

Substituting the Lindblad operators and the Hamiltonian with $\phi = 0$ in Eq. 1.11 and simplifying, we can write the Lindblad master equation for the system. We now recast the master equation in the Bloch basis, given by $\mathcal{B} = \frac{1}{\sqrt{2}}\{\mathbb{1}, \sigma_x, \sigma_y, \sigma_z\}$. Since any valid density matrix ρ must satisfy $\mathrm{Tr}(\rho) = 1$ and $\mathrm{Tr}(\rho^2) \leq 1$, it has the form $\frac{1}{\sqrt{2}}(1, \langle\sigma_x\rangle, \langle\sigma_y\rangle, \langle\sigma_z\rangle)$ in this basis. This basis also has a direct physical interpretation for spin-1/2, since $\langle\vec{\sigma}\rangle = (\langle\sigma_x\rangle, \langle\sigma_y\rangle, \langle\sigma_z\rangle)$ indicates the position of the state on the 3-dimensional Bloch sphere. We can construct the Liouville superoperator in this basis as

$$\mathcal{L}_{ij} = \mathrm{Tr}\left(B_i \cdot \mathcal{L}[B_j]\right) \ \forall \ \{B_i, B_j\} \in \mathcal{B} \ .$$

Therefore, the evolution of the state is given by the differential equation

$$\frac{d\langle\vec{\sigma}\rangle}{dt} = \mathbf{\Lambda}.\langle\vec{\sigma}\rangle + \frac{\langle\vec{\sigma}_T\rangle}{\mathrm{T}_1} \ . \tag{1.13}$$

Here,

$$\mathbf{\Lambda} = \begin{pmatrix} -\frac{1}{\mathrm{T}_2'} & -\Delta & 0 \\ \Delta & -\frac{1}{\mathrm{T}_2'} & \Omega \\ 0 & -\Omega & -\frac{1}{\mathrm{T}_1} \end{pmatrix}$$

is the generator of the evolution, $\langle\vec{\sigma}_T\rangle = (0, 0, p_T)$ represents the thermal equilibrium density matrix, $\mathrm{T}_2' = \left(\frac{1}{\mathrm{T}_2} + \frac{1}{2\mathrm{T}_1}\right)^{-1}$ is the effective spin-spin relaxation time and we have dropped the time invariant $\mathbb{1}$ component. Since $\langle\vec{\sigma}\rangle$ is also proportional to the magnetization of the non-interacting ensemble $\vec{M}$, its evolution is given by the differential equation

$$\frac{d\vec{M}}{dt} = \mathbf{\Lambda}.\vec{M} + \frac{M_0}{\mathrm{T}_1}\hat{z} \ , \tag{1.14}$$

where $M_0 \propto p_T$ is the thermal equilibrium magnetization. Eq. 1.14 are the Bloch equations [15], and we use this description to analyze bound exciton dynamics in Ch. 5.

1.2.5 Magnetic Dipole-Dipole Interaction

The general form of the magnetic dipole-dipole interaction Hamiltonian between two spins labelled 1 and 2, under the point-dipole approximation, is

$$H_D^{12} = -\frac{\mu_0\gamma_1\gamma_2\hbar^2}{4\pi|\vec{\mathbf{r}}|^3}\frac{3(\vec{\sigma}^1.\hat{\mathbf{r}})(\vec{\sigma}^2.\hat{\mathbf{r}}) - \vec{\sigma}^1.\vec{\sigma}^2}{4} \ , \tag{1.15}$$

where $\vec{\mathbf{r}} = (r_x, r_y, r_z)$ is the vector joining the two spins and $\hat{\mathbf{r}} = (e_x, e_y, e_z)$ is the corresponding unit vector. A more compact notation is to write

$$H_D^{12} = \frac{1}{4}\vec{\sigma}^1 \cdot \mathbf{D}^{12} \cdot \vec{\sigma}^2 \ , \tag{1.16}$$

where the dipolar interaction tensor $\mathbf{D}^{12}$ is a second order tensor, with elements

$$D_{ij}^{12} = \frac{\mu_0 \gamma_1 \gamma_2 \hbar^2}{4\pi |\vec{\mathbf{r}}|^3} \left(\delta_{ij} - 3e_i e_j\right) \forall \ \{i,j\} \in \{x,y,z\} \ . \tag{1.17}$$

Note that $\mathbf{D}^{12}$ is symmetric and traceless. While the explicit form above requires the point-dipole approximation, Eq. 1.16 does not.

Writing $\vec{\mathbf{r}} = (r, \theta, \phi)$ in spherical coordinates, Eq. 1.15 can also be recast into the well known alphabet form [9, 16]

$$H_D^{12} = \frac{\mu_0}{4\pi} \hbar^2 \gamma_1 \gamma_2 \frac{1}{4r^3} \left(A + B + C + D + E + F\right) \ , \tag{1.18}$$

where

$$\begin{aligned}
A &= (1 - 3\cos^2\theta)\sigma_z^1 \sigma_z^2 \ , & B &= -\frac{1 - 3\cos^2\theta}{4} \left(\sigma_+^1 \sigma_-^2 + \sigma_-^1 \sigma_+^2\right) \ , \\
C &= -\frac{3}{2} \sin\theta \cos\theta e^{-i\phi} \left(\sigma_z^1 \sigma_+^2 + \sigma_+^1 \sigma_z^2\right) \ , & D &= -\frac{3}{2} \sin\theta \cos\theta e^{i\phi} \left(\sigma_z^1 \sigma_-^2 + \sigma_-^1 \sigma_z^2\right) \ , \\
E &= -\frac{3}{4} \sin^2\theta e^{-2i\phi} \sigma_+^1 \sigma_+^2 \ , & F &= -\frac{3}{4} \sin^2\theta e^{2i\phi} \sigma_-^1 \sigma_-^2 \ .
\end{aligned}$$

The dipole-dipole interaction is often small compared to Zeeman interaction in magnetic resonance experiments. In such cases, for dipole-dipole interactions between "like" spins ($\gamma_1 = \gamma_2$), the A and B terms survive the RWA. For "unlike" spins with $|\gamma_1| \gg |\gamma_2|$ or vice versa, the A term is the only one to survive RWA.

1.3 Infinitesimal Strain Theory

Strain in the silicon lattice, static as well as time dependent, plays an important role in our experiments. The purpose of this short section is to introduce the basic concept of infinitesimal strain theory and its notation.

A general deformation of an object can be thought of as a mapping of each point in the body, located at position $\vec{r}$, to a new location $\vec{r} + \vec{dr}$. Therefore, for a three-dimensional object, it is described by a second-order (3×3) tensor. The general deformation tensor can be decomposed into a symmetric (strain) and anti-symmetric (rotation) part. Therefore, the strain is written as

$$\boldsymbol{\epsilon} = \begin{pmatrix} \epsilon_{xx} & \epsilon_{xy} & \epsilon_{xz} \\ \epsilon_{xy} & \epsilon_{yy} & \epsilon_{yz} \\ \epsilon_{xz} & \epsilon_{yz} & \epsilon_{zz} \end{pmatrix} \ . \tag{1.19}$$

The strain tensor has 6 independent terms, and can further be decomposed into an isotropic component and a traceless one, given by

$$\boldsymbol{\epsilon} = \epsilon_h \mathbb{1} + \boldsymbol{\epsilon'} \ , \tag{1.20}$$

where $\epsilon_h = \left(\frac{\epsilon_{xx}+\epsilon_{yy}+\epsilon_{zz}}{3}\right)$ is the hydrostatic or volumetric strain and $\boldsymbol{\epsilon'}$ is called the deviatoric strain.

The stress quantifies the internal distribution of contact forces in a body. This can also be written as a second-order (3×3) tensor. The anti-symmetric component of this tensor is equal to the net torque, which must be zero for an object at equilibrium. Therefore, the stress tensor $\boldsymbol{\sigma}$ is constrained to be symmetric, resulting in 6 independent terms. It can also be decomposed into a hydrostatic and deviatoric component. In the limit of infinitesimal strain, the applied stresses and induced strains inside a material are related by Hooke's law [17],

$$\boldsymbol{\epsilon} = -\mathbf{C}.\boldsymbol{\sigma} \ , \tag{1.21}$$

where the stiffness $\mathbf{C}$ is a fourth-order $(3 \times 3 \times 3 \times 3)$ tensor. The symmetry of the stress/strain tensors and of the strain energy density constrains the stiffness tensor to have at most 21 independent terms [18]. It is helpful to write the Hooke's law using the Voight notation [19], where $\boldsymbol{\sigma}$ and $\boldsymbol{\epsilon}$ are converted to 6-dimensional vectors

$$\vec{\epsilon} = (\epsilon_{xx}, \epsilon_{yy}, \epsilon_{zz}, 2\epsilon_{yz}, 2\epsilon_{xz}, 2\epsilon_{xy}) \ , \tag{1.22}$$

$$\vec{\boldsymbol{\sigma}} = (\sigma_{xx}, \sigma_{yy}, \sigma_{zz}, \sigma_{yz}, \sigma_{xz}, \sigma_{xy}) \ , \tag{1.23}$$

and the stiffness $\mathbf{C}$ is written as a second-order (6×6) tensor.

Chapter 2

Phosphorus-doped Silicon

Silicon is an intrinsic semiconductor with an indirect bandgap. It can be doped with group 3 elements (boron, aluminum, etc) to form a p-type semiconductor, or with group 5 elements (phosphorus, arsenic, etc) to form an n-type semiconductor. These dopants form substitutional defects in the lattice, giving rise to interesting local properties. This chapter provides a brief introduction to phosphorus-doped silicon, which the experiments in this thesis focus on.

2.1 Introduction

The only stable isotope of phosphorus (^{31}P) has a spin-1/2 nucleus. Phosphorus has an extra unpaired (donor) electron which is free to move around in the conduction band in doped silicon at room temperature. However, it is localized to the defect site at low temperatures (< 30 K) and has a strong hyperfine interaction with the nuclear spins. As a result, phosphorus defects have been investigated as a candidate from quantum computing and sensing applications, starting with the proposal by Kane [20].

Silicon, on the other hand, has three stable isotopes: ^{28}Si with spin-0 and 92.2% natural abundance, ^{29}Si with spin-1/2 and 4.7% abundance and ^{30}Si with spin-0 and 3.1% abundance. Kane's proposal identified ^{29}Si spins as a major source of noise for the defect electron and nuclear spins. Therefore, enrichment with the spin-0 isotopes is desirable for these applications. The isotopes can be separated by gas centrifugation of SiF_4, followed by conversion to silane (SiH_4) and chemical vapor deposition (CVD) [21]. The Avogadro project [22], which aimed to create a new standard for the kilogram using isotopically pure

^{28}Si, resulted in highly enriched ^{28}Si samples with 46 ppm ^{29}Si. These samples have since proved critical for a wide variety of quantum information experiments using the defect spins [1, 4, 23–25]. We use an isotopically purified ^{28}Si sample from the same project [1] for the experiments in Ch. 5, which focus on the ^{31}P nuclear spin. However, ^{29}Si spins can serve as a testbed for many-body physics experiments, and have also been explored as a resource for Magnetic Resonance Imaging (MRI) [5, 26], due to their long relaxation times across a large temperature range. Our experiments in Ch. 6 focus on these ^{29}Si spins and their interaction with ^{31}P spins, using a natural abundance silicon sample [1].

2.2 Band Structure of Silicon

Silicon is an indirect bandgap semiconductor, as illustrated schematically in Fig. 2.1. Therefore, absorption or emission of photons, resulting from transitions between the valence and conduction bands, must be accompanied with absorption or emission of phonons. In the case of illumination with above-bandgap light, the absorption of photons results in the emission of phonons into the sample.

Phosphorus is a "shallow" donor since the ground state energy of the neutral, bound state (D^0) of the donor electron is 45.3 meV below the conduction band, which is small compared to the bandgap (> 1.14 eV). Silicon also exhibits a metal-insulator transition as a function of doping concentration [27]. Above a threshold concentration ($\sim 10^{18}$ cm^{-3}), the overlap between neighbouring defect electron wavefunctions introduces an exchange interaction, such that the ground state of the donor electron is a non-localized state. As a result, heavily doped silicon remains conducting/metallic at all temperatures. Below this threshold, however, the eigenstates of the impurity potential are localized to the phosphorus site. The energy level structure of the donor under these conditions is illustrated in Fig. 2.1. Since there is a large continuum of available states in the conduction band, the thermal energy ($k_BT = 26$ meV at 300 K) is still sufficient to keep most sites ionized at temperatures above ~ 50 K, resulting in a conducting sample, and a single electron spin-1/2 line is observed in ESR measurements [28] with no observable hyperfine coupling. However, at temperatures below 30 K, the donors are localized to the site with probability $\simeq 1$, as shown in Fig. 2.2. This results in an insulating sample at thermal equilibrium under the experimental conditions used in this thesis (between 1.2 K and 4.2 K) and a

[1] The sample was provided by Prof. M.L.W Thewalt

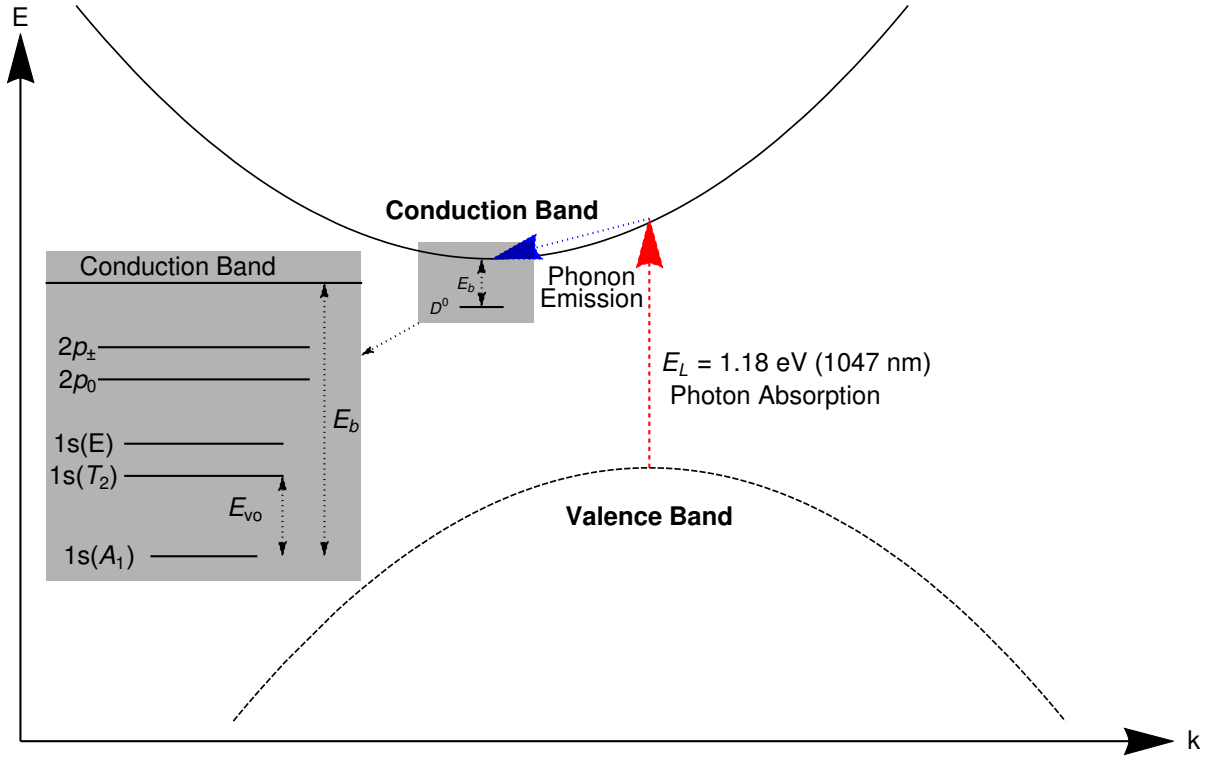

Figure 2.1: A simplified band diagram, showing the indirect bandgap and shallow donor state in silicon. The absorption of above-bandgap linearly polarized photons (red, dashed) leads to the emission of phonons (blue, dotted). The bound neutral defect state (D^0) with the binding energy E_b (45.3 meV) is shown, with a zoomed-in version showing the electronic level structure of the defect. E_{VO} (12.95 meV) is the energy difference between the defect ground state and the first excited state.

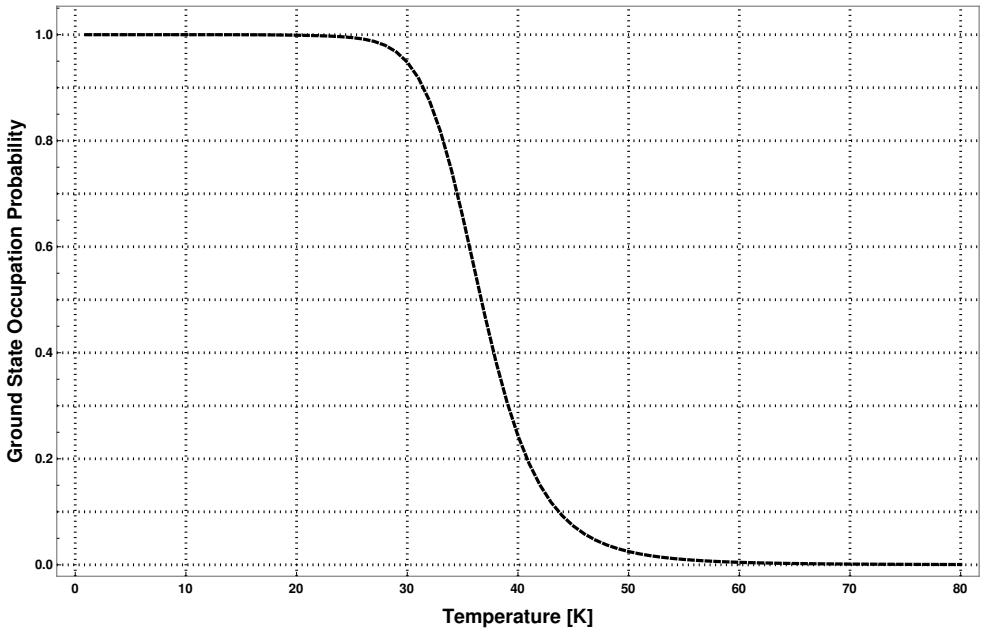

Figure 2.2: Occupation probability of the ground state by the ^{31}P defect electron as a function of temperature, demonstrating the localization at low temperatures (< 30 K). The probability was approximated numerically from the defect energy levels [28] and the density of states (DOS) of the conduction band [29].

strong hyperfine interaction with the ^{31}P as well as a smaller interaction with neighbouring ^{29}Si nuclear spins. This "transition" with temperature can easily be observed with ESR [28], dielectric constant measurements as well as conductivity measurements.

2.3 Electron Wavefunction of Neutral Donor

The wavefunction of the defect electron has been the subject of investigations dating back to the effective mass theory (EMT) approach proposed by Kohn and Luttinger [30] in 1955. This remains the preferred analytical approach, with a significant body of work aimed at refining it. This approach involves writing the Schrodinger equation with a Coulombic impurity potential, and assuming that the wavefunction is localized around six degenerate conduction band minima. This approximation is well satisfied for phosphorus donors in silicon. The donor electron wavefunction can then be written as

$$\psi(\vec{r}) = \sum_{j=1}^{6} \alpha_j F_j(\vec{r}) \phi_{\vec{k}_j^{(0)}}(r) \ , \tag{2.1}$$

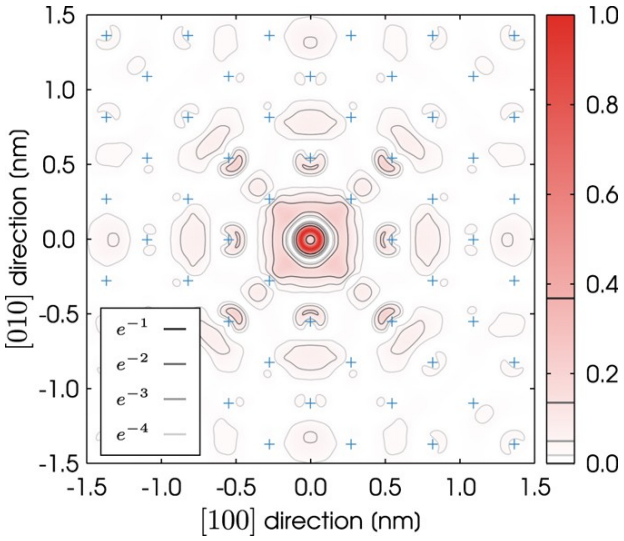

Figure 2.3: Probability density of the defect electron ($|\psi|^2$) in the 001 plane, with the silicon atom sites indicated by blue pluses. Figure reproduced without modifications from Smith et al. [34] under a Creative Commons license CC-BY-4.0

where $\phi_{\vec{k}_j^{(0)}}(r)$ are the eigenstates of the crystal Hamiltonian (Bloch states), corresponding to the six conduction band minima and the coefficients $\{\alpha_j\}$ are determined by the symmetry group of the defect (T_d). For the ground state (labelled as $1s(A_1)$ in Fig. 2.1), $\alpha_j = \frac{1}{\sqrt{6}}$. Kohn and Luttinger proposed an ansatz for the envelope, of the form

$$F_j(r) = \frac{1}{\sqrt{6\pi a_\perp^2 a_\parallel}} \exp\left(-\sqrt{\frac{x^2+y^2}{a_\perp^2} + \frac{z^2}{a_\parallel^2}}\right),$$

where $a_\perp$ and $a_\parallel$ are variational parameters. Since these two are in general not equal, the wavefunction envelope has a pancake shape, with radii $a_\perp = 2.51$ nm and $a_\parallel = 1.44$ nm for phosphorus [31]. The effective Bohr radius of the wavefunction is given by the geometric mean $a_B = a_\parallel^{1/3} a_\perp^{2/3}$, which is 2.087 nm. Models using more recently developed numerical tools such as density-functional theory (DFT) have also been proposed by Hollenberg and others [32–34]. These models show good agreement with experiments as well as with EMT. The simulated probability density $|\Psi(\vec{r})|^2$ of the defect electron is shown in Fig. 2.3.

2.4 Hyperfine Interaction

In general, the hyperfine interaction between the defect electron spin and a nearby nuclear spin at $\vec{r}_n$ can be written as

$$H_{HF}^{en} = \frac{1}{4}\vec{\sigma}^e \cdot \mathbf{A}^{en} \cdot \vec{\sigma}^n \ ,$$

where $\mathbf{A}^{en}$ is the hyperfine interaction tensor, which depends on $\vec{r}_n$. The hyperfine interaction is a sum of two different interactions. The first is the isotropic Fermi-contact interaction, proportional to the overlap of the spatial wavefunction of the electron with the nuclear spin, such that

$$H_{FC}^{en} = \frac{1}{4}A_{en}\vec{\sigma}^e \cdot \vec{\sigma}^n \ , \tag{2.2}$$

$$A_{en} = -\frac{8\pi}{3}\hbar^2\gamma_e\gamma_n|\Psi(\vec{r}_n)|^2 \ . \tag{2.3}$$

The second is the anisotropic dipolar interaction described in Ch. 1. Therefore,

$$\mathbf{A}^{en} = A_{en}\mathbb{1} + \mathbf{D}^{en} \ , \tag{2.4}$$

where $\mathbf{D}^{en}$ is the traceless, symmetric dipolar interaction tensor.

The tetrahedral symmetry (point group $\mathrm{T_d}$, which has 24 elements) of the defect site requires that the hyperfine interaction tensor be invariant under all 24 operations of the group. This is only possible for a tensor proportional to the identity operator. This implies that the dipolar component of the hyperfine interaction must be zero, such that

$$H_{HF}^{eP} = \frac{A_{eP}}{4}\vec{\sigma}^e \cdot \vec{\sigma}^P \ .$$

The overlap $|\Psi(\vec{r}_n)|^2$ is maximum at the defect site ($\vec{r}_P = 0$), resulting in a large isotropic hyperfine interaction ($A_{eP} = 117.532$ MHz [35]) with the ^{31}P nuclear spin. In contrast, the interaction of the electron with the nearby ^{29}Si is not constrained to be isotropic, since the presence of the ^{31}P defect breaks the tetrahedral symmetry at these sites. The hyperfine interaction with these spins can therefore have a non-zero dipolar component.

2.4.1 Strain Dependence of the Fermi-contact Interaction

Strain in the lattice results in a distortion of the electron wavefunction relative to its unstrained state. This changes the overlap $|\Psi(\vec{r}_n)|^2$, modifying the Fermi-contact interaction.

In the limit of small/infinitesimal strain, we can approximate the effect with a Taylor expansion up to second order in strain,

$$A_{en}(\vec{\epsilon}) = A_{en}(0)\left(1 + \vec{\nabla}A_{en}\cdot\vec{\epsilon} + \frac{1}{2}\vec{\epsilon}\cdot\mathbf{H}_{A_{en}}\cdot\vec{\epsilon}\right) \ . \tag{2.5}$$

We use the Voight notation such that the strain is a 6-dimensional vector and $\vec{\nabla}A_{en}$ and $\mathbf{H}_{A_{en}}$ are the 6×6 dimensional Jacobian and Hessian matrices respectively. Perturbations to the ^{31}P hyperfine interaction under application of strain and electric fields must also be invariant under the symmetry transformations. This constraints $\vec{\nabla}A_{eP}$ and $\mathbf{H}_{A_{eP}}$ to have the form [6, 36]

$$\vec{\nabla}A_{eP}\cdot\vec{\epsilon} = K\epsilon_{hs} \ , \tag{2.6}$$

$$\begin{aligned}\vec{\epsilon}\cdot\mathbf{H}_{A_{eP}}\cdot\vec{\epsilon} = {} & X\left(\epsilon_{xx}^2+\epsilon_{yy}^2+\epsilon_{zz}^2\right) + Y\left(\epsilon_{xx}\epsilon_{yy}+\epsilon_{yy}\epsilon_{zz}+\epsilon_{xx}\epsilon_{zz}\right) \\ & + Z\left(\epsilon_{xy}^2+\epsilon_{yz}^2+\epsilon_{xz}^2\right) \ ,\end{aligned} \tag{2.7}$$

where $\epsilon_{hs} = \frac{(\epsilon_{xx}+\epsilon_{yy}+\epsilon_{zz})}{3}$ is the hydrostatic strain, and K, X, Y and Z are constants.

Chapter 3

Magnetic Resonance in Phosphorus-doped Silicon

The previous chapter introduced the phosphorus defect in silicon. In this chapter, we look at the magnetic resonance properties of the electron, ^{29}Si and ^{31}P nuclear spins.

3.1 Introduction

We approximate the sample as an ensemble of independent subsystems, each consisting of a phosphorus defect and all the silicon sites within a radius r, where the average distance between nearest-neighbour phosphorus defects is $2r$. This approximation is valid in the dilute doping regime, where the average distance is large enough that the coupling between defect electrons is negligible. The average distances to the nearest-neighbour ^{29}Si and ^{31}P are calculated in Appendix A and listed in Table 3.1.

Each subsystem comprises of a defect electron spin, a ^{31}P nuclear spin and a set $\{^{29}\text{Si}\}$ of nearby ^{29}Si nuclear spins (~ 1500 and 4×10^5 for the ^{28}Si enriched and natural abundance

Neighbour	Concentration	Average Distance
^{29}Si	4.7%	0.433 nm
^{29}Si	46 ppm	4.198 nm
^{31}P	1.5×10^{15} cm^{-3}	48.328 nm
^{31}P	6×10^{15} cm^{-3}	30.444 nm

Table 3.1: Average distance to the nearest neighbour

Term	Value	Term	Value
ω_e	188 GHz	ω_P	115 MHz
ω_{Si}	56 MHz	A_{eP}	117 MHz
$\lvert\mathbf{A}^{ej}\rvert$	0-3 MHz	$\lvert\mathbf{D}^{Pj}\rvert$	0-200 Hz
$\lvert\mathbf{D}^{ij}\rvert$	0-100 Hz		

Table 3.2: Range of values for terms of the Hamiltonian in Eq. 3.1, at $B_0 = 6.7$ T

samples respectively). The Hamiltonian in the presence of a static magnetic field B_0 is

$$H = \frac{\omega_e}{2}\sigma_z^e + \frac{\omega_P}{2}\sigma_z^P + \frac{\omega_{Si}}{2}\sum_{j\in\{^{29}\mathrm{Si}\}}\sigma_z^j + \frac{A_{eP}}{4}\vec{\sigma}^e\cdot\vec{\sigma}^P \tag{3.1}$$
$$+\frac{1}{4}\sum_{j\in\{^{29}\mathrm{Si}\}}\vec{\sigma}^e\cdot\mathbf{A}^{ej}\cdot\vec{\sigma}^j + \frac{1}{4}\sum_{j\in\{^{29}\mathrm{Si}\}}\vec{\sigma}^P\cdot\mathbf{D}^{Pj}\cdot\vec{\sigma}^j + \frac{1}{4}\sum_{\{i,j\}\in\{^{29}\mathrm{Si}\}}\vec{\sigma}^i\cdot\mathbf{D}^{ij}\cdot\vec{\sigma}^j\ ,$$

where $\omega_e = \gamma_e B_0$, $\omega_P = \gamma_P B_0$ and $\omega_{Si} = \gamma_{Si} B_0$ are the respective Larmor precession frequencies, $\{\mathbf{A}^{ej}\}$ are the hyperfine interaction tensors between the electron and the ^{29}Si and $\{\mathbf{D}^{Pj}\}$ and $\{\mathbf{D}^{ij}\}$ are the dipolar interaction tensors corresponding to the ^{31}P-^{29}Si and ^{29}Si-^{29}Si dipolar interactions respectively. Table 3.2 provides the range of values for the terms in the Hamiltonian at 6.7 T.

3.2 Defect Electron Spin

The hyperfine interaction with the ^{31}P spin ($A_{eP} = 117.532$ MHz) corresponds to a magnetic field of 42 G on the electron spin. For $B_0 \gg 42$ G, the electron spin Larmor is the dominant term in Eq. 3.1, such that the electron is quantized in the Zeeman eigenbasis. The ^{31}P hyperfine interaction is reduced to a $\sigma_z^e\sigma_z^P$ form, resulting in a splitting of the electron lineshape. In practice, the ^{31}P hyperfine interaction A_{eP} is not identical across different subsystems, leading to an isotopic [7] line broadening. The presence of multiple isotopes causes local symmetry breaking and changes to the effective mass of the electron, which modifies the defect electron wavefunction (and therefore the value of the hyperfine coupling). The isotopic effect was found to be composed of two distinct contributions [25]. The first is a discrete change in the hyperfine interaction, dependent on the average mass of the nearest-neighbour silicon isotopes. This effect is asymmetric in natural abundance silicon, where configurations of nearest neighbours with increasing average mass will result in a larger hyperfine coupling but are less likely. The second is a continuous broadening,

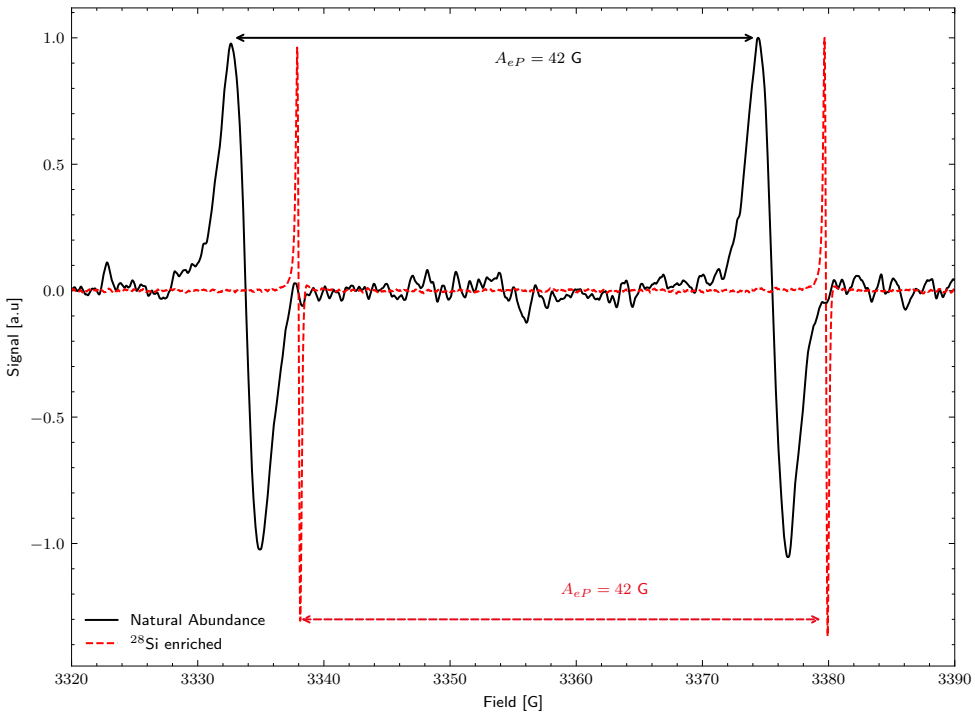

Figure 3.1: CW-ESR spectra of defect electron spin in natural abundance (black, solid) and ^{28}Si enriched (red, dotted) phosphorus-doped silicon, demonstrating the broadening of the electron lineshape due to isotope effects. The microwave frequency was 9.392 GHz and 9.387 GHz for the natural abundance and ^{28}Si enriched samples respectively, which contributes to the offset between the two spectra along the x-axis.

dependent on the average bulk isotopic mass. This originates from the small (10^{-5}) but observable dependence of the lattice parameter on the isotope, which generates strain in the lattice [37].

Since $\mathbf{A}^{ej}$ is a function of the location of the j^{th} ^{29}Si with respect to the defect site, and the ^{29}Si are distributed uniformly at random in the lattice, this interaction term is also not identical across different subsystems. The coherence time (T_2^e) of individual defect electron spins is also affected by the coupling to the large ^{29}Si environment, and reducing the size of this environment by almost three orders of magnitude results in significantly longer single spin T_2^e. As a result of the above effects, the electron T_2^e is a strong function of the isotopic concentration. Feher [38] was the first to demonstrate that enriching silicon with the ^{28}Si isotope results in a narrowing of the ESR lineshape. The continuous wave(CW)-ESR spectra of the electron spin at 20 K for the ^{28}Si-enriched and natural abundance silicon samples, shown in Fig. 3.1, also demonstrate this effect.

3.3 ^{31}P Nuclear Spin

The ^{31}P nuclear spin has a gyromagnetic ratio of $\gamma_P = 2\pi \times 17.235$ MHz/T. This means that the Zeeman interaction frequency ω_P is comparable to or smaller than the hyperfine coupling A_{eP} at most practical field values. However, since the secular part of the Hamiltonian with respect to the electron Zeeman frequency ω_e is $\sigma_z^e \sigma_z^P$, the eigenstates of the ^{31}P nuclear spin are the Zeeman eigenstates for $B_0 \gg 42$ G.

Similar to the defect electron spin, the ^{31}P nuclear spin coherence time is also affected by the isotopic broadening and the nearby ^{29}Si nuclear spin bath. The combination of the two results in an inhomogeneous linewidth for ^{31}P nuclear spins in natural abundance silicon of 30 kHz [7] with an asymmetric lineshape, compared to ≤ 200 Hz (limited by field inhomogeneity and susceptibility effects) in isotopically enriched ^{28}Si.

The relaxation timescales for the spins are summarized in Table 3.3. The biggest source of ^{31}P dephasing in natural abundance silicon is the interaction with nearby ^{29}Si nuclear spins, which is ~ 100 Hz based on the 0.433 nm average distance. In the case of isotopically enriched ^{28}Si, the nearest ^{29}Si is much farther away on average, at 4.198 nm, resulting in a dipolar coupling ~ 0.14 Hz. The ^{31}P T_2^n in this case is limited by the electron spin T_1^e, which induces a random phase on the nuclear spin with each electron spin flip due to the strong hyperfine interaction. The resulting T_2^n process on the ^{31}P is given by $T_2^n = \frac{T_1^e}{p_{\downarrow_e}}$, where $p_{\downarrow_e} = \left(1 + \exp\left(\frac{\hbar\omega_e}{k_B T}\right)\right)^{-1}$ [36] is the probability of occupation of the excited state for the electron. Therefore, on-demand ionization of the defect electron is a useful tool for further extending the coherence times of the ^{31}P. This has been achieved optically [1], demonstrating that the ^{31}P T_2^n can be increased to 39 mins at room temperature and several hours at 4.2 K in a sample with lower defect concentration. The nuclear T_1^n is extremely long ($\gg 10^4$ s) for isotopically enriched ^{28}Si at 1.7 K, but is ~ 712 s [4] at 4.2 K.

3.4 ^{29}Si Nuclear Spins

The gyromagnetic ratio of silicon ($\gamma_{Si} = -2\pi \times 8.465$ MHz/T) results in a resonance frequency of 55-57 MHz at our experimental fields of 6.5-6.7 T. The negative sign of the gyromagnetic ratio indicates that the $|\downarrow\rangle$ state is the ground state, the same as the electron spin and opposite to that of the ^{31}P spin. This has some interesting consequences which

we explore in Ch. 6. Fig. 2.3 indicates that the nearby silicon lattice sites also experience an overlap with the electron wavefunction $\Psi(\vec{r})$, such that the isotropic component A_{ej} is expected to be significant for ^{29}Si close to the defect. However, the magnitude $|\Psi(\vec{r})|^2$ at these lattice sites is often much smaller than one would predict based on the envelope $F_j(r)$ alone, because of the oscillatory nature of the Bloch states. As a result, the largest hyperfine interaction observed for ^{29}Si is significantly smaller (3.1 MHz [39]) than that of ^{31}P, even though $F_j(r)$ would suggest a hyperfine coupling of more than 80 MHz. Compared to the silicon lattice constant of 0.543 nm, the Bohr radius of ~ 2 nm indicates that the electron wavefunction span will include a large number of silicon atoms, 4.7 % of which are ^{29}Si in natural abundance silicon.

These interactions were mapped first by Feher [40] and then by Hale [39, 41] in a very comprehensive manner using Electron Nuclear Double Resonance (ENDOR) measurements. The ENDOR spectrum reveals several sharp, resolved lines between 3.1 MHz to 300 kHz that can be mapped to 19 "shells" containing a total of ~ 200 nuclei. It is possible to map the spectral lines to lattice position (to some extent) by performing orientation dependent measurements, since the contact hyperfine term A_{ej} (and the wavefunction overlap) obeys the symmetry of the defect site, whereas the dipolar interaction term $\mathbf{D}^{ej}$ obeys cylindrical symmetry about the static field. Below 300 kHz, there is a "continuum" of hyperfine shifts on the ^{29}Si, because the difference in the hyperfine interaction of successive shells at this point falls within the ^{29}Si dipolar linewidth.

We divide the set $\{^{29}\text{Si}\}$ into two distinct sets for some of our analysis. We define ^{29}Si spins with a hyperfine interaction large enough to shift their resonance frequency outside the experimental spectrum integration window ($\pm$6.75 kHz, centered about the nuclear Zeeman frequency) as "core" ^{29}Si spins in this thesis, since they do not contribute to the observed signal. Based on the envelope function in Eq. 2.1, the contact hyperfine coupling decays to within the window at a distance of 7.7 nm from the defect. This volume encapsulates 12.92% of all ^{29}Si spins. The dipolar interaction falls off much more rapidly, to within the window at 1.33 nm ($< 0.07\%$ of all spins). However, the core as defined is likely to be less than 12.92% of the ^{29}Si spins, since the envelope is an upper bound and the interference of Bloch states yields smaller hyperfine coupling values for most of the nuclear spins. Therefore, the majority of ^{29}Si spins do not see an observable hyperfine interaction with the defect electron due to the dilute doping concentration, and contribute to our measured ^{29}Si signal. These are referred to as "bulk" ^{29}Si spins for the remainder of this thesis.

	4.7% ^{29}Si, 6×10^{15} cm^{-3} ^{31}P	**46 ppm ^{29}Si,1.5×10^{15} cm^{-3} ^{31}P**	
	4.2 K	**1.7 K**	**4.2 K**
^{29}Si T_1	$10^6 - 10^7$ s		
^{29}Si T_2	12 ms		
^{31}P T_1	572 s	$> 10^4$ s	712
^{31}P T_2	16 ms	421 ms	56 ms
Donor e$^-$ T_1	1 ms		

Table 3.3: Spin Relaxation Lifetimes

Chapter 4

Experimental Setup and Methods

This chapter contains a description of the experimental setup as well as the basic data processing methods. Specific modifications made for each experiment are detailed in their respective chapters.

4.1 Overview

All experiments were carried out using home built RF probes and a commercial Bruker spectrometer. The samples were immersed in a liquid helium bath, which was maintained at 4.2 K (atmospheric pressure) or lower (by pumping) inside a long tailed Janis cryostat, inserted into the bore of an Oxford superconducting wide-bore (89 mm) magnet, whose field was set to 6.57 T for a part of the experiments and at 6.7 T for the rest.

4.2 Radio Frequency Tank Circuits

We use two different circuit designs for the experiments in Ch. 5 and Ch. 6. The first one is a single channel split resonance design [42], shown in Fig. 4.1a. This circuit is effectively two almost identical oscillators coupled together capacitively (through C4). The coupling splits the resonance into two, and allows for tuning/matching of the individual resonances by varying the capacitors C1-C4. In practice, only 3 capacitors need to be varied in order to achieve a satisfactory tuning and matching range. Since the sample sits in L1 while the field is distributed equally in L1 and L2, we lose a factor of two in filling factor with this design. However, we avoid the need to filter/isolate two separate channels, which is harder when the two frequencies are relatively close to each other. This is useful when we

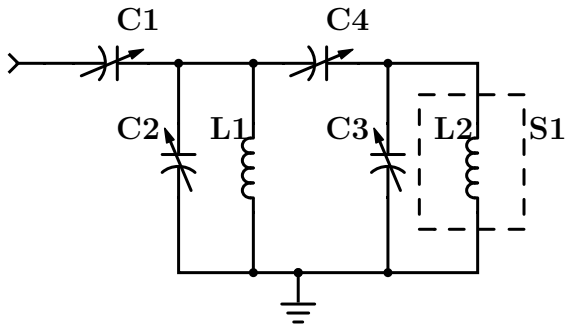

(a) Single Channel Split Resonance Circuit

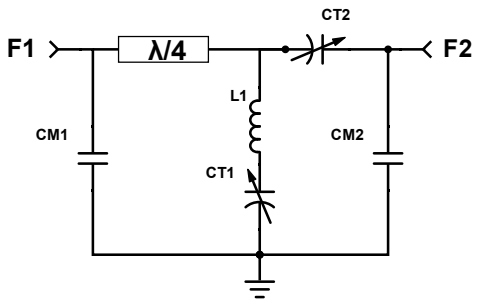

(b) Two Channel Double Resonance Circuit

Figure 4.1: The two tank circuits used for our experiments. We use low temperature ceramic capacitors from Voltronics. The arrow across capacitors indicates tunable ones (Voltronics NMCB10-5CKE). The inductor/detection coils were made using rhodium flashed copper wire. One of the coils in the split resonance circuit (L2) was shielded with a copper cage (S1) to minimize mutual inductance between the coils.

want to address the neutral (D^0) and ionized (D^+) ^{31}P spin states, since we do not need to detect the two states simultaneously or pulse on one while detecting on the other. The second probe circuit is a traditional two channel double-resonance design [43], shown in Fig. 4.1b. It is designed to resonate close to 174 MHz and 56 MHz, allowing us to pulse and detect both ^{29}Si and ^{31}P spins. The $\lambda/4$ section at 174 MHz acts as a filter preventing leakage from the high frequency channel into the low frequency one, whereas the reverse is prevented by CM2, which is effectively a short circuit for the high frequency and serves as a matching capacitor for low frequency. This provides 13 dB of isolation between the two channels (measured by S_{12} at the two frequencies). We achieve additional isolation (40 dB) by using Bruker RF filters at room temperature (low-pass filter for the 56 MHz channel, high-pass filter for the 174 MHz channel).

4.3 Cryogenics

We use a Janis 10CNDT cryostat, which is a "wet" cryostat with a helium space volume of 8 L. The bottom part of the cryostat has concentric tails that fit inside the bore of the superconducting magnet. The outermost tail at room temperature has an O.D of 3.375 in., whereas the innermost tail has an I.D of 1.88 in.. The bottoms of the tails were fitted with three aligned sapphire windows at room temperature, 77 K and LHe temperature respectively, in order to allow infrared radiation from the laser to reach the sample. Sap-

phire was chosen for its excellent infrared properties while providing the hardness to form a reliable indium seal against the aluminum flange on the tail. This introduces a noticeable heat load on the Helium bath, but still provides a single shot hold time of 20-28 hours at 4.2 K, depending on the laser power used. Hold times at 1.3 K are around 10 hours, and relatively unaffected by laser power.

In order to reach temperatures between 4.2 K to 1.3 K, we pump on the LHe space using a RUVAC WS1001 roots blower pump, backed by a TRIVAC B D 65 B rotary vane pump. While pumping, special care has to be taken to keep the cryostat free of leaks, as nitrogen ice can cover the optical window for the laser and also pose a potential safety hazard. The RF tank circuit was mounted on a cryogenic insert designed to hold a vacuum seal while allowing for tuning and matching. The insert consists of a hollow 3 ft long stainless steel tube with 1/2 in. diameter, brazed on to a brass tube 18 in. long. The stainless steel provides good thermal isolation between the helium bath and the room temperature end, but the brass is necessary at the bottom, since stainless steel, which is weakly magnetic, can spoil the magnetic field homogeneity if placed close to the sample. The insert also has copper baffles with aligned holes, which provide line of sight access from the top of the insert to the bottom. Some holes were used to connect the tunable ceramic capacitors at the probe circuit to the room temperature side using G10 rods through a vacuum feed-through, allowing tuning and matching of the resonant circuits at base temperature. Others were used for passing semi-rigid coaxial lines for the RF and electric field, as well as thermometer wiring (phosphor bronze twisted pairs). The coaxial lines were also stainless steel (with low loss dielectric) from the room temperature end to about halfway down to minimize heat load. We then switch to a copper coaxial line to prevent distortion of the magnetic field close to the sample. The temperature was measured using a calibrated Lakeshore Cernox resistor, through a Lakeshore 370 controller. We monitor the pressure inside the bath using a Granville-Phillips 275 Mini-Convectron Pressure Sensor as well as an analog pressure gauge.

4.4 Optical Setup

The schematic of our optical setup is shown in Fig. 4.2 and Fig. 4.3. Most components were purchased from Thorlabs (TL). The entire setup is mounted on an aluminum optical breadboard (TL MB648), mounted on five 5 in. stainless steel posts (TL P5) epoxied to the floor to ensure a consistent position. We use a 500 mW 1047 nm laser (Laserglow LRS-1047 DPSS), which outputs a 2 mm beam. The laser is mounted on a small aluminum

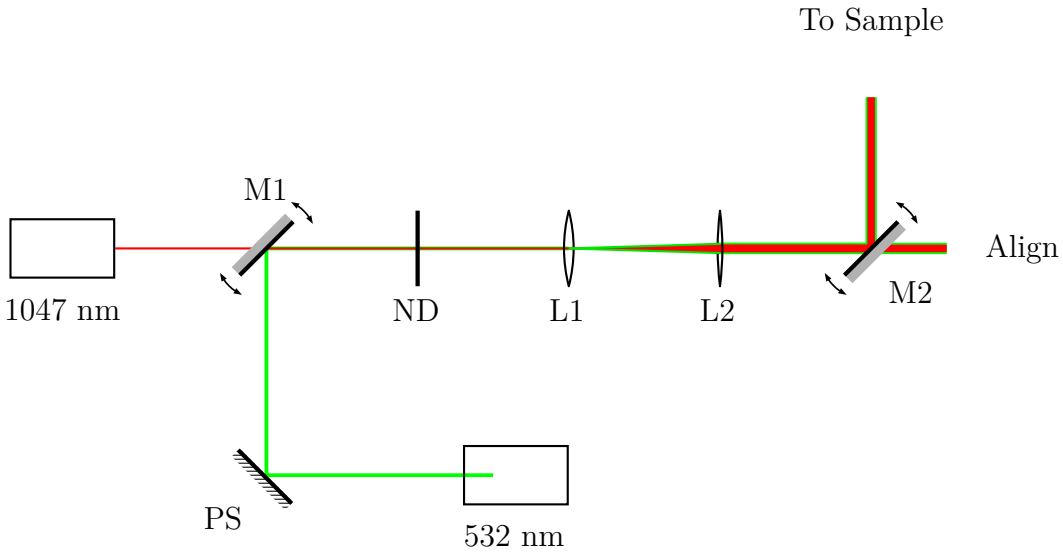

Figure 4.2: The optical setup consists of a green alignment laser (532 nm) which is aligned to the main laser (1047 nm) using a periscope (PS) and a flip mirror (M1) which can be switched in and out of the optical path. The beam then goes through a set of neutral density (ND) filters, followed by two convex lenses (L1 and L2) in a telescope configuration. This is followed by a mirror, which directs the beam up the magnet bore and onto the sample, through optical windows in the cryostat.

breadboard (TL MB4) to provide the heat sink. This breadboard is then mounted on a two-axis translation stage (TL PT102 and PT1) which allows alignment of the laser beam with respect to the telescope, which is fixed in position in the plane perpendicular to the beam direction. Variation of laser power is achieved using a variety of neutral density (ND) filters (TL NExxB-B, where xx indicates the attenuation value, ranging from xx = 01 for O.D 0.1, to xx = 60 for OD 6.0) mounted on three attenuator wheels (TL FW1A and FW 2A). The attenuation of these filters is wavelength dependent, and can also vary slightly for two filters of the same O.D value. We calibrated our filters for 1047 nm using a power meter, with the results given in Table 4.1. The telescope consists of two convex lenses L1 and L2 (TL LA1708-B and LA1131-B) of focal lengths 20 cm and 5 cm respectively, with L1 mounted on a linear translation stage (TL PT1) to enable fine tuning of the distance between the two, which helps ensure collimation of the beam. The telescope increases the beam diameter from 2 mm to 8 mm, which is necessary for illumination of the entire sample. After the telescope, the magnified beam is reflected off the adjustable mirror M2 (TL POLARIS-K1 and PF10-03-P01), which sends the beam up the magnet bore. M2 is the primary means of fine tuning the alignment of the beam on a regular basis, to correct for small long term drifts after the initial alignment. Since the infrared beam is invisible to the naked eye, it is difficult to determine if the beam is hitting the sample at base temperature. While one may align it to the coil position using infrared detector cards at room temperature, the alignment can be off at cryogenic temperatures because of movements caused by thermal contraction. Instead, we use a 5 mW green laser (Laserglow LBS-532) that can be switched in and out of the optical path using the flip mirror M1 (TL FM90, POLARIS-K1 and PF10-03-P01). We first align the green laser with the infrared using a periscope (TL RS99 and PF10-03-P01) and M1, and then use it to align the beam path inside the magnet bore, through the sapphire windows and onto the sample. In order to calibrate the loss through the optics and sapphire windows, we measured the power at the top of the cryostat at room temperature, in the absence of the cryogenic insert. Since we ensure that the beam is collimated, this is the same as the incident power on the sample holder/coil setup. We found that at maximum laser output power (430 mW) and without any ND filters, the incident power is 218 mW. The laser is triggered by a TTL from the NMR spectrometer. The response timescale was measured to be 50 ms, much faster than the irradiation times used in our experiments, which are typically hundreds/thousands of seconds long. Since the T_2^n of the ^{31}P nuclear spin is lower under irradiation [4], we need to ensure that the laser has completely turned off before we apply a RF detection pulse. Nuclear T_1^n timescales are long ($\gg$ 1 s), so we use a delay of 500 ms - 1 s between irradiation and the detection pulse.

O.D	Transmission Coefficient	O.D	Transmission Coefficient
0.1	0.792	1	8.854×10^{-2}
0.2	0.519	1.3	4.631×10^{-2}
0.3	0.393	2	4.938×10^{-2}
0.4	0.409	3	1.061×10^{-2}
0.5	0.337	4	2.050×10^{-3}
0.6 (1)	0.253	5	8.359×10^{-4}
0.6 (2)	0.267	6	7.987×10^{-3}

Table 4.1: Attenuation from ND Filters at 1047 nm. Our setup has two 0.6 O.D filters (labelled 1 and 2) on two separate wheels, with a slightly different transmission coefficient.

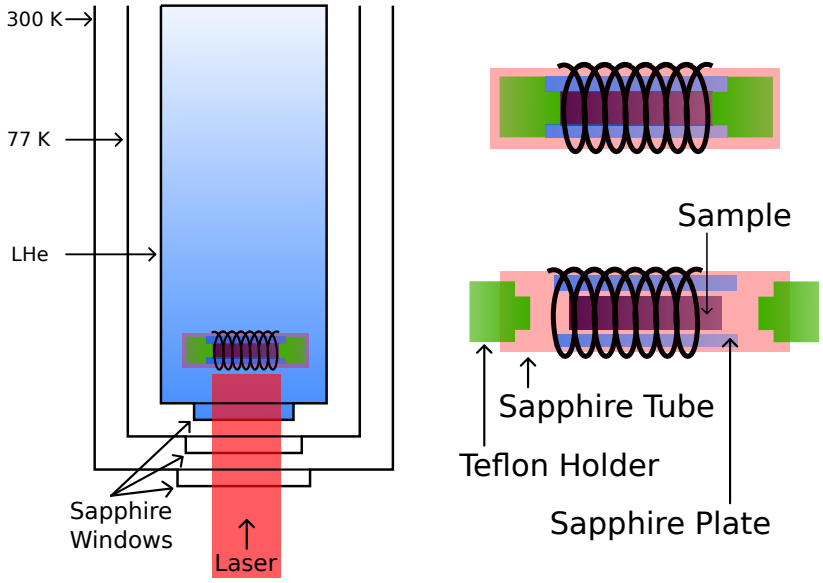

Figure 4.3: Three sapphire windows at room temperature, 77 K and LHe temperatures separated by vacuum allow optical access while providing thermal isolation. A magnified version of the sample holder is shown on the right. This ensures sample is held in place in a strain free configuration.

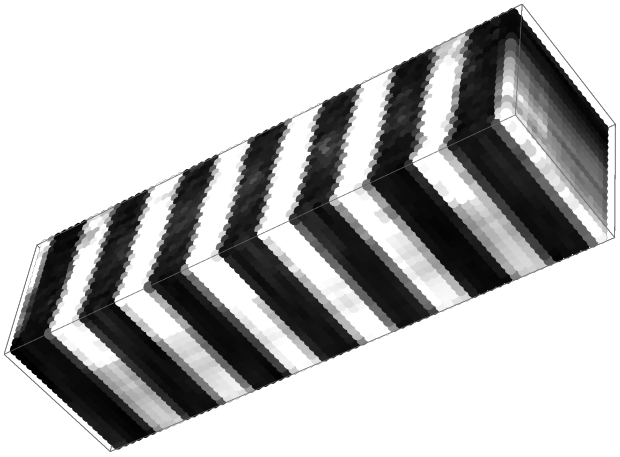

Figure 4.4: Simulated light absorption profile over the sample, due to the nonuniform light distribution created by the NMR coil and the sample holder assembly.

Once the laser beam passes through the optical access windows into the cryostat, a part of it is reflected by the detection coil, which must be around the sample for excitation and detection of the NMR signal. It is also affected by the sample holder assembly shown in Fig. 4.3. This creates a highly nonuniform light distribution over the sample. Simulations of this light distribution were carried out by Thomas Alexander [44] using COMSOL. The simulation traced 200,000 rays over a 8 mm width Gaussian beam hitting the NMR coil/sample holder setup. The resulting light intensity pattern over the sample is shown in Fig. 4.4, with the probability density function for the local light intensity in the sample shown in Fig. 5.5. In our analysis in Ch. 5, we use the simulated distribution to compare the experimental data to expected results based on a local light intensity dependent process that is driven by formation of bound excitons as well as a global light intensity dependent process that is driven by phonons. The choice of mesh size matters in this context, since the mesh must be small compared to the length scale of what is considered "global", and yet not finer than the scale of what is considered "local". Therefore, we choose a mesh size of 100 μm $\times$ 100 μm $\times$ 100 μm, large compared to the mean free path of free excitons (24 μm at 12 K [45]), but small compared to the mean free path of sub-terahertz phonons (3.3 mm at 30 K [46]). The simulations indicate that given the incident power of 218 mW, 0.232 mW is absorbed in the sample. This corresponds to uniform illumination with an intensity of 166 mW cm^{-2} assuming a penetration depth $\lambda = 26.9$ cm, as measured for intrinsic silicon at 4.2 K [47].

4.5 Data Acquisition and Processing

The data was collected using the Bruker TopSpin software on the spectrometer computer. Most of the experiments in this thesis measure the polarization $\langle \sigma_z \rangle$, which is proportional to the peak of the Free Induction Decay (FID) signal. Since there is no experimental cost to collecting the entire FID instead of just the peak, we can achieve a better signal-to-noise ratio by looking at the integral of the fourier transform of the FID, after baseline correction and smoothing using a linear filter with an exponential window function.

The decay of the FID is given by T_2^*, which is determined by the inhomogeneity of the magnetic field distribution at various nuclear spins in the ensemble. However, it is refocusable using a Hahn Echo [48] or Carr-Purcell-Meiboom-Gill (CPMG) [49] sequence, shown in Fig. 4.5. This results in a spin echo, which is also proportional to the magnetization, and whose amplitude decays with the dipole-dipole interaction limited T_2. In case of the ^{31}P spins, there is a large difference between the T_2^* and T_2, which are 100 μs and 16 ms respectively in natural abundance silicon [7], and 2 ms and 1.2 s respectively, in ^{28}Si enriched silicon [4]. Therefore, if we perform each detection using a CPMG sequence instead of just the FID, we can potentially boost the SNR by a factor of $2\sqrt{\frac{T_2}{5T_2^*}} \simeq 24$ [50]. The data processing involved treating the measured signal between each pair of refocusing pulses as an individual acquisition and averaging the amplitude of the complex signal over these acquisitions. Other approaches in literature include fourier transforming the entire time domain record, resulting in spikelets whose linewidth is given by the T_2, and an envelope giving the T_2^* limited lineshape. A detailed analysis of these approaches can be found in [50] and [51]. This approach was implemented after the experiments for Ch. 5 were completed, since SNR was not a limiting factor there. It was also not used for ^{29}Si detection, since the disparity between T_2^* and T_2 is much lower (factor of 4) in this case, limiting the potential SNR gain. The true boost in SNR for the ^{31}P measurements is closer to a factor of 16.

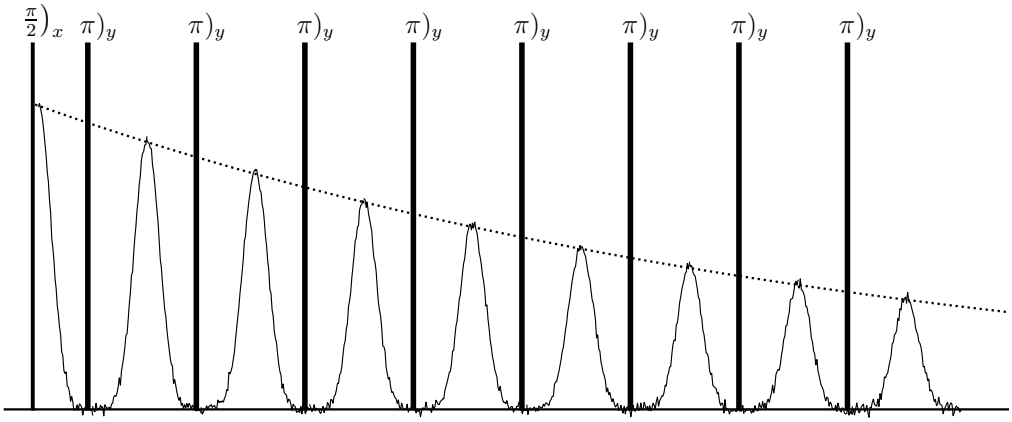

Figure 4.5: Acquisition using the Carr-Purcell-Meiboom-Gill (CPMG) pulse sequence, which was used to measure the ^{31}P nuclear spin signal in natural abundance silicon. The solid rectangular blocks are pulses, while the solid line indicates the acquired signal. The sequence consists of a $\frac{\pi}{2})_x$ readout pulse, followed by a delay τ which includes detection of the FID. This is followed by refocusing pulses $\pi)_y$, and a delay of 2τ during which the echo is detected. The dotted line is a guide to the eye for the T_2 decay of the echo.

Chapter 5

^{31}P Dynamics under Optical Pumping

5.1 Introduction

Optical pumping of phosphorus-doped silicon has been shown to generate ^{31}P hyperpolarization in isotopically enriched ^{28}Si [4] as well as natural abundance silicon [7, 52]. There have been different proposals regarding the process that leads to this, with some suggesting that it is an Overhauser-like process driven by non-equilibrium phonons [52] and others suggesting that it relies on a transfer of angular momentum during formation of bound excitons (BEs) at the defect site [23]. These proposals both lead to similar predictions for the sign of the polarization, as well as its dependence on the light intensity, and are therefore hard to verify with a simple magnetic resonance measurement. Here, we demonstrate that NMR has the capability of probing the ionization of the defect sites, which is driven by the formation and recombination of BEs, due to changes in the resonance frequency of ^{31}P during this process. We exploit these capabilities to show that the hyperpolarization process in our system is predominantly phononic. We measure the defect ionization and photoneutralization rates by using the Bloch-McConnell equations [8], commonly used in the determination of chemical reaction rates. We also report a paramagnetic shift of 16 kHz on the ^{31}P nuclear spin in its ionized state, which has not been measured previously.

The experiments in this chapter focus on the ^{31}P nuclear spin in isotopically enriched ^{28}Si. The effect of the residual ^{29}Si is expected to be neglible, and it has not been possible to measure an inductively detected signal from these ^{29}Si. Therefore, we drop the ^{29}Si terms in Eq. 3.1 and consider the simplified Hamiltonian

$$H = \frac{\omega_e}{2}\sigma_z^e + \frac{\omega_P}{2}\sigma_z^P + \frac{A_{eP}}{4}\vec{\sigma}_e \cdot \vec{\sigma}_P \ . \tag{5.1}$$

5.2 Dynamics of Excitons Under Optical Pumping

The absorption of an above-bandgap photon in the sample leads to the creation of an electron-hole pair. This pair forms a quasiparticle known as a "free" exciton (FE), consisting of a conduction band electron free to move in the lattice, coupled to a hole [53]. The radiative lifetime of these FEs is very long (∼ms [23]) compared to the observed lifetimes, and the dominant relaxation channel is non-radiative relaxation via impurity sites [45, 54]. This mechanism involves the formation of BEs and bound multi-exciton complexes (BMECs) [55] at the defect sites, which then decay via an Auger recombination process. The likelihood of formation of BMECs is lower than that for BEs (≤ 5 % [55]), and we neglect them in our analysis. In this section, we will look at the BE formation and recombination process as well as the ability of NMR measurements to probe these in more detail.

5.2.1 A Three Step Process

The process driven by optical pumping with above-bandgap light is illustrated in Fig. 5.1. The FE is captured at a defect site, resulting in the formation of a BE. We label the state of the site in the presence of a BE as D^0X. This state consists of two electrons with identical spatial wavefunctions, occupying the lowest energy level of the defect potential. The Pauli exclusion principle dictates that their spins must form a singlet state. The hole is also localized to the defect site. The BE decays predominantly (99.99% [56]) through an Auger ionization process, where one of the electrons recombines with the hole, and the resulting energy is transferred as kinetic energy to the other electron. This second electron (called the Auger electron) is kicked from the shallow donor-bound state high into the conduction band as a free electron, where it relaxes to the bottom of the conduction band primarily through phonon emission. Since the Auger electron has an excess kinetic energy of ~ 1 eV, much higher than the binding energy of the defect, it can ionize other defect sites which have not formed a bound exciton yet, either through a direct collision or through emission of high energy phonons into the lattice. The affected defect sites (including the one that originally formed the BE) are left in an ionized state (which we label as D^+) for some time before the capture of a free electron in the conduction band returns the defect to its neutral state (which we label as D^0). The D^0 state can then capture another FE to form the D^0X state, continuing the cycle. This leads to a steady state in the lattice where the number of defect sites in the D^0, D^0X and D^+ states is determined by the relative rates of each of these processes.

We label the rates associated with these transitions as $\kappa_{D^0 \to D^0X}$, $\kappa_{D^0X \to D^+}$, $\kappa_{D^0 \to D^+}$ and $\kappa_{D^+ \to D^0}$. $\kappa_{D^0 \to D^0X}$ denotes the rate at which FEs are captured at the donor sites. This is proportional to the number of FEs available in the conduction band, which is in turn proportional to the applied laser intensity. Therefore, we expect $\kappa_{D^0 \to D^0X} \propto I$. Similarly, nearly every FE capture will result in the formation of an Auger electron, since this is the primary decay mechanism. Each Auger electron, on average, will ionize a certain number of other defect sites. Therefore, direct ionization of defect sites by the Auger electron (given by $\kappa_{D^0 \to D^+}$) is proportional to $\kappa_{D^0 \to D^0X}$, and in turn proportional to I. On the other hand, the rate of recombination ($\kappa_{D^+ \to D^0}$) is proportional to the number of free electrons available in the conduction band, which scales as the square root of the laser intensity [5, 57]. Therefore, $\kappa_{D^+ \to D^0} \propto \sqrt{I}$. We will denote the constants of proportionality for $\kappa_{D^0 \to D^0X}$ and $\kappa_{D^+ \to D^0}$ as $\alpha_{D^0 \to D^0X}$ and $\alpha_{D^+ \to D^0}$ respectively, and the average number of impact ionizations driven by every Auger electron as n_a, such that $\kappa_{D^0 \to D^+} = n_a \kappa_{D^0 \to D^0X}$. The lifetime of the BE (and therefore the D^0X state) has been measured to be 272 ns [56], and we will use this value in our analysis. This is expected to be short compared to the lifetime of the D^+ state, which in turn is short compared to the lifetime of the D^0 state. Therefore, we expect that $\kappa_{D^0X \to D^+} \gg \kappa_{D^+ \to D^0} \gg (\kappa_{D^0 \to D^0X}, \kappa_{D^0 \to D^+})$.

5.2.2 ^{31}P Nuclear Spin Hamiltonian

The ^{31}P nuclear spin in the D^0 state sees a strong contact hyperfine interaction with the donor electron of 117.53 MHz. However, in the D^0X state, there are two electrons in the ground state of the donor potential with identical spatial wavefunctions, forming a spin singlet. Therefore, the contact hyperfine interaction seen by the ^{31}P nuclear spin vanishes in the D^0X state. The ^{31}P can still experience a hyperfine shift due to interaction with the hole (A_h), which is a spin-3/2 particle. The strength of this interaction has not been measured to date. However, it has been estimated to be 2 MHz [58], and can be upper bounded, based on the lack of an observable effect in photoluminescence (PL) measurements, to ~ 20 MHz, given by the PL linewidth [59]. In the D^+ state, there are no electrons or holes with significant overlap or proximity to produce any observable local field on the ^{31}P. Therefore, the ^{31}P resonance frequency in the D^+ state should be given purely by the gyromagnetic ratio. However, the local electronic configuration can also generate a small field, leading to a paramagnetic shift $\delta\omega$.

Let us first consider the D^0 state. At 6.7 T and 1.3 K, the electron is polarized to 99.8%. We perform our measurements at 174 MHz ($= \omega_P + \frac{A_{eP}}{2}$ at 6.7 T), with an

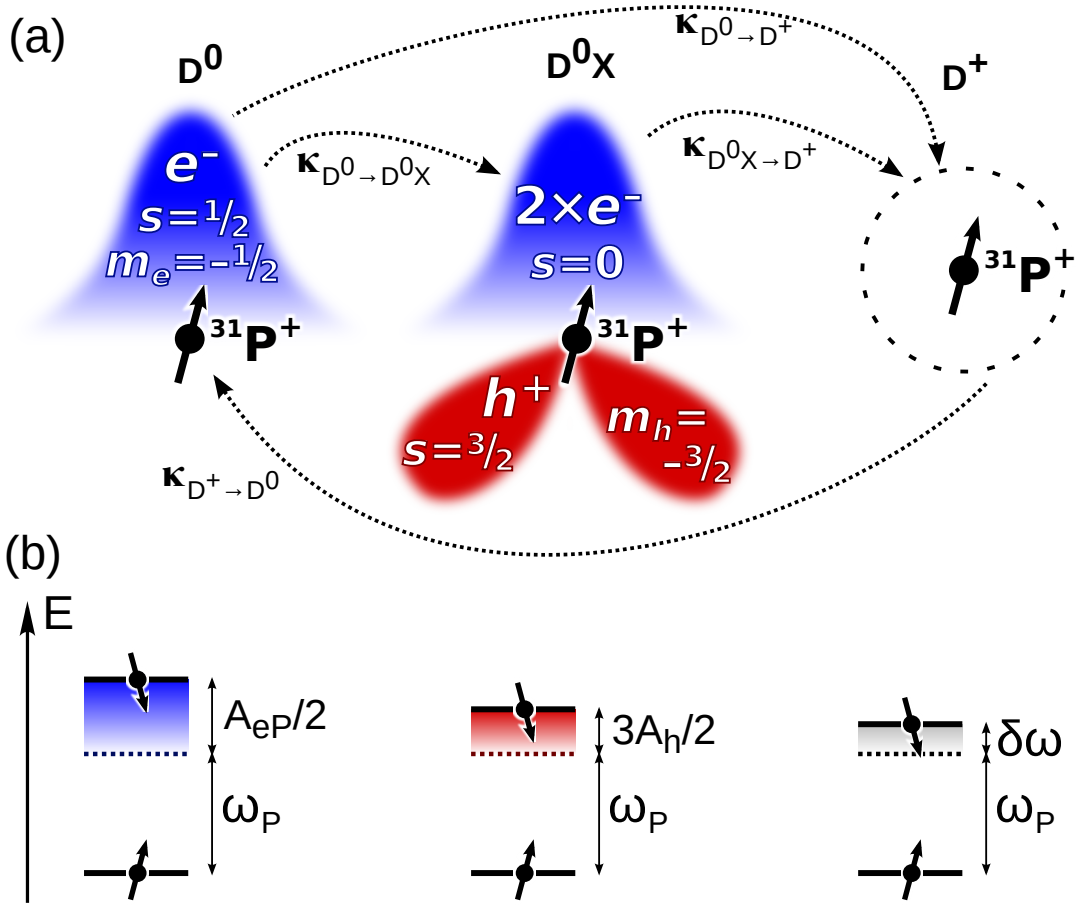

Figure 5.1: (a) An illustration of the process seen by the ^{31}P spin under optical pumping, with the associated rates. The neutral donor D^0 captures a free exciton to form the bound exciton state D^0X. The bound exciton recombines via the Auger ionization process, leaving behind an ionized donor D^+. The ionized donor is photoneutralized by the capture of a free electron, driving it back to the D^0 state. Finally, the neutral donor D^0 may be directly ionized, for e.g. by impact with high energy electrons, into the D^+ state. (b) The ^{31}P spin energy levels in the three states. Here, ω_P is the Zeeman splitting, A_{eP} is the hyperfine interaction with the defect electron, A_h is the hyperfine interaction with the hole and $\delta\omega$ is the paramagnetic shift in the D^+ state

excitation bandwidth ~ 30 kHz. The detection bandwidth, given by the quality factor of the tank circuit, is ~ 100 kHz. Therefore, we will only detect nuclear spins conditional on the electron spin being in the ground state. The only observable effect of the other manifold is expected to be the effective T_2^n process driven by the electron T_1^e. Therefore, we can write the effective nuclear spin Hamiltonian in the D^0 state as

$$H_{D^0}^{\text{eff}} = \left(\frac{\omega_P}{2} + \frac{A_{eP}}{4}\right)\sigma_z \ . \tag{5.2}$$

In the D^0X state, the hole can have a significant hyperfine interaction with the nuclear spin. The hole has an extremely short T_1 [58], such that it thermalizes well within the BE lifetime of 272 ns. We will assume that it is mostly in its ground state, leaving us with an effective nuclear spin Hamiltonian

$$H_{D^0X}^{\text{eff}} = \left(\frac{\omega_P}{2} + \frac{3A_h}{4}\right)\sigma_z \ . \tag{5.3}$$

In the D^+ state, there is no interaction apart from the Zeeman interaction and a potential paramagnetic shift. Therefore, the Hamiltonian is given by

$$H_{D^+} = \frac{(\omega_P + \delta\omega)}{2}\sigma_z \ , \tag{5.4}$$

where $\delta\omega$ is the paramagnetic shift.

We have not been able to experimentally observe an NMR signal from the D^0X or D^+ states directly. This is not surprising, since their population is expected to be much smaller than that of the D^0 state, and lifetimes relatively short. This would result in a small, broadened signal that is extremely hard to detect. However, the lifetimes of these states are long enough that a resonant RF field would modify the nuclear spin state each cycle, resulting in a change in the observed spin polarization in the D^0 state after the defect undergoes several cycles of the three step process. Since the optical pumping which drives this three step process is also responsible for the buildup of ^{31}P polarization, we can perform time dependent measurement of the polarization growth in the D^0 state while saturating on the D^0X and D^+ resonances. Every time the defect is driven to the D^0X and D^+ states, it gets slightly depolarized by the drive. Therefore, we expect the measured D^0 polarization to decrease as a function of the saturation drive strength and frequency.

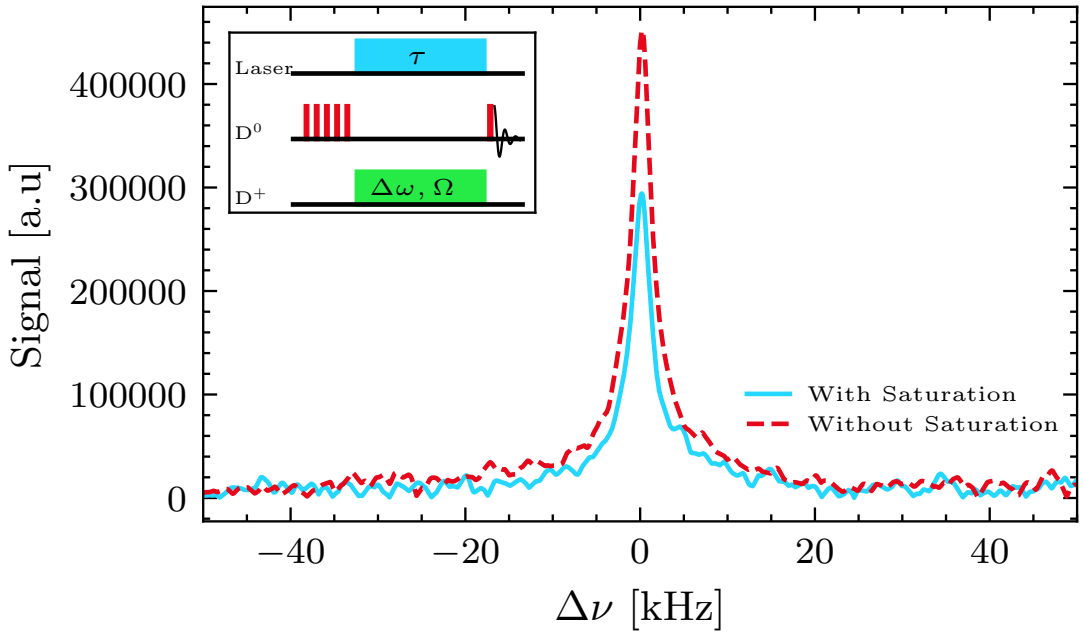

Figure 5.2: A comparison of ^{31}P spectra in the D^0 state, with (blue, solid) and without (red, dashed) a saturation drive at the D^+ frequency during optical pumping at 1.3 K. The reduction in polarization in the presence of saturation demonstrates that we can observe the defect ionization process with our pump-probe type experiment, illustrated in the inset. The reference frequency ($\Delta\nu = 0$) is 174.105 MHz. Inset: The experimental sequence consists of a saturation train on the D^0 state, to ensure no initial polarization, followed by optical pumping for duration τ, while simultaneously saturating at a frequency $\Delta\omega$ away from the ^{31}P Zeeman frequency at 6.7 T (115.312 MHz) with a drive strength Ω. The measurement is performed with a $\pi/2$ pulse followed by detection of the FID at the end of the optical pumping duration, after a wait time of 0.5 s to ensure that the laser is completely off. For the data in the main figure, $\tau = 480$ s, $\Delta\omega = -19$ kHz and $\Omega = 240$ Hz were used.

5.3 Experimental Setup

All experiments in this chapter were conducted at a temperature of 1.3 K and in a magnetic field of 6.7 T. The sample was a 8 mm × 2 mm × 2 mm single crystal of isotopically enriched ^{28}Si. Our approach can be described as a pump-probe type experiment, where we saturate (pump) at or close to the resonance of the bare ^{31}P Zeeman frequency of 115 MHz and measure (probe) the polarization in the hyperfine shifted D^0 state at 174 MHz. This was implemented on the single channel split-resonance probe described in Ch. 4, using the two output channels of the spectrometer. The effect of this on the ^{31}P polarization at 174 MHz can be seen in Fig. 5.2, with the experiment scheme shown in the inset. We use a low noise amplifier (LNA) at room temperature and a bandpass filter around 115 MHz for experiments with $\Omega \leq 1$ kHz, as shown in Fig. 5.3. For the experiment with $\Omega \simeq 4$ kHz, the required power output was higher than the maximum output from the LNA. The Bruker spectrometer amplifier was used instead, and the effect of amplifier noise was measured to have $\ll 5\%$ error on the effective Ω. In order to extract the defect ionization and recombination rates, we need to calibrate the Rabi frequency Ω. However, the lack of an observable NMR signal at 115 MHz necessitates an indirect calibration using the 174 MHz channel, which was performed as follows:

1. A broadband pickup coil was placed ~ 5 mm away from the coil and the voltage generated across it by the saturation pulse was recorded during the experiments. This voltage is proportional to the applied Rabi field B_1 at the sample, with a constant of proportionality determined by the pickup coil inductance as well as geometric factors.

2. At 174 MHz, the effective field [1] at the sample (B_1) under the application of a pulse was calculated as

$$B_1 = \frac{2\Omega}{\gamma_P + \frac{A_{eP}}{2B_0}} ,$$

where Ω is the Rabi frequency, calculated from a standard Rabi experiment on the D^0. By measuring the induced voltage across the coil during the Rabi experiment, the constant of proportionality was determined. Differences in circuit properties

[1] This is different from the field generated by the coil due to what is known as the "hyperfine enhancement" [60]. Since the RF drive at 174 MHz is slow compared to the electron Larmor frequency of 188 GHz, it adiabatically rotates the electron spin. This results in an effective time dependent modulation of the hyperfine coupling, which is experienced by the nuclear spin as an additional RF field. The resulting enhancement of the effective Rabi frequency is a well known effect in electron-nuclear double resonance experiments.

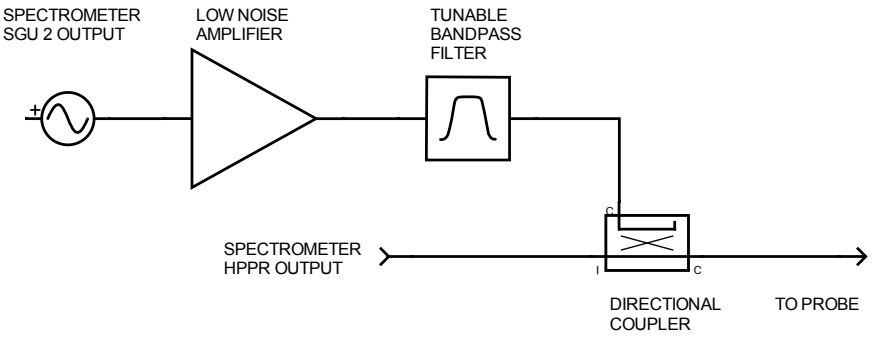

Figure 5.3: The $\sim$ 115 MHz saturation drive is generated with the spectrometer's Signal Generating Unit (SGU 2), amplified by the LNA (Mini Circuits ZHL-32A), filtered through a bandpass filter (K & L, tunable) and then coupled to the input of the single channel probe through a directional coupler (Werlatone C5964, 30 dB)

at the two frequencies will result in a constant of proportionality that is frequency dependent. Therefore, a transmission measurement was performed to verify that the response of the broadband coil was flat over the frequency range.

5.4 ^{31}P Hyperpolarization Mechanism

The effect of above-bandgap optical pumping below the metal-insulator transition resulting in ^{31}P hyperpolarization has been observed experimentally on multiple occasions [4, 7, 23, 52] with conflicting theoretical proposals for the dominant process [23, 52], and very little experimental evidence that can distinguish between the two. In this section, we expand on the Overhauser-like process proposed by McCamey further [52], and present experimental evidence which suggests that this is the dominant mechanism under our experimental conditions.

5.4.1 Bound Exciton Capture Dependent Model

Let us first take a look at the angular momentum transfer model proposed by Sekiguchi et. al [23], without constraining its mathematical form. FE electrons in silicon under

above-bandgap pumping are very well thermalized, with extremely short spin-relaxation times ($\sim$ ns or lower). We also expect to start with a thermally polarized defect electron spin in the beginning of the optical pumping process, since no microwave control is applied and the T_1^e in the D^0 state is not particularly long ($\sim$ ms) in the absence of light. On the other hand, we noted earlier that the combined state of the two electrons in the BE must be a spin-singlet. Therefore, at high fields and low temperature, when the electron thermal state is highly polarized, the BE capture must involve transfer of angular momentum away from the electron spins. Sekiguchi et al. proposed a mechanism for BE capture, where a simultaneous electron-nuclear spin flip transfers the angular momentum to the nuclear spin for the $\sim 50\%$ of the defects which have nuclear spins in the $|\uparrow_P\rangle$ state to begin with, such that the formation of BEs preferentially drives the nuclear spins into the $|\downarrow_P\rangle$ state. They note that the BE capture can also occur via an intermediate state where the captured electron is initially in the barely bound $1s\Gamma_{3,5}$ valley-orbit excited states, where it can be in the same spin state as the defect electron spin, until the spin-orbit coupling flips one of the electron spins. Below, we list some of the predictions expected from a model where the nuclear spin-flip mediated mechanism dominates and is primarily responsible for the hyperpolarization of ^{31}P nuclear spins.

- The conserved quantity is the angular momentum. The gyromagnetic ratios of the ^{31}P and electron spins are opposite in sign. Therefore, the result will be a nuclear spin "anti-hyperpolarization" (AHP), where the population of the nuclear spin is driven to its excited state, rather than the ground state.

- The rate of hyperpolarization will be proportional to the rate of formation of BEs ($\kappa_{D^0 \rightarrow D^0X}$), which is in turn proportional to the laser intensity I. The steady state that this process drives to, on the other hand, will always be set by the electron spin polarization.

- If the nuclear-spin mediated capture is indeed the dominant channel for BE formation, this formation will be slowed as the nuclear spin becomes polarized, since the D^0 sites with a polarized nuclear spin can no longer accept the angular momentum from the electron spin. Therefore, the capture cross-section i.e. the probability of capture for a given FE, must decrease. This will also lead to an increase in the steady state FE concentration in the sample, since the dominant relaxation pathway, which is the formation of BEs, is now suppressed. Therefore, if the nuclear-spin mediated capture is dominant, then $\alpha_{D^0 \rightarrow D^0X}$ must be significantly dependent on the nuclear spin polarization. If a mechanism not involving the nuclear spin dominates, $\alpha_{D^0 \rightarrow D^0X}$

will be completely independent of the nuclear polarization. For an intermediate situation, where both channels compete, the effect of the nuclear spin polarization on $\alpha_{D^0 \to D^0 X}$ is non-zero but non-trivial. We will not attempt to model it here.

We noted that the rate of polarization in this model depends on the number of FEs available for capture. However, the mean free path of FEs in silicon is ~ 24 μm [45, 61], which is much smaller than the mm scale variation of light intensity over the sample due to the presence of the coil. Therefore, we expect that the nuclear spin polarization rate in this model will be proportional to the local light intensity and not the average power over the sample. The ^{31}P nuclear spin polarization in different parts of the sample is expected to grow at different rates under such a model, such that the overall polarization is given by

$$\langle \sigma_z \rangle(t) = \int_V \eta(I) p_{ss}(I,t) \ , \tag{5.5}$$

where $p_{ss}(I,t)$ is the local light intensity-dependent polarization function. We note that in the case where the nuclear-spin mediated capture is the dominant process, the mean free path should increase as the FE capture cross section goes down. If the mean free path exceeds mm, it may average out the light intensity variation.

5.4.2 Phononic Model

Now, let us consider the model proposed by McCamey et al. [52], where they suggested that the nuclear hyperpolarization is a result of the electron spin-lattice relaxation (T_1^e) being driven to a different effective temperature compared to the electron-nuclear cross-relaxation (T_x).

We first consider the effect of strain on the electron-nuclear spin system. Incorporating the strain dependence of the hyperfine coupling shown in Eq. 2.5, we can write the total Hamiltonian for the electron-^{31}P spin system as

$$H = \frac{\omega_e}{2}\sigma_z^e + \frac{\omega_P}{2}\sigma_z^P + \frac{A_{eP}}{4}\left(1 + \vec{\nabla} A_{eP}.\vec{\varepsilon} + \frac{1}{2}\vec{\varepsilon}.\mathbf{H}_{A_{eP}}.\vec{\varepsilon}\right)\vec{\sigma}^e.\vec{\sigma}^P \ . \tag{5.6}$$

The absorption of above-bandgap light in the sample leads to emission of phonons in the lattice, resulting in a time-dependent strain at the nuclear spin site. This strain can be modeled as a sum over elastic waves of frequencies $\{\omega_i\}$ originating from a set of randomly distributed sources at $\{\vec{r}_j\}$. Therefore, the strain is given by

$$\vec{\varepsilon}(t) = \sum_i \sum_{j=1}^{N_i} \vec{\varepsilon}_i(\vec{r}_j)\cos(\omega_i t + \zeta_{ij}) \ , \tag{5.7}$$

where N_i is the number of waves at frequency ω_i and the phase ζ_{ij} is a uniformly distributed random variable. Since number of waves is proportional to laser intensity, the sum over random phases yields

$$\vec{\varepsilon}(t) = \sqrt{I} \sum_i \vec{\epsilon}_i \cos(\omega_i t + \zeta_i) \ , \tag{5.8}$$

where I is the laser intensity. $\vec{\epsilon}_i$ is a mode dependent photon to phonon yield constant, which captures the photon absorption efficiency as well as the frequency distribution of the emitted phonons. Substituting Eq. 5.8 in Eq. 5.6, going into the rotating frame of $\frac{\omega_e}{2}\sigma_z^e + \frac{\omega_P}{2}\sigma_z^P$ and performing the rotating wave approximation, the Hamiltonian can be simplified to

$$\begin{aligned} H_{\text{sec}} \simeq \frac{A_{eP}}{4}\sigma_z^e\sigma_z^P + \sqrt{I}\frac{A_{eP}}{4}\left(\sum_{\substack{\omega_i = \\ \omega_e - \omega_P}} \vec{\nabla} A_{eP}.\vec{\epsilon}_i\right)\left(\sigma_+^e\sigma_-^P + \sigma_-^e\sigma_+^P\right) \\ + I\frac{A_{eP}}{8}\left(\sum_{\substack{\omega_i \pm \omega_k = \\ \omega_e - \omega_P}} \vec{\epsilon}_i.\mathbf{H}_{A_{eP}}.\vec{\epsilon}_k\right)\left(\sigma_+^e\sigma_-^P + \sigma_-^e\sigma_+^P\right) \ . \end{aligned} \tag{5.9}$$

While we have described the action of phonons using Hamiltonians, we note that this is not expected to be a coherent process. The phonon lifetimes are short ($\leq \mu$s) compared to the timescales of these perturbations, which are ∼kHz or smaller. There is also no phase coherence between subsequent phonons at a given site or between phonons at different sites. Therefore, the modulation of the hyperfine interaction will drive an incoherent cross-relaxation process between the electron and ^{31}P spin. The process will also have an associated "temperature" with it, rather than simply equalising the populations of the two levels. In particular, in the absence of any laser excitations, the effect of the thermal phonons will be to drive the cross-relaxation to a Boltzmann distribution given by the lattice temperature, with $\mathrm{T}_x \sim 10^4$ s [62]

The effective Hamiltonian in Eq. 5.9 indicates that it will result in cross-relaxation of the ^{31}P driven by either single phonon absorption ($\omega_i = \omega_e - \omega_P$), two phonon absorption ($\omega_i + \omega_j = \omega_e - \omega_P$) or Raman scattering ($\omega_i - \omega_j = \omega_e - \omega_P$) processes. While the linear term in strain for the ^{31}P hyperfine interaction is non-zero for the hydrostatic component, it is symmetry constrained to be zero for any deviatoric strain. Therefore, we expect that the two phonon/Raman processes, which involve an integration over the entire phonon spectrum, will drive the cross-relaxation between the electron and ^{31}P. This was verified experimentally by Nakayama and Hasegawa for thermal phonons [62], where

they concluded that the cross-relaxation (in the absence of large static strains) is primarily a Raman process. Therefore, we expect that the cross-relaxation rate is proportional to the laser intensity i.e. $T_x^{-1} \propto I$. On the other hand, the electron relaxation is driven primarily by single phonon processes, as well as by thermalization through the conduction band electrons during the defect ionization and photo-neutralization process. In the presence of above-bandgap optical pumping, the steady state phonon distribution cannot be described by a single temperature, since the electron decay will preferentially populate some phonon modes and will not follow a Boltzmann distribution. Therefore, the electron relaxation, driven primarily by single phonon processes and interaction with conduction band electrons, can be driven to a different quasi-temperature T_e, compared to the two phonon/Raman driven cross-relaxation, whose effective temperature we label as T_p. In particular, we expect $T_e \leq T_p$ for two reasons:

- The FEs are expected to be very well thermalized to the bath temperature [23], preventing T_e from deviating significantly. Increasing laser power, while increasing the number of non-thermal phonons, also increases the frequency of defect ionization events, thus increasing the thermal contact of the defect electron spin with the FE electrons.
- The two-phonon/Raman process samples a larger number of non-equilibrium phonons generated by the optical pumping, compared to the single phonon process, which can only be affected by the increase in population of the ~ 188 GHz phonon mode.

Pines, Bardeen and Slichter [63] were the first to identify that an imbalance between the cross-relaxation and the electron spin-lattice relaxation timescales can result in a high transient nuclear polarization. Feher [35] noted that driving these two processes to different temperatures will yield a steady state nuclear hyperpolarization rather than a transient one, and that the spin temperature of defect electrons can be different from that of the phononic bath driving a cross-relaxation, in particular under a DC electric field based injection of "hot" conduction band electrons. This idea was extended by McCamey and co-workers [52] to the optical pumping process, where they proposed that the emission of phonons due to the indirect bandgap of silicon will result in a phononic quasi-temperature T_p that can be higher than that of the defect electron spins, which are primarily thermalized to the conduction band electrons. Our primary contribution to the theory is to point out, through the above analysis, that it is not just the thermalization via conduction band electrons, but also a difference in the phonon modes contributing to the two processes that can create a temperature difference.

Here, we derive this result using the language of open quantum systems [64]. Electron spin relaxation to a thermodynamic temperature T_e with a timescale T_1^e is given by the Lindblad operators

$$L_{\pm}^{e} = \sqrt{\frac{1 \pm p_e}{2\mathrm{T}_1^e}}\sigma_{\pm}^{e} \ , \qquad\qquad p_e = \tanh\left(\frac{\hbar\omega_e}{2k_{\mathrm{B}}T_e}\right) \ ,$$

where p_e is the electron thermal polarization at temperature T_e. If the cross-relaxation is driven to a different equilibrium temperature T_p over a timescale T_x, the process can be written with the Lindblad operators

$$L_{\pm}^{en} = \sqrt{\frac{1 \pm p_x}{2\mathrm{T}_x}}\sigma_{\pm}^{e}\sigma_{\mp}^{P} \ , \qquad\qquad p_x = \tanh\left(\frac{\hbar(\omega_e - \omega_P)}{2k_{\mathrm{B}}T_p}\right) \ ,$$

where p_x is the equilibrium polarization for the cross-relaxation process at temperature T_p. Therefore, we can write down the master equation for the process, as given by Eq. 1.10, as

$$\begin{aligned}
\frac{d\rho}{dt} = &-i\left(\frac{\omega_e}{2}[\sigma_z^e,\rho] + \frac{\omega_P}{2}[\sigma_z^P,\rho] + \frac{A_{eP}}{4}[\sigma_z^e\sigma_z^P,\rho]\right) \\
&+ \left(\frac{1-p_e}{4\mathrm{T}_1^e}\right)\left(2\sigma_+^e\rho\sigma_-^e - \sigma_-^e\sigma_+^e\rho - \rho\sigma_-^e\sigma_+^e\right) + \left(\frac{1+p_e}{4\mathrm{T}_1^e}\right)\left(2\sigma_-^e\rho\sigma_+^e - \sigma_+^e\sigma_-^e\rho - \rho\sigma_+^e\sigma_-^e\right) \\
&+ \left(\frac{1-p_x}{4\mathrm{T}_1^x}\right)\left(2\sigma_-^e\sigma_+^P\rho\sigma_+^e\sigma_-^P - \sigma_+^e\sigma_-^P\sigma_-^e\sigma_+^P\rho - \rho\sigma_+^e\sigma_-^P\sigma_-^e\sigma_+^P\right) \\
&+ \left(\frac{1-p_x}{4\mathrm{T}_1^x}\right)\left(2\sigma_-^e\sigma_+^P\rho\sigma_+^e\sigma_-^P - \sigma_+^e\sigma_-^P\sigma_-^e\sigma_+^P\rho - \rho\sigma_+^e\sigma_-^P\sigma_-^e\sigma_+^P\right) \ .
\end{aligned} \tag{5.10}$$

The steady state of the system under this process is achieved when $\frac{d\rho}{dt} = 0$. This is equivalent to calculating the zero-eigenvalue eigenvector of the superoperator $\mathcal{L}$, which can be written explicitly using Roth's lemma as demonstrated in Eq. 1.12 and solved analytically. The resulting steady state density matrix is given by

$$\rho_{\mathrm{eq}} = \left(\frac{1}{2}\mathbb{1}^e + \frac{p_e}{2}\sigma_z^e\right) \otimes \left(\frac{1}{2}\mathbb{1}^P + \frac{p_n}{2}\sigma_z^P\right) \ , \tag{5.11}$$

where $p_n = \frac{p_e - p_x}{1 - p_e p_x}$ is the effective nuclear spin polarization. Assuming that the defect electron spin temperature is the same as the helium bath and that the laser induced phonons will result in the quasi-temperature $T_p > T_e$, we expect a negative nuclear hyperpolarization, in agreement with the experimental results [4]. Fig. 5.4 shows how the induced nuclear polarization depends on the effective cross-relaxation temperature T_p. It is clear that a small imbalance between the two baths is capable of generating large nuclear polarizations. In particular, the lower bounds measured by Gumann et. al. [4] would require

$T_p \geq 11.17$ K at 4.2 K and $T_p \geq 1.7$ K at 1.3 K respectively. The time dependence of the nuclear polarization can be calculated, starting from an initial state corresponding to a thermal electron spin polarization and unpolarized ^{31}P spin state, by solving the master equation, as

$$\langle \sigma_z^P \rangle(t) = \mathrm{Tr}\left(\sigma_z^P \cdot \exp\left(\mathcal{L}t\right) \cdot \left(\frac{\mathbb{1}}{2} + \frac{p_e}{2}\sigma_z^e\right)\right) \ . \tag{5.12}$$

While the analytical solution for this in the general case exists, it is long and uninformative. It can be simplified under the assumption that $\mathrm{T}_1^e \ll \mathrm{T}_x$, which is always true in our system. Then, the ^{31}P polarization growth as a function of time is given by

$$p(t) = p_n\left(1 - \exp\left(-\frac{t}{\mathrm{T}_1^{\mathrm{D}^0}}\right)\right) \ , \tag{5.13}$$

where

$$\mathrm{T}_1^{\mathrm{D}^0} = \frac{2\mathrm{T}_x}{(1 - p_e p_x)} \ . \tag{5.14}$$

and the superscript indicates that the polarization growth only occurs while the defect is in the D^0 state. For high magnetic fields and laser intensities, such that $-p_x \ll -p_e \leq 1$, we expect $p_n \sim p_e$ and $\mathrm{T}_1^{\mathrm{D}^0} \propto \mathrm{T}_x \propto I^{-1}$. However, p_n can be smaller at lower laser powers under this model, unlike the BE capture driven one where p_n always equilibriates to p_e.

5.4.3 Experimental Results

The probability density function for the local light intensity shown in Fig. 5.5 shows that the laser intensity varies significantly over the sample at 1.3 K. The simulation indicates that the variation in laser intensity happens over mm length scales, due to the spacing between the coil turns which is ∼1 mm. Fig. 5.6 shows the time dependent buildup of ^{31}P polarization at three different laser powers, which are good fits to an exponential process with a single time constant. The inset to the figure shows a linear fit to the inverse of the fitted time constants, indicating that the time constant scales approximately as $\mathrm{T}_1^{\mathrm{D}^0} \propto I^{-1}$, which is in agreement with the expectation from both the phononic and BE capture models. Fig. 5.7 shows that a fit which assumes that the local polarization growth rate is determined by the local light intensity and integrates over the distribution $\eta(I)$ results in a poor fit to the time dependent buildup curve, in comparison to the fit to a local light intensity independent growth rate. We believe that the data excludes the possibility of a local light intensity dependent process. This is in favor of a phononic process, since the mean free

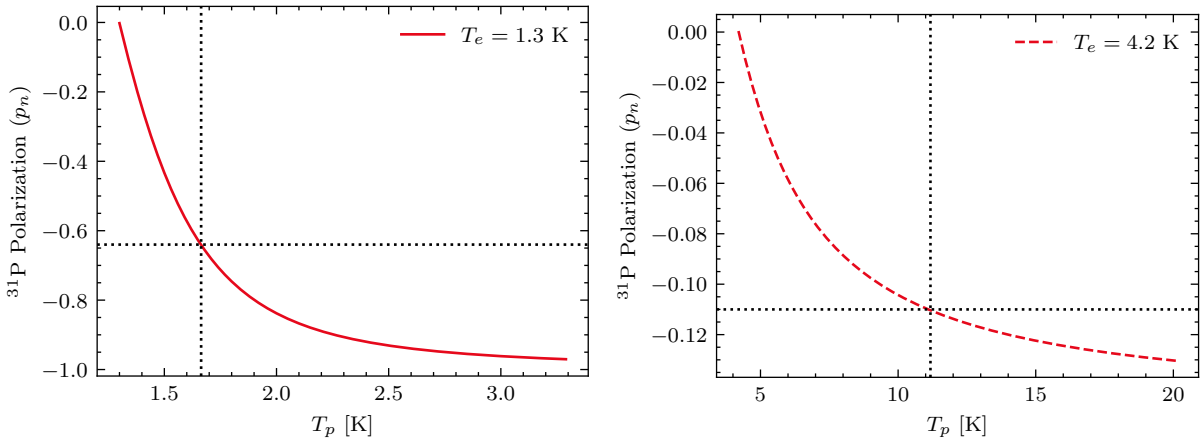

(a) (b)

Figure 5.4: Simulated ^{31}P polarization as a function of the effective cross relaxation temperature T_p for 1.3 K (a) and 4.2 K (b). The dotted lines indicate the polarization and corresponding T_p for the lower bounds measured in [4], which were -64% for pumped LHe temperature, yielding $T_p = 1.7$ K for $T_e = 1.3$ K and -11% for 4.2 K (with a laser time constant of 577 s and a thermal T_1^n of 712 s), yielding $T_p = 11.17$ K for $T_e = 4.2$ K

path of acoustic phonons, which we expect will contribute to the hyperpolarization process, are ∼mm. It does not immediately exclude the BE capture driven process since, as noted earlier, the mean free path of FEs can also increase to average out the intensity variation effects, if the nuclear spin driven BE capture is the dominant FE relaxation channel.

However, if the nuclear spin driven BE capture is indeed the dominant FE channel, the rate of capture at each site must be strongly dependent on the ^{31}P nuclear spin state. Let us consider the effect of a strong saturation drive on the D^+ state, such that the steady state at D^0 is a fully saturated nuclear spin. If we start from the high AHP state, most ^{31}P spins are in the $|\downarrow_P\rangle$ state. Therefore, the formation of BEs through angular momentum exchange between the electron and nuclear spin is suppressed, and the rate at which the nuclear spins see the saturation drive is determined by the $1s\Gamma_{3,5}$ state mediated capture rate. However, if we invert the ^{31}P polarization with a π-pulse, the situation is now reversed. Most ^{31}P spins are in the $|\downarrow_P\rangle$, able to exchange angular momentum with the FE electron. Therefore, the angular momentum exchange driven capture rate is now maximal, whereas the $1s\Gamma_{3,5}$ state mediated capture rate remains unchanged. Therefore, the contribution of the angular momentum exchange driven process to the BE capture rate should be observable as an asymmetry between the time dependent decay of ^{31}P polarization starting from these two different initial states. This is true even for a large n_a,

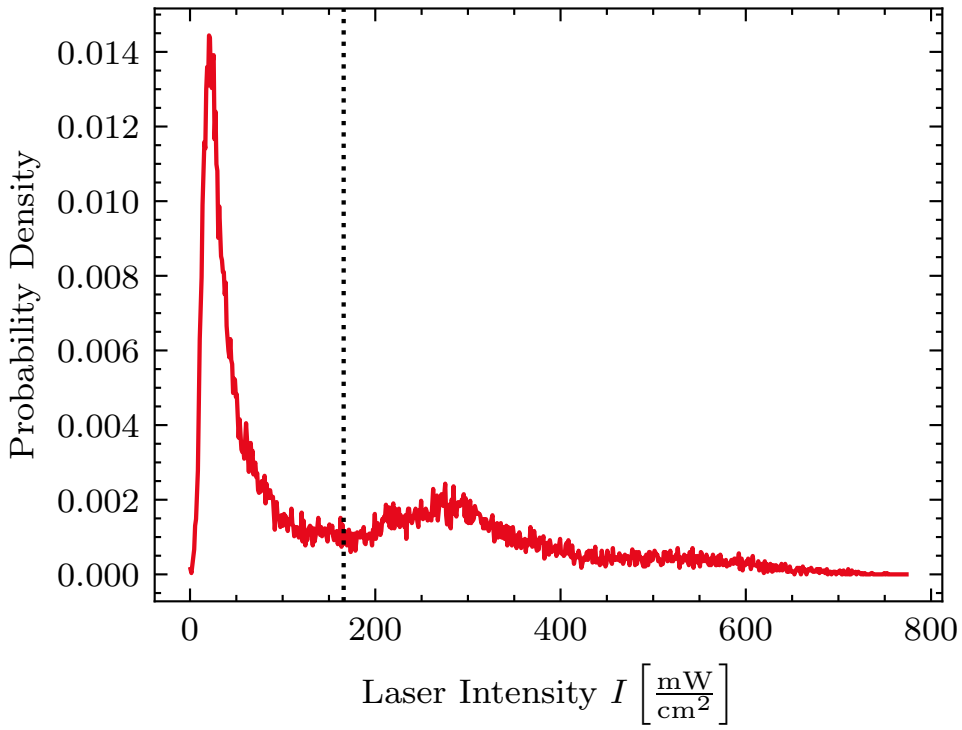

Figure 5.5: Probability density $\eta(I)$ vs laser intensity, derived from a COMSOL simulation of the steady state light distribution across the sample. The average intensity over the distribution is 166 $\frac{\mathrm{mW}}{\mathrm{cm}^2}$, indicated by the black dotted line.

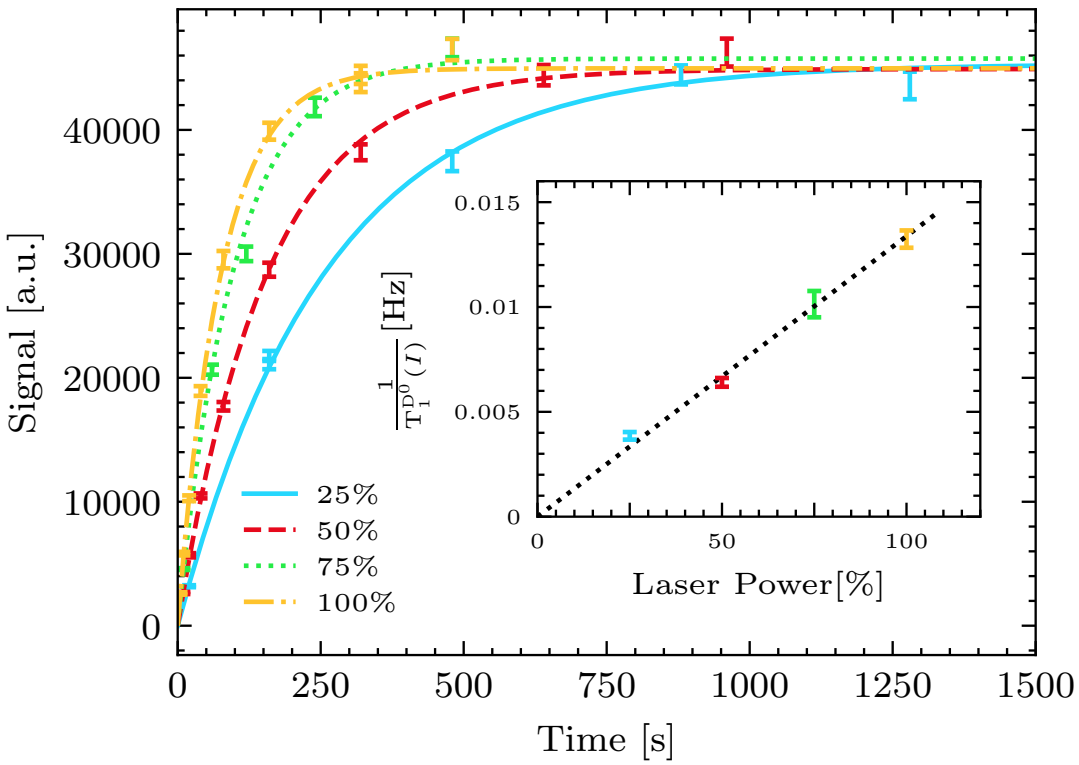

Figure 5.6: ^{31}P signal as a function of optical pumping duration with fits to an exponential buildup curve $S(t) = S_0\left(1 - \exp\left(-\frac{t}{T_1^{D^0}}\right)\right)$, for 25% (blue, solid), 50% (red, dashed), 75% (green, dotted) and 100% (dash-dotted, yellow) of the maximal laser power. The laser power was varied using the power supply and the output verified with a power meter. Inset: Inverse of the extracted time constants $T_1^{D^0}$, as a function of laser power. The dotted line is a linear fit. This confirms that the ^{31}P hyperpolarization rate is proportional to the laser power, as expected under the phononic model at high laser power.

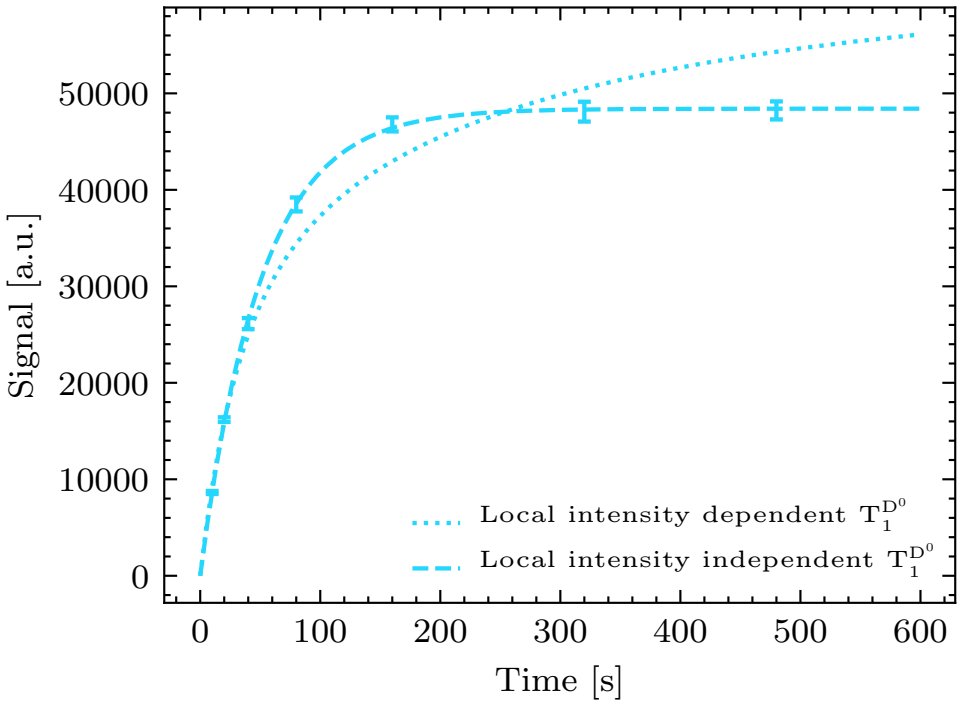

Figure 5.7: ^{31}P signal as a function of time. Dashed line is a fit to local intensity independent time constant $S(t) = S_0\left(1 - \exp\left(-\frac{t}{T_1^{D^0}}\right)\right)$. Dotted line is a fit to an inverse-linear local intensity dependence of the time constant $S(t) = S_0 \int \eta(I)\left(1 - \exp\left(-\frac{It}{t_1^{D^0}}\right)\right) dI$, where $\eta(I)$ is given in Fig. 5.5. The data is an excellent fit to the local light intensity independent model and a poor fit to the local light intensity dependent one, and demonstrates that the polarization timescale $T_1^{D^0}$ is independent of local light intensity.

but no longer true if there is a defect ionization process which is not conditional on BE formation. The likelihood of such a process will be discussed later in this chapter. The data in Fig. 5.8 shows that there is very little asymmetry between the decay in these two cases. This suggests that the BE capture and recombination is primarily driven by a ^{31}P spin state independent capture process, such as the $1s\Gamma_{3,5}$ state mediated one. This is also not sufficient, on its own, to exclude the possibility that the ^{31}P hyperpolarization is driven primarily by the BE capture process. Even if a small fraction of the BE capture events involve a nuclear spin flip preferentially to the $|\downarrow_P\rangle$ state, it will eventually polarize the nuclear spins, with a timescale longer than if the nuclear spin mediated process had dominated. However, such a process must also be local light intensity dependent, since the mean free path of the FEs is not significantly affected by the nuclear spin polarization.

The combined observations of a local light intensity independent polarization growth rate and a nuclear spin state insensitive defect ionization rate eliminates the possibility of the FE capture driven hyperpolarization process playing a significant role in our system. The observations are consistent with the phononic hyperpolarization process, leading us to conclude that this is the primary process driving ^{31}P hyperpolarization under above-bandgap optical pumping at 1.3 K.

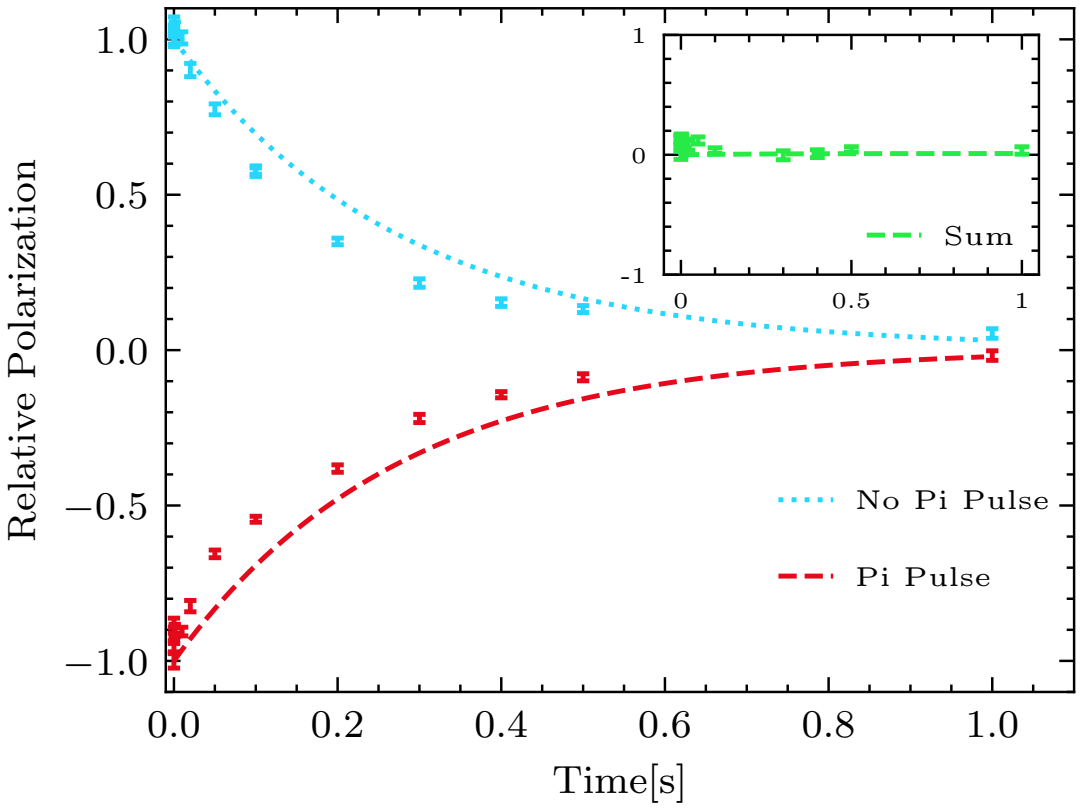

Figure 5.8: ^{31}P Polarization decay with time under optical pumping at maximal laser power and saturation with $\Omega = 4$ kHz. Starting from a state with $\sim 96\%$ of maximum polarization (160 s optical pumping without saturation), with (red) and without (blue) a π pulse in the beginning. The length of the π-pulse is 13 μs, and is treated as negligible. The signal amplitudes have been normalized to the t = 0 point. The lines indicate model predictions based on solutions to Eq. 5.17, with initial states $\langle\sigma_z\rangle^{\mathrm{D}^0} = 1$ (blue, dotted) and $\langle\sigma_z\rangle^{\mathrm{D}^0} = -1$ (red, dashed), and the parameters given by Table. 5.1, which have been extracted from the experiments shown in Fig. 5.10. Inset: Sum of the two signals at each time point, with the model predictions indicated by the green, dashed line. The symmetry observed in the measurement shows that the defect ionization rate is independent of the nuclear spin state. This suggests that the BE capture and recombination is driven primarily by a ^{31}P nuclear spin state independent capture process.

5.5 Extracting Defect Ionization and Photoneutralization Rates

Here, we use the saturation dependent measurements to extract the defect ionization and photoneutralization rates. Let us begin by convincing ourselves that the formation of BEs drives almost every defect ionization event.

Almost every photon absorbed into the silicon results in the creation of a FE [53], and almost every FE ($\sim$ 99.99% [56]) will decay through the BE formation and Auger recombination process. On the other hand, the thermal energy k_BT at 1.3 K (0.1 meV) is much smaller than the defect binding energy (45 meV), leaving no defect sites in a thermally excited state. The non-thermal phonons generated by the above-bandgap excitation can generate $\sim$12 meV of excess energy per photon (since the excitation is 1047 nm, compared to the 1058 nm bandgap). Therefore, one would require that the excess energy from absorption of 4 photons be transferred efficiently to a defect in order to ionize it in this manner. In comparison, the Auger electron has $\sim$1.127 eV of excess energy, sufficient to drive up to 25 impact ionizations on its own. Another potential source of ionization is the occasional direct absorption of the 1047 nm light by the defect site, and subsequent impact ionizations created by the resulting high energy electron. However, since the average number of these impact ionizations is approximately the same as that of the Auger electron, the relative contribution of this process to the overall number of defect ionizations will be the same as the fraction of photons absorbed that do not result in the formation of a BE, which is negligible. Therefore, it is reasonable to assume that almost every ionization event can be attributed to the formation of a BE.

5.5.1 Saturation Experiment and the Bloch-McConnell Equations

We have seen that saturation on resonance with D^+ reduces the polarization obtained. In order to use this effect to extract the defect ionization and photoneutralization rates, we derive an analytical form for the polarization as a function of saturation power and saturation frequency.

In the presence of the BE capture and recombination process, the spin sees a fluctuating Hamiltonian, depending on what state it is in. This is similar to the situation encountered in chemical exchange reactions, where the transition of the molecule between two chemical species A and B with different chemical shifts results in changes to the lineshape and magnetization, which can be probed by saturating parts of the line. It is possible to

analyse the evolution directly as that of a single spin seeing a fluctuating Hamiltonian [65]. However, McConnell [8] pointed out that it is much simpler and yet perfectly valid to treat the system as two ensembles of independent spin species, connected by a forward and reverse rate such that the total number of spins is conserved. The evolution of these ensembles is described by a modified set of Bloch equations, known as the Bloch-McConnell equations. We have 3 different "species" D^0, D^0X and D^+, connected by rates $\kappa_{D^0\to D^0X}$, $\kappa_{D^0X\to D^+}$, $\kappa_{D^0\to D^+}$ and $\kappa_{D^+\to D^0}$ that are sometimes one directional i.e. D^0X can only go to D^+ and not directly to D^0. Therefore, we can write Bloch-McConnell equations to describe the dynamics in this system, in the rotating frame at $\omega_c = \omega_P + \Delta\omega$, as

$$\frac{d}{dt}\begin{pmatrix}\langle\vec{\sigma}\rangle^{D^0}\\ \langle\vec{\sigma}\rangle^{D^0X}\\ \langle\vec{\sigma}\rangle^{D^+}\end{pmatrix} = \begin{pmatrix}\Lambda^{D^0} - \kappa_{D^0\to D^0X} - \kappa_{D^0\to D^+} & 0 & \kappa_{D^+\to D^0}\\ \kappa_{D^0\to D^0X} & \Lambda^{D^0X} - \kappa_{D^0X\to D^+} & 0\\ \kappa_{D^0\to D^+} & \kappa_{D^0X\to D^+} & \Lambda^{D^+} - \kappa_{D^+\to D^0}\end{pmatrix}\cdot\begin{pmatrix}\langle\vec{\sigma}\rangle^{D^0}\\ \langle\vec{\sigma}\rangle^{D^0X}\\ \langle\vec{\sigma}\rangle^{D^+}\end{pmatrix} + \begin{pmatrix}\langle\vec{\sigma}\rangle_e^{D^0}\\ \langle\vec{\sigma}\rangle_e^{D^0X}\\ \langle\vec{\sigma}\rangle_e^{D^+}\end{pmatrix}. \tag{5.15}$$

Here,

$$\Lambda^{D^0} = \begin{pmatrix}-\frac{1}{T_2^{D^0}} & -\frac{A_{eP}}{2} - \Delta\omega & 0\\ \frac{A_{eP}}{2} + \Delta\omega & -\frac{1}{T_2^{D^0}} & \gamma_P^{D^0}\frac{B_1}{2}\\ 0 & -\gamma_P^{D^0}\frac{B_1}{2} & -\frac{1}{T_1^{D^0}}\end{pmatrix}, \qquad \langle\vec{\sigma}\rangle_e^{D^0} = \frac{p_T^{D^0}}{T_1^{D^0}}\begin{pmatrix}0\\0\\1\end{pmatrix},$$

$$\Lambda^{D^0X} = \begin{pmatrix}-\frac{1}{T_2^{D^0X}} & -\frac{3A_h}{2} - \Delta\omega & 0\\ \frac{3A_h}{2} + \Delta\omega & -\frac{1}{T_2^{D^0X}} & \gamma_P^{D^0X}\frac{B_1}{2}\\ 0 & -\gamma_P^{D^0X}\frac{B_1}{2} & -\frac{1}{T_1^{D^0X}}\end{pmatrix}, \qquad \langle\vec{\sigma}\rangle_e^{D^0X} = \frac{p_T^{D^0X}}{T_1^{D^0X}}\begin{pmatrix}0\\0\\1\end{pmatrix}, \tag{5.16}$$

$$\Lambda^{D^+} = \begin{pmatrix}-\frac{1}{T_2^{D^+}} & -\delta\omega - \Delta\omega & 0\\ \delta\omega + \Delta\omega & -\frac{1}{T_2^{D^+}} & \gamma_P\frac{B_1}{2}\\ 0 & -\gamma_P\frac{B_1}{2} & -\frac{1}{T_1^{D^+}}\end{pmatrix}, \qquad \langle\vec{\sigma}\rangle_e^{D^+} = \frac{p_T^{D^+}}{T_1^{D^+}}\begin{pmatrix}0\\0\\1\end{pmatrix}$$

are the generators and steady states under the different effective Hamiltonians. An implicit assumption in writing these equations is that the timescale over which the transitions occur is short enough to treat them as an instantaneous process. Another assumption is that the capture rates are independent of the polarization, which we have verified experimentally as shown in Fig. 5.8. For our system, the following simplifications can be made:

- $\langle\sigma_x\rangle$ and $\langle\sigma_y\rangle$ are not transferred between states: All three states have a Hamiltonian that leaves populations $\langle\sigma_z\rangle$ invariant, but not coherences $\langle\sigma_x\rangle$ and $\langle\sigma_y\rangle$. As each

individual spin hops between the three states, it will accumulate a phase depending on the time spent in each state. Since the expected lifetime of D^0 and D^+ states ($> \mu s$) is much longer than the difference in larmor precession timescales ($\sim$ 10 ns), the accumulated phase for each instance is random, and the average over the ensemble is zero. Mathematically, this requires $\{\kappa_{D^0 \to D^0X}, \kappa_{D^0 \to D^+}, \kappa_{D^+ \to D^0}\} << \frac{A_{eP}}{2}$, which is easily satisfied.

- No coherences are generated in the D^0 state: In our experiments, the saturation drive is varied over a narrow range close to ω_P, such that $\frac{A_{eP}}{2} + \Delta\omega >> \Omega$ for all Δ. Therefore, it is too far off resonance from the D^0 state to have any effect. The only pulse we apply on resonance with D^0 is the readout pulse, and there are no coherences generated in the D^0 state that play a role in the state reached at that point. Therefore, we can safely set $\langle \sigma_x \rangle^{D^0} = 0$ and $\langle \sigma_y \rangle^{D^0} = 0$ for all times.

- The only native relaxation process that matters is $T_1^{D^0}$: We showed earlier that the DNP process is phonon driven, and only occurs in the D^0 state. Therefore, $T_1^{D^0}$ is $\sim$ 100 s, varying with the laser power, and $p_T^{D^0} \simeq 1$. In the D^+ state, the nuclear spin sees a thermal T_1 and T_2, which are expected to be long (hours) [1]. In comparison, the fraction of time spent in the D^+ state must be much smaller than that spent in the D^0 state, since the D^+ state does not yield an observable signal despite a high SNR at D^0. The nuclear spin-lattice relaxation time in the D^0X state, $T_1^{D^0X}$ can be shorter than $T_1^{D^0}$ due to the presence of the hole, but is still expected to be long compared to the fraction of time spent in this state ($< 10^{-3}$). Therefore, we neglect the effect of $T_1^{D^0X}$ and $T_1^{D^+}$. Similarly, since the effective T_2 are limited by the BE rates and we dropped the coherences earlier, we do not need a native T_2 process in any of the three states.

- The lifetime of the bound exciton (D^0X) state, which has been previously measured to be 272 ns, is much shorter than the expected lifetime of the other states (D^0 and D^+), which is $> \mu$s. It is also much faster than the saturation drive strength timescale (Ω^{-1}), which is $<$ 400 Hz for experiments in this section, and at most 4 kHz for the experiment in Fig. 5.8. The average number of Auger electron driven ionizations can also be significantly more than one. This means that the D^0X state has a negligible population compared to D^+ and D^0 at any given time, and the saturation drive will not affect the spin when it passes through the this state. Mathematically, this requires $\kappa_{D^0X \to D^+} \gg \{\Omega, \kappa_{D^+ \to D^0}\}$ or $n_a \gg 1$. This essentially reduces the three step process to a two step one between D^0 and D^+.

Based on the above assumptions, we can write a simplified set of equations as:

$$\frac{d}{dt}\begin{pmatrix}\langle\sigma_x\rangle^{\mathrm{D}^+}\\ \langle\sigma_y\rangle^{\mathrm{D}^+}\\ \langle\sigma_z\rangle^{\mathrm{D}^+}\\ \langle\sigma_z\rangle^{\mathrm{D}^0}\end{pmatrix} = \begin{pmatrix}-\kappa_{\mathrm{D}^+\to\mathrm{D}^0} & -\delta\omega-\Delta\omega & 0 & 0\\ \delta\omega+\Delta\omega & -\kappa_{\mathrm{D}^+\to\mathrm{D}^0} & \Omega & 0\\ 0 & -\Omega & -\kappa_{\mathrm{D}^+\to\mathrm{D}^0} & \kappa'_{\mathrm{D}^0\to\mathrm{D}^+}\\ 0 & 0 & \kappa_{\mathrm{D}^+\to\mathrm{D}^0} & -\frac{1}{T_1^{\mathrm{D}^0}}-\kappa'_{\mathrm{D}^0\to\mathrm{D}^+}\end{pmatrix}\cdot\begin{pmatrix}\langle\sigma_x\rangle^{\mathrm{D}^+}\\ \langle\sigma_y\rangle^{\mathrm{D}^+}\\ \langle\sigma_z\rangle^{\mathrm{D}^+}\\ \langle\sigma_z\rangle^{\mathrm{D}^0}\end{pmatrix} + \frac{p_T^{\mathrm{D}^0}}{\mathrm{T}_1^{\mathrm{D}^0}}\begin{pmatrix}0\\0\\0\\1\end{pmatrix}, \tag{5.17}$$

where $\kappa'_{\mathrm{D}^0\to\mathrm{D}^+} = \kappa_{\mathrm{D}^0\to\mathrm{D}^0\mathrm{X}} + \kappa_{\mathrm{D}^0\to\mathrm{D}^+}$ and $\Omega = \gamma_P\frac{B1}{2}$ is the effective Rabi frequency in the D^+ state. Note that we are no longer able to distinguish between the BE formation/recombination and the Auger electron driven ionization, and instead measure the sum of the two rates. We will briefly discuss the potential to distinguish between the two in the outlook. Solving the above equation for the steady state solution, we find that the magnetization in the D^0 state is given by

$$\mu_z^{\mathrm{D}^0} = p_T^{\mathrm{D}^0}\left(1+\frac{\Omega^2 T_1^{\mathrm{D}^0}\kappa'_{\mathrm{D}^0\to\mathrm{D}^+}}{(\Delta\omega+\delta\omega)^2+\Omega^2+\kappa^2_{\mathrm{D}^+\to\mathrm{D}^0}}\right). \tag{5.18}$$

The general time-dependent solution to Eq. 5.17 was computed numerically and shows that under the regime of low Rabi saturation ($\Omega \le \kappa'_{\mathrm{D}^0\to\mathrm{D}^+} \ll \kappa_{\mathrm{D}^+\to\mathrm{D}^0}$), the time dependent evolution of $\langle\sigma_z\rangle^{\mathrm{D}^0}$ is very well-approximated by an exponential rise to the steady state value,

$$\langle\sigma_z\rangle^{\mathrm{D}^0}(t) \simeq \mu_z^{\mathrm{D}^0}\left(1-\exp\left(-\frac{t}{\mathrm{T}_{\mathrm{eff}}}\right)\right). \tag{5.19}$$

We can calculate the time constant $\mathrm{T}_{\mathrm{eff}}$ by noting that based on Eq. 5.17,

$$\left.\frac{d\langle\sigma_z\rangle^{\mathrm{D}^0}(t)}{dt}\right|_{t=0} = \frac{1}{\mathrm{T}_1^{\mathrm{D}^0}},$$
$$\implies \frac{\mu_z^{\mathrm{D}^0}}{\mathrm{T}_{\mathrm{eff}}} = \frac{1}{\mathrm{T}_1^{\mathrm{D}^0}}.$$

Therefore,

$$\mathrm{T}_{\mathrm{eff}} = \mathrm{T}_1^{\mathrm{D}^0} p_T^{\mathrm{D}^0}\left(1+\frac{\Omega^2 T_1^{\mathrm{D}^0}\kappa'_{\mathrm{D}^0\to\mathrm{D}^+}}{(\Delta\omega+\delta\omega)^2+\Omega^2+\kappa^2_{\mathrm{D}^+\to\mathrm{D}^0}}\right). \tag{5.20}$$

Because of the light intensity variation across the sample, we expect different parts of the sample to see different rates of ionization and recombination. However, the constants of proportionality $\alpha_{\mathrm{D}^+\to\mathrm{D}^0}$ and $\alpha_{\mathrm{D}^0\to\mathrm{D}^0\mathrm{X}}$ as well as the average number of Auger driven ionizations n_a are not expected to vary across the sample, and are expected to be only a function of the defect concentration and temperature. $T_1^{\mathrm{D}^0}$ is also independent of the local light intensity, as discussed in the previous section. Therefore, we can write

$$\langle\sigma_z\rangle^{\mathrm{D}^0}(I,t) = \mu^{\mathrm{D}^0}(I)\left(1-\exp\left(-\frac{t}{\mathrm{T}_{\mathrm{eff}}}\right)\right) \ , \tag{5.21}$$

where

$$\mu_z^{\mathrm{D}^0}(I) = p_T^{\mathrm{D}^0}\left(1+\frac{\Omega^2\mathrm{T}_1^{\mathrm{D}^0}\alpha'_{\mathrm{D}^0\to\mathrm{D}^+}\sqrt{I}}{(\Delta\omega+\delta\omega)^2+\Omega^2+\alpha^2_{\mathrm{D}^+\to\mathrm{D}^0}I}\right) \ , \tag{5.22}$$

$$\alpha'_{\mathrm{D}^0\to\mathrm{D}^+} = (1+n_a)\alpha_{\mathrm{D}^0\to\mathrm{D}^0\mathrm{X}} \ . \tag{5.23}$$

The average polarization over the sample is then

$$\overline{\langle\sigma_z\rangle}^{\mathrm{D}^0}(t) = \int p(I)\langle\sigma_z\rangle^{\mathrm{D}^0}(I,t)dI \ . \tag{5.24}$$

5.5.2 Experimental Results and Analysis

We performed a sweep of the saturation frequency at two different Rabi strengths 120 Hz and 240 Hz, with the polarization at 160 s as a function of drive frequency shown in Fig. 5.10. This is sufficient but not ideal in order to determine $\alpha_{\mathrm{D}^+\to\mathrm{D}^0}$ and $\alpha'_{\mathrm{D}^0\to\mathrm{D}^+}$, since Eq. 5.22 is only dependent on the product $\alpha'_{\mathrm{D}^0\to\mathrm{D}^+}\mathrm{T}_1^{\mathrm{D}^0}$. Instead, we determined $\mathrm{T}_1^{\mathrm{D}^0}$ from a buildup curve with no saturation, shown in Fig. 5.9. We then used the extracted value as a fixed parameter in fitting the data in Fig. 5.10 to Eq. 5.17. The fitted parameters are given in Table 5.1. We used these parameters with the simulated intensity distribution to generate predictions for the time-dependent buildup curves with saturation, shown in Fig. 5.9, as well as for the experiment shown in Fig. 5.8 in the earlier section.

Let us verify the self consistency of our measured parameters and the approximations:

- $\{\kappa_{\mathrm{D}^0\to\mathrm{D}^0\mathrm{X}}, \kappa_{\mathrm{D}^0\to\mathrm{D}^+}\} \ll \kappa_{\mathrm{D}^+\to\mathrm{D}^0}$: For the average values, the ratio of the sum ($\kappa'_{\mathrm{D}^0\to\mathrm{D}^+} = \kappa_{\mathrm{D}^0\to\mathrm{D}^0\mathrm{X}} + \kappa_{\mathrm{D}^0\to\mathrm{D}^+}$) with $\kappa_{\mathrm{D}^+\to\mathrm{D}^0}$ is 1:400, which is consistent. Similarly, the $\alpha'_{\mathrm{D}^0\to\mathrm{D}^+}$ to $\alpha_{\mathrm{D}^+\to\mathrm{D}^0}$ ratio does not exceed 1:180 for any value of I based on the simulated light intensity distribution.

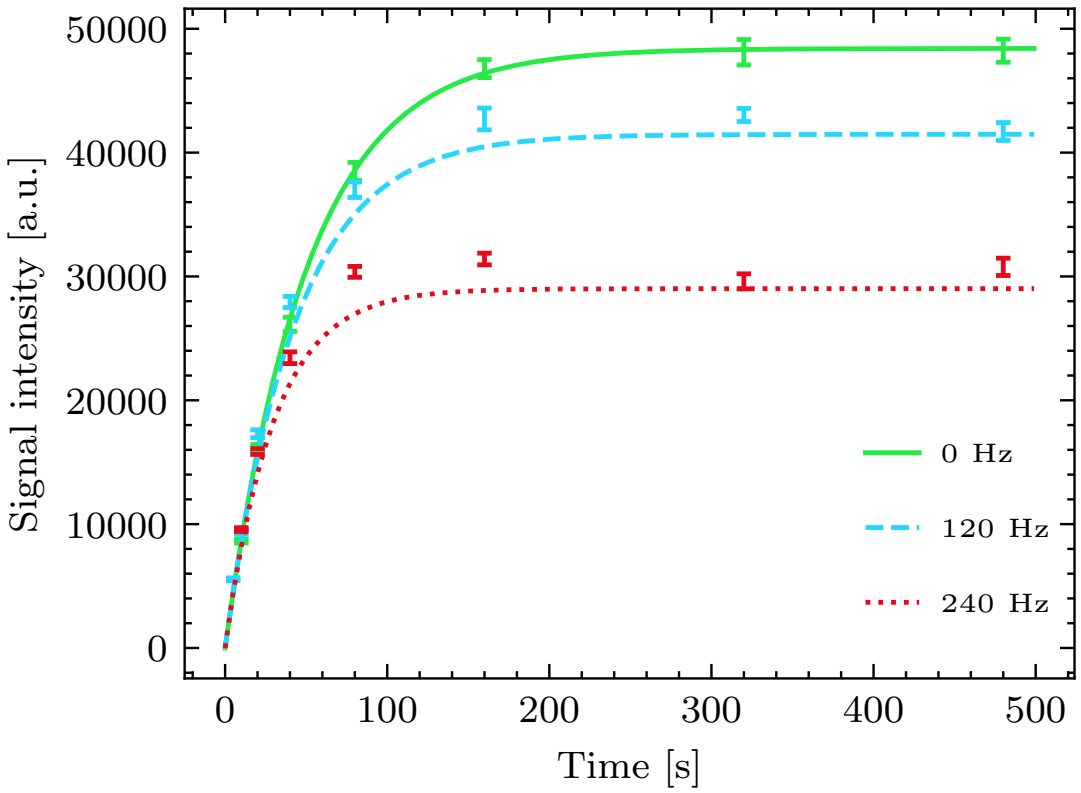

Figure 5.9: ^{31}P signal as a function of time for a saturation drive at 115.292 MHz during optical pumping, with a saturation drive strength $\Omega = 0$ Hz (green, solid), $\Omega = 120$ Hz (blue, dashed) and $\Omega = 240$ Hz (red, dotted). The solid line at 0 Hz is a fit to the data, while the dotted and dashed lines at 120 Hz and 240 Hz are model predictions, based on parameters extracted from the 0 Hz fit in combination with fits to the data in Fig. 5.10

Parameter	Value	Parameter	Value
$\alpha'_{D^0\to D^+}$	7.3 ± 0.76 Hz$\frac{cm^2}{mW}$	$\langle\kappa'_{D^0\to D^+}\rangle$	1.21 ± 0.13 kHz
$\alpha_{D^+\to D^0}$	35 ± 2 kHz$\frac{cm}{\sqrt{mW}}$	$\langle\kappa_{D^+\to D^0}\rangle$	451 ± 27 kHz
$T_1^{D^0}$	50 ± 1 s	δ	-16 ± 1.6 kHz

Table 5.1: Parameters extracted from a fit to Eq. 5.22. The mean values are calculated for the average light intensity $I = 166\ \frac{mW}{cm^2}$

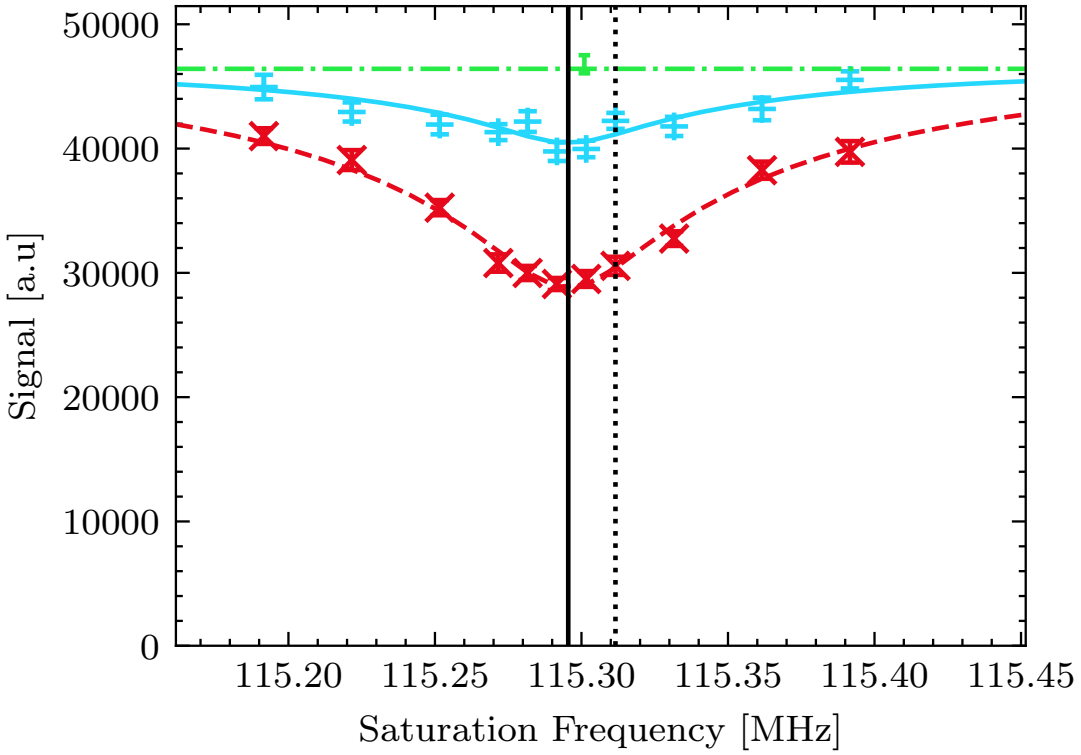

Figure 5.10: ^{31}P signal after 160 s of optical pumping, as a function of saturation frequency with fits to Eq. 5.24 for a saturation strength of 0 Hz (green, dash-dotted), 120 Hz (blue, solid) and 240 Hz (red, dashed). The time constant $T_1^{D^0}$ and the constant of proportionality between the observed signal and the steady state polarization $S \propto p_T^{D^0}$ were extracted from the fit to the time dependent buildup at 0 Hz saturation, shown in Fig. 5.9. The vertical (black, dotted) line indicates the resonance frequency of ^{31}P nuclei in the absence of a chemical/paramagnetic shift, referenced with a sodium phosphate spectrum measured in situ. The vertical (black, solid) line indicates our best estimate of the resonance frequency of ^{31}P in the D^+ state based on the fits, corresponding to a paramagnetic shift of ~ -16 kHz.

- $\kappa_{D^0X\to D^+} \gg \kappa_{D^+\to D^0}$: The previously lifetime of 272 ns [56] corresponds to $\kappa_{D^0X\to D^+} =$ 3.7 MHz, which results in the ratio 1:9 for the average intensity, and 1:2 for the maximal. This is not convincingly satisfied. However, numerical simulations of the full model in Eq. 5.15 indicate that even if the other condition ($n_a \gg 1$) is not met, the D^0X state has a negligible effect on the resultant D^0 polarization, for a wide range of A_h and $T_2^{D^0X}$ values.

- $n_a \gg 1$: Let us calculate the rate of capture of photons in the sample, based on our simulations. The COMSOL simulations indicate that the power deposited in the sample is 0.232 mW, while each photon has 1.184 eV of energy. Therefore, the photon absorption rate can be calculated as $\frac{0.232\text{ mW}}{1.184\text{ eV}}$, to be 1.223×10^{15} Hz. On the other hand, the rate of ionization can be calculated as

$$N \int \eta(I) \left(\frac{\alpha'_{D^0\to D^+} I}{\alpha_{D^+\to D^0}\sqrt{I} + \alpha'_{D^0\to D^+} I} \right) \alpha_{D^+\to D^0} \sqrt{I} dI \ ,$$

  where $N = 4.8 \times 10^{13}$ is the total no. of spins in the sample, calculated from the doping concentration and volume. This gives the rate of ionization as 5.8×10^{16} Hz. Assuming that every photon absorbed drives n_a+1 ionization events, we get $n_a \sim 46$. This is likely to be an overestimate, since each 1.184 eV photon only provides enough energy to drive at most 26 ionizations (assuming that the 45.3 meV transferred to each defect to ionize it is lost). It is not possible to pinpoint the origin of this discrepancy from our data, but we note the possible explanations : The COMSOL simulations might underestimate the true photon capture rate, or the Auger electron driven ionization process may be more efficient than our naive expectation. Other sources of error in this estimate of n_a are the uncertainties in our Rabi calibration and in the fits to the model, which may account for a $\sim$10% error, but not a factor of 2 or more. However, unless we are underestimating the photon capture rate by a factor of 50, it is reasonable to conclude that $n_a \gg 1$, such that most ionization events are driven directly by the Auger electron.

The results are consistent with our approximations. Since our measurement is based purely on the change in Hamiltonian seen by the ^{31}P spin, we must address the possibility of formation of other defect states which have zero hyperfine interaction with the electron spin, and the role that these might play in our measurements. For example, the excited orbital states of the localized defect electronic structure also have vanishing hyperfine interaction. It is possible for the electron to be driven to these states by absorption of THz phonons. However, the lifetime of the $2p_0$ state has been measured to be 235 ps [66]

in isotopically purified ^{28}Si, and the rest of the orbital states are expected to have even shorter lifetimes [67, 68]. This is much shorter than the measured lifetime of the ionized state ($\sim \mu$s), indicating that the formation of orbital states does not play a significant role in our measurements. Similarly, we can eliminate any contribution from the two-electron D^- state, which also has almost zero hyperfine interaction with the nuclear spin. The lifetime of this state has been measured to be at least two orders of magnitude longer than our measured ionized state lifetimes [69], and comparable to the lifetime of the D^0 state. However, it is still fast compared to our saturation drive Ω. Therefore, if the formation of D^- was a frequent event, it would have been reflected in the measured $\kappa_{D^+ \to D^0}$. The lack of such an effect implies that the rate of formation of the D^- state must be negligible compared to the rate of formation of the D^+ state, and that it does not play a significant role in the observed dynamics. Therefore, our attribution of the change in effective nuclear spin Hamiltonian to defect ionization events is justified.

5.6 Conclusions

We have shown that the defect ionization process driven by formation of bound excitons is independent of the ^{31}P spin state, indicating that the formation of bound excitons is driven by a process that does not involve angular momentum exchange with the ^{31}P spin. Similarly, we have also shown that the hyperpolarization process is driven by a process that is not sensitive to sub-mm scale light intensity variations. In combination, these two results lead us to conclude that the hyperpolarization process under 1047 nm optical pumping at cryogenic temperatures is predominantly driven by a phononic cross-relaxation process, where the non-equilibrium distribution of phonons can drive the electron-nuclear cross relaxation to a different, higher temperature than the electron spin temperature, generating a hyperpolarization in the opposite direction as the thermal polarization on ^{31}P.

We have also extracted the rate of defect ionization and photoneutralization, by modeling the nuclear spin dynamics under optical pumping with the Bloch-McConnell equations. Our results and analysis indicate that defect ionization is likely driven primarily by the Auger electron that is generated due to bound exciton recombination, with the rates given in Table 5.1. Our work demonstrates the utility of magnetic resonance measurements in probing defect ionization and photoneutralization rates. The applicability of this approach is not limited to samples that can be optically (or otherwise) hyperpolarized, or to ^{31}P defects in silicon. It should be usable, with modifications, in any defect with an observable nuclear spin, which is spectroscopically distinct from the bulk and has a state dependent

hyperfine coupling which is larger than the homogeneous linewidth of the nuclear spin. We have also measured a paramagnetic shift on the ionized ^{31}P nuclear spin, which has not been reported previously.

5.7 Future Directions

Fast, on demand hyperpolarization of ^{31}P spins is an important element for quantum computing proposals using the donor defects. Sub-second methods of achieving this with resonant optical excitation have been demonstrated [70]. In comparison, the above-bandgap process demonstrated here is relatively slow, with a time constant of ∼50 s, even though it is faster than previous measurements with above-bandgap light [4, 52]. However, our insight into the process driving it opens up a new avenues to achieve fast hyperpolarization. Since the process is primarily dependent on the saturation of the electron-nuclear cross-relaxation process by a resonant modulation of the hyperfine interaction, this can be achieved by applying an AC electric field, or a resonant strain modulation driven by phononic resonators. Electric field based control is of particular interest due to the local addressability and scalability of such an approach. There have been significant advances in the use of electric fields to initialize [71–73] and control [74, 75] nuclear spins in semiconductor devices. However, a sub-second hyperpolarization scheme has not been demonstrated (to the best of our knowledge).

This scheme is similar to the well known "solid effect" in magnetic resonance [60], where the electron-nuclear transition is driven by a resonant magnetic field. The solid effect is observed in the presence of small anisotropic components to the hyperfine coupling, but not in case of ^{31}P, where the interaction is symmetry constrained to be isotropic. Instead, we can use the modulation of the hyperfine interaction itself to drive the electron-nuclear transition. The Hamiltonian for the system under the application of an electric field $\vec{E}$ and strain $\vec{\varepsilon}$, Taylor expanded up to second order in both, is

$$\begin{aligned} H =& \frac{\omega_e}{2}\sigma_z^e + \frac{\omega_P}{2}\sigma_z^P + \frac{A_{eP}}{4}\Bigg(1 + \vec{\nabla}A_{eP}.\vec{\varepsilon} + \frac{1}{2}\vec{\varepsilon}.\mathbf{H}_{A_{eP}}.\vec{\varepsilon} \\ &+ \frac{1}{2}\vec{\varepsilon}.\mathbf{U}_{A_{eP}}.\vec{E} + \frac{1}{2}\vec{E}.\mathbf{V}_{A_{eP}}.\vec{E}\Bigg)\vec{\sigma}^e.\vec{\sigma}^P \ . \end{aligned} \tag{5.25}$$

The first order term in $\vec{E}$ is symmetry constrained to be zero [24], whereas the quadratic term is constrained to be isotropic ($\mathbf{V}_{A_{eP}} = \mathrm{V}_{A_{eP}}\mathbb{1}$) [36, 76], and $\mathrm{V}_{A_{eP}}$ has been measured to be -2.7×10^{-9} mm^2/V^2 [76]. Under the presence of a time-dependent strain given by

$\vec{\varepsilon}(t) = \sum_i \vec{\epsilon}_i \cos(\omega_i t + \zeta_i)$, and an oscillating electric field $\vec{E} = \vec{E}_0 \cos(\omega_E t)$, we can write the secular Hamiltonian in the rotating frame of the Zeeman term $\frac{\omega_e}{2}\sigma_z^e + \frac{\omega_P}{2}\sigma_z^P$ as

$$
\begin{aligned}
H_{\text{sec}} \simeq \frac{A_{eP}}{4}\sigma_z^e\sigma_z^P + \frac{A_{eP}}{4}\left(\sum_{\substack{\omega_i = \\ \omega_e - \omega_P}} \vec{\nabla} A_{eP} \cdot \vec{\epsilon}_i\right)\left(\sigma_+^e\sigma_-^P + \sigma_-^e\sigma_+^P\right) \\
+ \frac{A_{eP}}{8}\left(\sum_{\substack{\omega_i \pm \omega_k = \\ \omega_e - \omega_P}} \vec{\epsilon}_i \cdot \mathbf{H}_{A_{eP}} \cdot \vec{\epsilon}_k\right)\left(\sigma_+^e\sigma_-^P + \sigma_-^e\sigma_+^P\right) \\
+ \frac{A_{eP}}{8}\left(\sum_{\substack{\omega_i \pm \omega_E = \\ \omega_e - \omega_P}} \vec{\epsilon}_i \cdot \mathbf{U}_{A_{eP}} \cdot \vec{E}_0\right)\left(\sigma_+^e\sigma_-^P + \sigma_-^e\sigma_+^P\right) \\
+ \frac{A_{eP}}{8}\left(\delta_{2\omega_E - (\omega_e - \omega_P)} \mathrm{V}_{A_{eP}} \vec{E}_0 \cdot \vec{E}_0\right)\left(\sigma_+^e\sigma_-^P + \sigma_-^e\sigma_+^P\right) \ .
\end{aligned}
\tag{5.26}
$$

Therefore, if we apply an AC electric field at $\omega_E = \frac{\omega_e - \omega_P}{2}$, we can drive the electron-nuclear cross relaxation via the $\mathrm{V}_{A_{eP}}$ term. The amplitude of the cross-relaxation drive is -19.8×10^{-3} Hz mm^2/V^2, suggesting that sub-second polarization should be possible at modest electric field amplitudes of 10 V/mm or higher. There are a few considerations to keep in mind for such an approach: The nuclear spin polarization achieved in this scheme is limited by the electron spin polarization. This can be achieved by keeping B_0 high or the temperature low. The frequency ω_E at which the electric field must be applied increases with high fields (∼94 GHz at our field of 6.7 T), which poses an engineering challenge. This can be avoided by going to dilution refrigerator temperatures, where the electron is almost fully polarized at a moderate field of 3500 G, which is commonly used for X-band ESR measurements and would require $\omega_E \sim 5$ GHz. On the other hand, the electron T_1^e must also remain short. This is not the case at X-band, since the T_1^e scales as B^{-5} under the direct process [77]. This may be circumvented by reducing the electron T_1^e on demand using a burst of above-bandgap optical excitation, which needs to be short/weak enough to avoid raising the temperature of the sample appreciably.

It may also be possible to perform frequency selective phonon detection [36] using the ^{31}P hyperpolarization process outlined above. The electric field-strain coupling $\mathbf{U}_{A_{eP}}$ is known to cause inhomogeneous broadening due to the random distribution of static strains in the sample [24, 76], and is usually treated as a nuisance. However, the application of a sufficiently large AC electric field at $\omega_E \neq \frac{\omega_e - \omega_P}{2}$ will drive a hyperpolarization whose timescale is dominated by the amplitude and orientation of the phonon modes at a frequency $\omega_e - \omega_P \pm \omega_E$. This may enable mapping of the relative occupation of various

phonon modes.

Another interesting extension of our work would be to use the frequency swept saturation drive to detect the hyperfine coupling to the hole (A_h), which has not been measured experimentally yet. This would require a much wider sweep than the 300 kHz one performed in Fig. 5.10, and would also allow us to extract n_a if the effect of the hyperfine interaction is observable. Fig. 5.11 shows the simulated frequency dependent curve, using the extracted rates and the full model (Eq. 5.15). It is clear that the ability of this measurement to observe the effect of the hole will be conditional on the relative values of A_h and n_a - the smaller the n_a, the larger the saturation drive strength necessary to create an observable contrast at the hole frequency. However, the larger the saturation drive, the broader is the central line at the D^+ frequency, increasing the value of the smallest observable A_h. The simulations indicate that as long as the hole hyperfine interaction is close to or greater than the value of 2 MHz suggested in literature [58], it should be possible to observe this effect. Unfortunately, a broad frequency sweep with a calibrated Ω was not practical with our probe circuit, since the narrow bandwidth would require retuning of the probe at every few 100 kHz variation of the saturation drive frequency. This would in turn require calibration of the probe matching for the D^0 channel as well as a calibration of the Ω for each point. The complications associated with frequent retuning of the probe can be circumvented by varying the value of the static field for the lasing period, while saturating at a fixed frequency and detecting at a fixed field. This was also non-trivial for our current setup, where the static field is provided by a persistent mode NMR magnet.

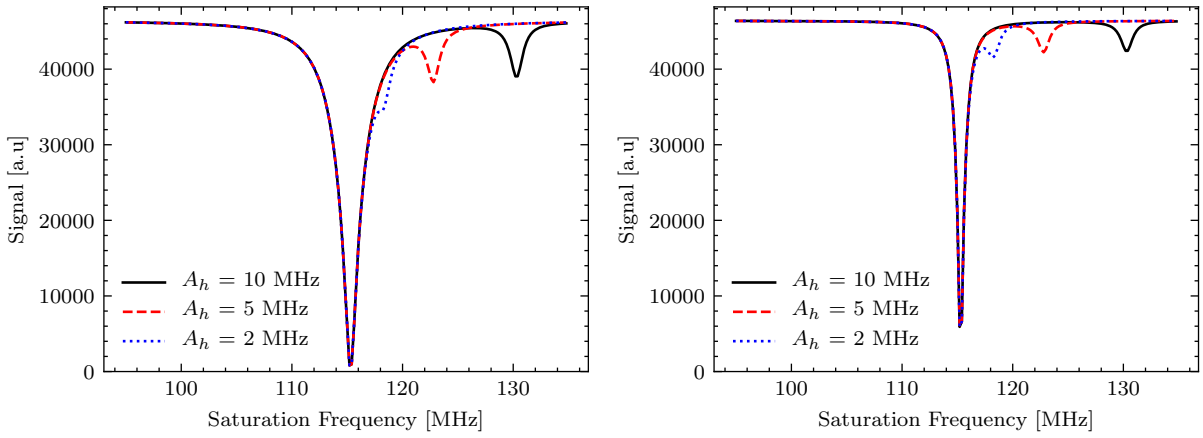

(a) $n_a = 25$, $\Omega = 6$ kHz

(b) $n_a = 5$, $\Omega = 2$ kHz

Figure 5.11: Simulation of the wide frequency sweep for various hole hyperfine interaction strengths, given different values of the Auger electron driven ionization number n_a and saturation drive strength Ω. This indicates that a pump-probe type experiment with stronger Rabi and a wider frequency sweep will be able to resolve the hole hyperfine interaction if it is close to or larger than the 2 MHz value expected from theoretical estimates.

Chapter 6

Dynamic Nuclear Polarization in Natural Abundance Silicon

6.1 Introduction

The research into ^{31}P defects for quantum information and sensing applications has been focused on using isotopically pure ^{28}Si crystals, since ^{29}Si nuclear spins are a major source of decoherence for the defect. However, ^{29}Si spins also have some desirable properties, such as long coherence [21] and spin-lattice relaxation times [5, 78]. Therefore, these spins can serve as a useful testbed for many-body physics ideas [79, 80] and have been explored as a potential hyperpolarized Magnetic Resonance Imaging (MRI) contrast agent [81, 82]. They have also been suggested as candidates for Quantum Computing [5, 21] and Quantum Memory [83] applications in the past, although interest in this has since reduced, with defect spins and quantum dot based approaches yielding much more promising results. For all of these applications, fast hyperpolarization of the spins presents a challenge that has not been convincingly overcome. Such hyperpolarization of nearby ^{29}Si spins may also be used as a passive means of improving defect coherence times [84].

It has been shown that bulk ^{29}Si can be hyperpolarized using optical pumping with above-bandgap [5, 85] as well as below-gap and resonant lasers [78]. Above-bandgap optical pumping, in particular, can drive the ^{29}Si polarization using out-of-equilibrium electron spins [57] and ^{31}P nuclear spins [78] as a resource. In this chapter, we investigate the mechanism driving these processes in more detail, and propose a scheme to hyperpolarize the ^{29}Si efficiently.

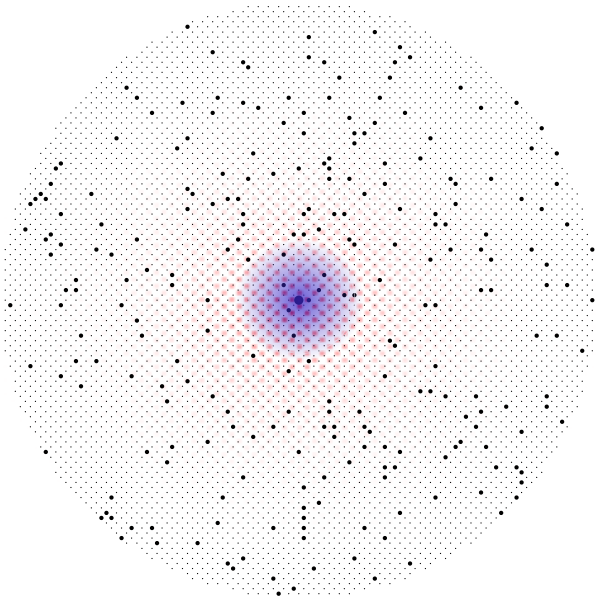

Figure 6.1: An illustration of the defect electron, ^{31}P and nearby ^{29}Si in silicon. The small dots represent lattice sites, with the larger interspersed ones being ^{29}Si, picked uniformly at random with probability $p = 0.047$. The largest dot at the center is the ^{31}P nuclear spin. The purple, symmetric cloud around it illustrates the decay of the dipolar interaction $\{\mathbf{D}^{Pj}, \mathbf{D}^{ej}\}$ in the plane perpendicular to the applied magnetic field. The red, periodic cloud illustrates the defect electron probability density, which is proportional to $\{A_{ej}\}$. The wavefunction oscillates with the periodicity of the lattice, but has an envelope that decays slower than the dipolar interaction.

6.2 Theory

As described in Ch.2, we treat the bulk phosphorus-doped silicon as an ensemble of subsystems, each consisting of the defect electron spin, the ^{31}P nuclear spin and the set $\{^{29}\text{Si}\}$ of the ^{29}Si nuclear spins within a distance that is half the average separation between defects. For the natural abundance silicon sample, this distance is 15.22 nm (See Table 3.1). Fig. 6.1 illustrates this subsystem in natural abundance silicon (4.7% ^{29}Si). The total Hamiltonian for this system, from Eq. 3.1, is

$$H = \frac{\omega_e}{2}\sigma_z^e + \frac{\omega_P}{2}\sigma_z^P + \frac{\omega_{Si}}{2}\sum_{j\in\{^{29}\text{Si}\}}\sigma_z^j + \frac{A_{eP}}{4}\vec{\sigma}^e\cdot\vec{\sigma}^P$$
$$+ \frac{1}{4}\sum_{j\in\{^{29}\text{Si}\}}\vec{\sigma}^e\cdot\mathbf{A}^{ej}\cdot\vec{\sigma}^j + \frac{1}{4}\sum_{j\in\{^{29}\text{Si}\}}\vec{\sigma}^P\cdot\mathbf{D}^{Pj}\cdot\vec{\sigma}^j + \frac{1}{4}\sum_{\{i,j\}\in\{^{29}\text{Si}\}}\vec{\sigma}^i\cdot\mathbf{D}^{ij}\cdot\vec{\sigma}^j \ ,$$

where $\{\mathbf{A}^{ej}\}$ are the hyperfine interaction tensors between the electron and the ^{29}Si. $\{\mathbf{D}^{Pj}\}$ and $\{\mathbf{D}^{ij}\}$ are the dipolar interaction tensors corresponding to the ^{31}P-^{29}Si and ^{29}Si-^{29}Si dipolar interactions respectively.

In this section, we analyze the effect of the various terms in this Hamiltonian. We show that the $\{\mathbf{A}^{ej}\}$ term can drive a polarization on the core ^{29}Si nuclear spins under optical pumping, similar to the ^{31}P model introduced in Ch. 5. We also show that the $\{\mathbf{D}^{Pj}\}$ term can drive a process where polarization from the ^{31}P is transferred to the core ^{29}Si at two matching conditions, at 2.3 T where it adds to the phononic contribution, and at 6.7 T, where it competes against the phononic process. Fig. 6.1 illustrates that while $\mathbf{A}^{ej}$ and $\mathbf{D}^{Pj}$ are both functions of the relative position vector $\vec{r}$ between the defect and the j^{th} ^{29}Si spin, they are not monotonically related. As a result, the two processes may primarily address different subsets of the core ^{29}Si. The resulting polarization of the core is transferred to the bulk ^{29}Si by the $\{\mathbf{D}^{ij}\}$ term, through the process of spin diffusion. We show that the defect ionization and recombination cycle driven during optical pumping has an effect on the spin diffusion processes driven by both the $\{\mathbf{D}^{ij}\}$ and $\{\mathbf{D}^{Pj}\}$ terms.

6.2.1 The Phononic Model for Nearby ^{29}Si

Let us consider the effect of the hyperfine interaction term $\{\mathbf{A}^{ej}\}$. For now, we neglect the dipolar component $\{\mathbf{D}_{ej}\}$ and focus on the isotropic Fermi-contact component $\{A_{ej}\}$. Following the derivation of Eq. 5.9, the secular Hamiltonian under the time-dependent

strain induced by optical pumping is

$$
\begin{aligned}
H_{\text{sec}} \simeq & \frac{A_{eP}}{4}\sigma_z^e\sigma_z^P + \sum_j \frac{A_{ej}}{4}\sigma_z^e\sigma_z^j \\
& + \sqrt{I}\sum_j \frac{A_{ej}}{4}\left(\sum_{\substack{\omega_i= \\ \omega_e-\omega_{Si}}} \vec{\nabla}A_{ej}\cdot\vec{\epsilon}_i\right)\left(\sigma_+^e\sigma_-^j + \sigma_-^e\sigma_+^j\right) \\
& + \sqrt{I}\frac{A_{eP}}{4}\left(\sum_{\substack{\omega_i= \\ \omega_e-\omega_P}} \vec{\nabla}A_{eP}\cdot\vec{\epsilon}_i\right)\left(\sigma_+^e\sigma_-^j + \sigma_-^e\sigma_+^j\right) \\
& + I\sum_j \frac{A_{ej}}{8}\left(\sum_{\substack{\omega_i\pm\omega_k= \\ \omega_e-\omega_{Si}}} \vec{\epsilon}_i\cdot\mathbf{H}_{A_{ej}}\cdot\vec{\epsilon}_k\right)\left(\sigma_+^e\sigma_-^j + \sigma_-^e\sigma_+^j\right) \\
& + I\frac{A_{eP}}{8}\left(\sum_{\substack{\omega_i\pm\omega_k= \\ \omega_e-\omega_P}} \vec{\epsilon}_i\cdot\mathbf{H}_{A_{eP}}\cdot\vec{\epsilon}_k\right)\left(\sigma_+^e\sigma_-^P + \sigma_-^e\sigma_+^P\right) \ .
\end{aligned}
\tag{6.1}
$$

The effective Hamiltonian indicates that cross relaxation of the ^{29}Si will be driven by either single phonon absorption ($\omega_i = \omega_e - \omega_{Si}$), two phonon absorption ($\omega_i + \omega_k = \omega_e - \omega_{Si}$) or Raman scattering ($\omega_i - \omega_k = \omega_e - \omega_{Si}$) processes. Since the difference in matching conditions ($\omega_i \pm \omega_k = \omega_e - \omega_n$) for ^{31}P and ^{29}Si is very small compared to the matching condition frequency itself (for e.g. 187.651 GHz vs 187.822 GHz at 6.7 T), we expect that the two phonon/Raman driven electron-^{29}Si cross-relaxation leads to a similar effective temperature, hyperpolarizing these ^{29}Si spins to a negative polarization.

The dipolar component $\{\mathbf{D}^{ej}\}$, which we neglected in Eq. 6.1, has terms that can drive all the transitions. Let us consider the dipolar alphabet notation for the interaction, as shown in Eq. 1.18. When the interaction is modulated at ω_e, it can drive the electron spin relaxation via the C and D terms. When modulated at $\omega_e - \omega_n$, it can drive the zero quantum cross-relaxation via the B term, and when modulated at $\omega_e + \omega_n$, it can drive the double quantum cross relaxation via the E and F terms. It can also drive the nuclear spin relaxation directly via the C and D terms, when modulated at ω_n. However, we noted in Ch. 2 that the dipolar interaction decays much faster as a function of distance from the defect (r) than the envelope $F_j(r)$ of the wavefunction. As a result, the interaction is expected to be primarily Fermi-contact type for ^{29}Si further away from the defect site. Even for the nearby defect sites, ENDOR measurements [39, 41] indicate that the hyperfine interaction tensor is primarily isotropic (for e.g., the dipole-dipole interaction with a ^{29}Si at

the neighboring lattice site would be ~ 300 kHz, while the largest Fermi-contact hyperfine coupling is 3.1 MHz). While there may be a small number of nearby ^{29}Si that experience a dipolar interaction comparable to or stronger than the Fermi-contact interaction, it is apparent that the majority do not. Therefore, we expect that on average, the effect of the dipolar interaction will be small compared to that of the Fermi-contact term.

It is important to note that unlike the ^{31}P, there are no symmetry constraints limiting the linear term (∇A_{ej}) in Eq. 6.1. The cross-relaxation may be driven by the single phonon, two phonon or Raman processes. The contribution of each of these processes can differ depending on the location of the ^{29}Si under consideration relative to the defect. However, we still expect the quasi-temperature T_p of the cross-relaxation to be different from the electron spin temperature T_e, due to the contribution of the defect ionization process to the electron spin relaxation. As a result, the nearby ^{29}Si spins will be driven to a non-thermal equilibrium polarization $p_n = \frac{p_e - p_x}{1 - p_e p_x}$, with a timescale $\frac{2\mathrm{T}_x}{(1-p_e p_x)}$, as derived in Eq. 5.11 and Eq. 5.14. The T_x and T_p are expected to be a non-trivial function of the phonon spectrum as well as the defect electron wavefunction, and we make no attempt to quantify them.

The relaxation timescale T_x for any ^{29}Si spin is expected to be significantly longer than that of the ^{31}P, since it is inversely proportional to the hyperfine interaction A_{ej}. Given that this is at least 40 times smaller than A_{eP} even for the ^{29}Si spin with the largest hyperfine shift, we expect the resultant hyperpolarization timescale is > 2000 s under optical pumping, given the ~ 50 s timescale observed for ^{31}P in the ^{28}Si enriched sample. However, since there is a large number of ^{29}Si spins experiencing the cross-relaxation with the electron spin, the total angular momentum transferred from the electron to the ^{29}Si can be significant.

6.2.2 Spin Diffusion and the Diffusion Barrier

The $\{\mathbf{D}^{ij}\}$ term of the Hamiltonian, which is the dipole-dipole interaction between ^{29}Si, is limited to ≤ 400 Hz due to the lattice spacing. This is a perturbation to the Zeeman interaction term $\omega_{Si} \sim 10 - 100$ MHz for typical NMR fields. In the rotating frame of the ^{29}Si Zeeman interaction, after performing the rotating wave approximation, the dipolar interaction term is

$$\sum_{j \in \{^{29}\mathrm{Si}\}} \vec{\sigma}^i \cdot \mathbf{D}^{ij} \cdot \vec{\sigma}^j \simeq \sum_{j \in \{^{29}\mathrm{Si}\}} \frac{1}{4} \left(D^{ij}_{xx} + D^{ij}_{yy} \right) \left(\sigma^i_+ \sigma^j_- + \sigma^i_- \sigma^j_+ \right) + D^{ij}_{zz} \sigma^i_z \sigma^j_z \, . \tag{6.2}$$

If we consider a two spin subset (labelled 1 and 2) and a difference in polarization i.e. initial states

$$\rho_1 = \frac{1}{2}\mathbb{1} + \frac{p_1}{2}\sigma_z^1 \ , \qquad\qquad \rho_2 = \frac{1}{2}\mathbb{1} + \frac{p_2}{2}\sigma_z^2 \ ,$$

the evolution under the dipolar interaction $\mathbf{D}^{12}$ results in

$$\langle\sigma_z^1\rangle(t) = \frac{p_1+p_2}{2} + \frac{p_1-p_2}{2}\cos\left(\omega_{12}t\right) \ , \qquad \langle\sigma_z^2\rangle(t) = \frac{p_1+p_2}{2} - \frac{p_1-p_2}{2}\cos\left(\omega_{12}t\right) \ ,$$

with $\omega_{12} = D_{xx}^{12} + D_{yy}^{12}$. Therefore, the dipolar interaction drives a coherent exchange of polarization back and forth. In our case, there are a large number of spins $\{i, j\}$ interacting with each other through the dipolar interaction. In the presence of relaxation effects (T_2), this results in an equalisation of the polarization over time. It has been shown [86] that this process can be approximated by a classical diffusion equation, given by

$$\frac{d\langle\sigma_z\rangle(\vec{r},t)}{dt} = -D\nabla^2\langle\sigma_z\rangle(\vec{r},t) \ , \tag{6.3}$$

where D is the spin diffusion coefficient. The coefficient can be estimated [86] from the dipole induced spin-spin relaxation time (T_2) as $D \simeq \frac{a^2}{34T_2}$ for a simple cubic lattice and $D \simeq \frac{a^2}{53T_2}$ for a face-centered cubic (FCC) lattice, where a is the distance between neighbouring nuclei. This has been demonstrated to be in good agreement with indirect [87, 88] as well as direct [89] experimental measurements of the diffusion coefficient in various systems. The average nearest neighbour distance between the ^{29}Si spins in natural abundance silicon is 0.433 nm (See Appendix A/Table 3.1), corresponding to a dipolar interaction of 58.486 Hz. The dipolar linewidth has been measured experimentally to be $\sim$ 80 Hz [90]. This results in a spin diffusion coefficient in bulk silicon of 0.5 nm^2/s [1]. We note that this is a crude estimate, since the expression $D \simeq \frac{a^2}{30T_2}$ commonly used in literature [86, 91, 92] is derived based on the assumption of a simple cubic lattice of equally spaced nuclear spins averaged over all orientations, which is likely to be a poor approximation to the ^{29}Si in silicon, where we have poisson distributed nuclear spins in a single crystal with a diamond cubic structure.

The polarization from the core ^{29}Si of each defect needs to diffuse $\langle r\rangle \leq 15.22$ nm on average before it spans the entire bulk. Using the bulk ^{29}Si spin diffusion coefficient $D = 0.5$ nm^2/s, this requires a timescale ($\tau = \frac{\langle r^2\rangle}{6D}$ [93]) of 77 s. This is short compared to the lower bound of 2000 s on the expected T_{DNP} of the core, calculated above based on

[1] This value differs from that of Hayashi et al [91, 92], since they consider the average distance to be $a \simeq N_c^{-\frac{1}{3}}$, which is incorrect by a factor of ~ 0.554.

the phononic model. However, the true timescale for spin diffusion can be longer due to the presence of the so-called spin diffusion barrier, which we look at next.

The idea of a spin diffusion barrier was proposed by Bloembergen [94] and observed in multiple experiments [95–98]. A detailed theoretical analysis of the expected role of this barrier in nuclear spin relaxation via impurities as well as DNP originating from impurities using a radial diffusion equation model was done by Khutsishvili [86]. The barrier is formed because of the fact that the B term of the dipolar alphabet, which is responsible for driving the homonuclear spin diffusion, is not secular when the spins do not have the same precession frequency. The distribution of hyperfine interactions $\{\mathbf{A}^{ej}\}$ means that the core spins have a varying range of precession frequencies, different from each other and from the bulk. This detuning reduces the efficiency of spin diffusion driven by the dipolar interaction. This results in the "spin diffusion barrier", which stops/slows the spread of polarization between nuclei where $|\mathbf{A}^{ei} - \mathbf{A}^{ej}| > |\mathbf{D}^{ij}|$.

Optical pumping in silicon introduces a new pathway in this process. We saw in Ch. 5 that the optical pumping drives a defect ionization and recombination process, with the rates given by Table. 5.1. During the ionized stage (D^+), the electron-nuclear hyperfine interaction vanishes ($\mathbf{A}^{ej} = 0$), temporarily removing the barrier and allowing diffusion between all ^{29}Si spins. We treat this as a classical diffusion problem with a time dependent (fluctuating) diffusion coefficient, such that

$$\mathcal{D}(t) = \begin{cases} D_{CB} & \text{if } D^0 \\ D & \text{if } D^+ \end{cases} , \tag{6.4}$$

where D_{CB} is the spatially averaged diffusion rate across the barrier. Since the diffusion coefficient $\mathcal{D}$ is purely a function of time, the diffusion equation is given by [93]

$$\frac{d\langle\sigma_z\rangle(\vec{r},t)}{dt} = -\mathcal{D}_{\text{eff}}\,\nabla^2\langle\sigma_z\rangle(\vec{r},t) , \qquad \mathcal{D}_{\text{eff}} = \frac{1}{t}\int_0^t \mathcal{D}(\tau)d\tau , \tag{6.5}$$

where $\langle\sigma_z\rangle(\vec{r},t)$ is the spatial and temporal polarization distribution and $\mathcal{D}_{\text{eff}}$ is the average diffusion coefficient over a time period t. Our measurements in Ch. 5 indicate that the timescales for defect ionization and photoneutralization are milliseconds or shorter. In comparison, the timescales we are observing over are hundreds of seconds. Therefore, the rapidly fluctuating $\mathcal{D}(\tau)$ yields an average $\mathcal{D}_{\text{eff}}$ given by

$$\mathcal{D}_{\text{eff}} = \frac{\kappa_{D^+\to D^0} D_{CB} + \kappa'_{D^0\to D^+} D}{\kappa'_{D^0\to D^+} + \kappa_{D^+\to D^0}} , \tag{6.6}$$

where $\kappa'_{D^0\to D^+}$ and $\kappa_{D^+\to D^0}$ are expected to be similar to the average values measured in Table. 5.1. Since $\kappa'_{D^0\to D^+} \propto I$, $\kappa_{D^+\to D^0} \propto \sqrt{I}$ and $\kappa'_{D^0\to D^+} \ll \kappa_{D^+\to D^0}$ for all practical laser powers, we expect that the D_{CB} contribution is independent of laser power, while the D contribution scales as $\sqrt{I}$.

Let us consider the extreme case where no diffusion can occur in the D^0 state when the diffusion barrier is present i.e. $D_{CB} = 0$. This assumption has been proven to be false in other systems [99], but is useful for calculating a lower bound on $\mathcal{D}_{\text{eff}}$. The average values in Table 5.1 give $\mathcal{D}_{\text{eff}} = 1.33 \times 10^{-3}$ nm^2/s. Estimating a "barrier size" is also non-trivial, since the oscillatory nature of the electron wavefunction leaves hyperfine-shifted core spins interspersed with bulk spins. Assuming a diffusion barrier size (r) of 2.7 nm based on the distance it takes for the dipolar component of the hyperfine interaction to fall within linewidth (and a generous overestimate compared to most experimentally measured diffusion barrier radii in other systems [99]), the time constant is 913 s for the polarization to cross the diffusion barrier. Since spin diffusion is not, in fact, fully suppressed in the D^0 state, the true timescale should lie somewhere between 77 s and 913 s. The longest time constant of 913 s is still shorter than the > 2000 s timescale for the core polarization based on the phononic process. Therefore, we conclude that the diffusion barrier is not expected to be a rate limiting step for polarizing the bulk via the phononic process.

We note that the actual process is not classical diffusion, but a quantum mechanical dipolar interaction, which may be further enhanced by the defect ionization and photoneutralization cycle in the regime $\kappa_{D^+\to D^0} \sim \{|\mathbf{D}^{ij}|\}$) and eventually suppressed by a quantum Zeno effect [100] in the limit of extremely short lifetimes ($\kappa_{D^+\to D^0} \gg \{|\mathbf{D}^{ij}|\}$). It can also be eliminated using multipulse methods such as WAHUHA [101]. Simultaneously, the reduced lifetimes may also increase diffusion in the D^0 state when $\kappa'_{D^0\to D^+} \sim \{|\mathbf{A}^{ei} - \mathbf{A}^{ej}|\}$, until it is also eventually suppressed in the regime $\kappa'_{D^0\to D^+} \gg \{|\mathbf{A}^{ei} - \mathbf{A}^{ej}|\}$. Therefore, the true polarization transfer rate will be determined by not only the fraction of time spent in the D^0 and D^+ states, but also the relative magnitude of the lifetimes of the states compared to the timescales of the dipole-dipole and hyperfine interactions.

6.2.3 ^{31}P-^{29}Si Resonant Matching

The ^{31}P nuclear spins, which are highly polarized due to the phononic process, can also be used as a resource, transferring polarization to their neighboring ^{29}Si spins via the dipole-dipole interaction $\{\mathbf{D}^{Pj}\}$. However, these two spins have very different Larmor precession

frequencies at most magnetic fields, since their gyromagnetic ratios are different. As a result, the B term of the dipole-dipole interaction is suppressed. Dluhy et al [78] showed experimentally that at 2.3 T, there exists a resonant matching condition where the dipole interaction is allowed, and results in polarization transfer from ^{31}P to bulk ^{29}Si. Here, we demonstrate that there are two matching conditions, with the second one at 6.7 T [7].

Let us consider the effect of the $\{\mathbf{D}^{Pj}\}$ term, ignoring the $\{\mathbf{D}^{ij}\}$ term for now. In the rotating frame of the electron spin, the secular Hamiltonian is given by

$$\begin{aligned} H = &\frac{\omega_P}{2}\sigma_z^P + \frac{\omega_{Si}}{2}\sum_j \sigma_z^j + \frac{A_{eP}}{4}\sigma_z^e\sigma_z^P \\ &+ \frac{1}{4}\sum_j \left(A_{zx}^{ej}\sigma_z^e\sigma_x^j + A_{zy}^{ej}\sigma_z^e\sigma_y^j + A_{zz}^{ej}\sigma_z^e\sigma_z^j\right) + \frac{1}{4}\sum_j \vec{\sigma}^P \cdot \mathbf{D}^{Pj} \cdot \vec{\sigma}^j \ . \end{aligned} \tag{6.7}$$

In order to visualize the effect of the $\{\mathbf{D}^{Pj}\}$ term, we consider a single ^{29}Si spin (with $\mathbf{A}^{ej} = 0$ for simplicity), and plot the eigenstructure and nuclear spin transition frequencies of the three spin (electron, ^{31}P and ^{29}Si) system as a function of field in Fig. 6.2. The eigenstructure shows that the dipolar term opens up avoided crossings in the $|\uparrow_e\rangle$ manifold of the electron spin, between the $|\uparrow_P\downarrow_{Si}\rangle$ and $|\downarrow_P\uparrow_{Si}\rangle$ states at 2.3 T (where $\nu_{Si} = \nu_P^{\uparrow}$) and between the $|\uparrow_P\uparrow_{Si}\rangle$ and $|\downarrow_P\downarrow_{Si}\rangle$ states at 6.7 T (where $\nu_{Si} = -\nu_P^{\uparrow}$), but results in only an energy shift in the $|\downarrow_e\rangle$ manifold.

We can simplify the Hamiltonian in Eq. 6.7 by going into one of two interaction frames, depending on whether we are close to 2.3 T (+) or 6.7 T (−), given by the Hamiltonians

$$H_{0,\pm} = H_0^{\downarrow_e} |\downarrow_e\rangle \langle\downarrow_e| + H_{0,\pm}^{\uparrow_e} |\uparrow_e\rangle \langle\uparrow_e| \ , \tag{6.8}$$

where

$$H_{0,\pm}^{\uparrow_e} = \frac{\omega_P^{\uparrow}}{2}\left(\sigma_z^P \pm \sum_j \sigma_z^j\right) \ , \tag{6.9}$$

$$H_0^{\downarrow_e} = \frac{\omega_P^{\downarrow}}{2}\sigma_z^P + \frac{\omega_{Si}}{2}\sum_j \sigma_z^j \ , \tag{6.10}$$

and $\omega_P^{\uparrow\downarrow} = \omega_P \mp \frac{A_{eP}}{2}$. Since $\{\omega_P^{\uparrow\downarrow}, \omega_{Si}\} \gg \{|\mathbf{D}^{Pj}|, |\mathbf{A}^{ej}|\}$, we can write the effective Hamiltonians as

$$H_{\pm} \simeq H^{\downarrow_e} |\downarrow_e\rangle \langle\downarrow_e| + H_{\pm}^{\uparrow_e} |\uparrow_e\rangle \langle\uparrow_e| \ , \tag{6.11}$$

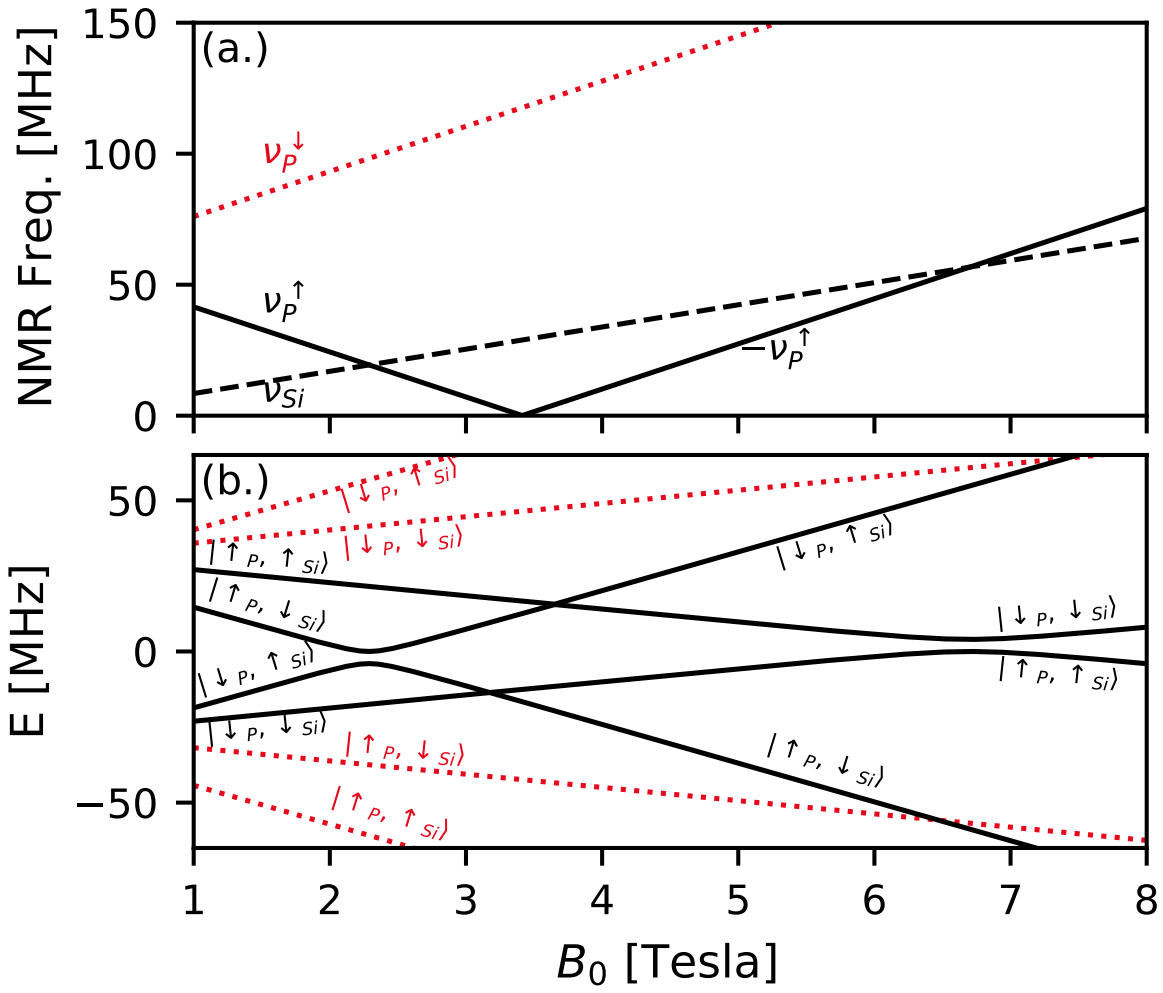

Figure 6.2: (a.) NMR transition frequencies vs. external magnetic field under the Zeeman and electron-^{31}P hyperfine interactions, for ^{31}P in the $|\downarrow_e\rangle$ (red, dotted) and $|\uparrow_e\rangle$ (black, solid) manifolds, and for ^{29}Si (black, dashed). (b.) Energy levels vs. external magnetic field of an electron-^{31}P-^{29}Si model spin system. The Hamiltonian is given by Eq. 6.7, with the anticrossing exaggerated by the choice of a dipolar interaction of 2 MHz. The corresponding ^{31}P and ^{29}Si eigenstates far from the 2.3 T and 6.7 T energy level anticrossings are marked in the figure, with the electron in the $|\uparrow_e\rangle$ / $|\downarrow_e\rangle$ indicated by black and red color, respectively. The anticrossing between $|\uparrow_P, \downarrow_{Si}\rangle$ and $|\downarrow_P, \uparrow_{Si}\rangle$ at 2.3 T results in a zero-quantum (ZQ) polarization exchange, while the anticrossing between $|\downarrow_P, \downarrow_{Si}\rangle$ and $|\uparrow_P, \uparrow_{Si}\rangle$ at 6.7 T results in a double-quantum (DQ) polarization exchange. The effective interaction Hamiltonians for the ZQ (+) and DQ (−) are calculated in Eq. 6.14

where

$$H_{\pm}^{\uparrow_e} = \sum_j \left(\frac{\Delta_j^{\pm}}{2}\sigma_z^j + \frac{D_{zz}^{Pj}}{4}\sigma_z^P\sigma_z^j + H_{\pm,D}^{Pj} \right) , \tag{6.12}$$

$$H^{\downarrow_e} = \sum_j \left(-\frac{A_{eP}}{2}\sigma_z^P - \frac{A_{zz}^{ej}}{4}\sigma_z^j + \frac{D_{zz}^{Pj}}{4}\sigma_z^P\sigma_z^j \right) , \tag{6.13}$$

with $\Delta_j^{\pm} = \omega_P^{\downarrow} \mp \left(\omega_{Si} + \frac{A_{zz}^{ej}}{2}\right)$, and

$$\begin{aligned} H_{+,D}^{Pj} &= \frac{1}{4}\left(D_{xx}^{Pj} + D_{yy}^{Pj}\right)\left(\sigma_+^P\sigma_-^j + \sigma_-^P\sigma_+^j\right) , \\ H_{-,D}^{Pj} &= \frac{1}{4}\left(D_{xx}^{Pj} - D_{yy}^{Pj} - 2iD_{xy}^{Pj}\right)\sigma_+^P\sigma_+^j + \frac{1}{4}\left(D_{xx}^{Pj} - D_{yy}^{Pj} + 2iD_{xy}^{Pj}\right)\sigma_-^P\sigma_-^j . \end{aligned} \tag{6.14}$$

Close to the 2.3 T matching condition, $\Delta_j^+ \ll |H_{+,D}^{Pj}|$ for some subset of ^{29}Si spins, allowing $H_{+,D}^{Pj}$ to drive spin exchange, whereas close to 6.7 T, $\Delta_j^- \ll |H_{-,D}^{Pj}|$ for some subset of ^{29}Si spins, allowing $H_{-,D}^{Pj}$ to drive the spin exchange. Experimental measurements at 2.3 T [78] indicate that the width of the matching condition in terms of its effect on the bulk polarization is much broader than that of possible $\{\mathbf{D}^{Pj}\}$, and is determined by the distribution of $\{\mathbf{A}^{ej}\}$ instead. At 6.7 T, we expect the width to be determined by a combination of the $\{\mathbf{A}^{ej}\}$ distribution and the lifetime of the electron excited state $|\uparrow_e\rangle$. Away from these two conditions, $\Delta_j^{\pm} \gg |H_{\pm,D}^{Pj}|$ and $H_{\pm,D}^{Pj}$ is suppressed for all ^{29}Si spins.

Consider the simplified system consisting of a single ^{29}Si spin (index j, $\mathbf{A}^{ej} = 0$) coupled to the ^{31}P and electron, starting from an initial state given by $\rho = \frac{1}{2}\mathbb{1} + \frac{p}{2}\sigma_z^P$, corresponding to a polarization p of the ^{31}P spin and an unpolarized ^{29}Si. At the 2.3 T matching condition, the ^{31}P and ^{29}Si polarization will evolve as

$$\langle\sigma_z^P\rangle(t) = \frac{p}{2}(1 + \cos(\omega_{Pj}t)) , \qquad \langle\sigma_z^j\rangle(t) = \frac{p}{2}(1 - \cos(\omega_{Pj}t)) ,$$

where $\omega_{Pj} = \left(D_{xx}^{Pj} + D_{yy}^{Pj}\right)$. In the presence of spin-spin relaxation and the ^{31}P hyperpolarization process, this will result in a polarization p on the ^{29}Si. In contrast, at the 6.7 T matching condition, $\Delta_j^- = 0$ and the ^{31}P and ^{29}Si polarization will evolve as

$$\langle\sigma_z^P\rangle(t) = \frac{p}{2}(1 + \cos(\omega'_{Pj}t)) , \qquad \langle\sigma_z^j\rangle(t) = -\frac{p}{2}(1 - \cos(\omega'_{Pj}t)) ,$$

where $\omega'_{Pj} = \sqrt{4{D_{xy}^{Pj}}^2 + \left(D_{xx}^{Pj} - D_{yy}^{Pj}\right)^2}$. In this case, a polarization p on ^{31}P results in a polarization $-p$ on ^{29}Si. We note that the effective dipolar couplings at 2.3 T and 6.7 T also differ in magnitude ($\{\omega_{Pj}\}$ and $\{\omega'_{Pj}\}$), but we do not consider its effect further.

It is clear from the energy level structure and Eq. 6.11 that the polarization transfer from the ^{31}P is only allowed in the excited state ($|\uparrow_e\rangle$) manifold of the electron spin. At 4.2 K and 6.7 T, the electron polarization is 79%, such that the electron spin is in the ground state for a majority of the time. However, it is frequently driven to the excited state by the electron spin-lattice relaxation process with the timescale T_1^e. Since there is a difference of A_{eP} in the precession frequencies of ^{31}P in the two manifolds, the off-diagonal components of the density matrix do not remain coherent across the jumps induced by T_1^e, resulting in an effective "reset" of the coherent polarization exchange between the ^{31}P and ^{29}Si. As a result, the rate of the ^{31}P-^{29}Si polarization transfer is dependent on the T_1^e. It is also dependent on $\kappa'_{D^+\rightarrow D^0}$, since the defect ionization and photoneutralization process has a similar effect, with the polarization transfer being suppressed in the D^+ state. The coherent polarization exchange term above has a cosine time dependence, which means that when $\{T_1^e, {\kappa'_{D^0\rightarrow D^+}}^{-1}\} < \{{\omega'_{Pj}}^{-1}\}$, the average flux (time derivative) of the polarization transferred decreases with decreasing lifetimes. The maximum possible value for ω'_{Pj} is $\sim$ 200 Hz for ^{29}Si occupying adjacent lattice sites, compared to the measured T_1^e $\sim$ms in the dark [4]. Therefore, we expect most ${\omega'_{Pj}}^{-1}$ to be in this regime. As a result, the rate of ^{31}P-^{29}Si polarization transfer is expected to be reduced with optical pumping, which shortens T_1^e and increases $\kappa'_{D^0\rightarrow D^+}$. In the infinitely short relaxation time limit ($\{T_1^e, {\kappa'_{D^0\rightarrow D^+}}^{-1}\} \ll \{{\omega'_{Pj}}^{-1}\}$), the polarization transfer will be suppressed. This can be thought of as a quantum Zeno effect [100], where the constant "measurement" freezes the evolution under the dipolar Hamiltonian.

Let us briefly consider the implications of this for the ^{31}P spin. At the matching condition, the polarization transfer to ^{29}Si is an additional relaxation process, resulting in shorter T_1^n and a lower effective polarization. The effect is expected to be maximal in the absence of optical pumping, since $T_1^e < \{{\omega'_{Pj}}^{-1}\}$, and reduced by optical pumping due to the resulting reduction in T_1^e and increase in $\kappa'_{D^0\rightarrow D^+}$.

6.3 Experimental Results and Analysis

Experiments in this chapter were performed at two magnetic fields, 6.6 T and 6.7 T, at a temperature of 4.2 K. This temperature was preferred over 1.3 K for two reasons: the ready availability of data from previous measurements in natural abundance silicon at this temperature [7] and the relatively long timescales for ^{29}Si dynamics, which make maximizing the single shot hold time of the cryostat an important practical consideration. The two channel double resonance probe described in Ch. 4 was used, and the sample was a

natural abundance (4.7% ^{29}Si) silicon crystal of dimensions 8 mm $\times$ 3 mm $\times$ 2 mm , with phosphorus doping of 6×10^{15} cm^{-3}. The optical setup described in Ch. 4 and used for the experiments in Ch. 5 was used. However, we do not expect the same nonuniform laser distribution at 4.2 K as simulated for the experiments at 1.3 K in Ch. 5. The boiling LHe at 4.2 K has a large amount of helium bubbles, which cannot form in superfluid helium at 1.3 K. Since the refractive indices for helium gas and liquid are different, these bubbles scatter the incident laser light and are expected to smear out the light distribution over the sample. There may still remain some variations over a mm scale, but this has no consequences for the experiments in this chapter.

The ^{31}P measurements were carried out using the CPMG echo detection scheme described in Ch. 4, since the signal-to-noise ratio (SNR) on the free induction decay (FID) was low. The data was acquired over several months of experiments. Reference measurements (^{29}Si polarization after 4800 s of optical pumping at full laser power) over time indicate that any systematic errors due to thermal cycling or drift in laser power were within the error bars, except for two discrete events when the optical setup was modified to incorporate additional ND filters and when the cryostat was moved in and out of field as a safety requirement while changing the magnetic field. Across these events, the change was $\sim$ 12.5%. Since it is not possible to unambiguously assign the change in signal to a single cause (drift in laser power, change in sample position relative to coil, etc), the data was divided into three groups, with no plot containing data points from more than one group. Therefore, it is not valid to compare the signal amplitude (a.u) across different plots unless explicitly done in the text.

6.3.1 Electron-driven ^{29}Si Polarization

The phononic model predicts that optical pumping should generate a negative bulk ^{29}Si polarization, which is the same direction as the ^{29}Si thermal polarization ($p_T < 0$). In order to quantify the polarization, a reference measurement is necessary. However, we are not able to measure steady state thermal polarization at 4.2 K since the T_1^n is too long. Instead, we use the signal measured from the sample left overnight in the magnetic field at room temperature (where the $T_1^n \sim 5000$ s), immediately after the cool down (which takes 3000-4000 s) using a 90 deg. pulse as a reference. The data is shown in Fig. 6.3. Since T_1^n becomes longer at lower temperatures, the measured signal should originate from a polarization which is not substantially larger than the room temperature polarization. Therefore, this measurement allows us to put a lower bound on the laser induced polar-

ization, which is 6×10^{-6} after 4800 s of optical pumping. Comparing the phase of the reference signal with the laser induced polarization signal, we conclude that the laser induced polarization is negative, consistent with our expectation.

Next, we measure the polarization growth as a function of lasing duration at maximal laser power, shown in Fig. 6.4. The buildup curve shows a constant increase with time after an initial slow rise in rate, indicating that we are far from the steady state polarization. The fact that the rate of polarization growth at short times is slower than that at longer times is indicative of a second order process, such as the polarization of the core followed by spin diffusion to the bulk. This leads us to believe that the polarization during optical pumping with above-bandgap light (1047 nm) at 4.2 K originates from the ^{31}P defect site.

Let us look at the laser power dependence of the ^{29}Si signal. A comparison between the temporal dependence of the laser polarization at full laser power and 2.37 % laser power (gray circles) is plotted in Fig. 6.5, with the inset showing the two buildups normalized to their respective 4800 s signals. The excellent overlap of the two curves is possible in two regimes: at a long timescale compared to diffusion rate, if the diffusion coefficients are equal, or in the very short time regime, irrespective of diffusion coefficient. However, we are expected to be in a long timescale regime at 4800 s for maximal laser power, based on the upper bound of 913 s on the diffusion timescale assuming $D_{CB} = 0$. Therefore, the diffusion coefficients for the two laser powers must be comparable, despite the two orders of magnitude variation in laser power. This is contrary to the $\sqrt{I}$ scaling of the bound, suggesting that the contribution of D_{CB}, which is practically independent of laser power, is dominant. This supports our expectation that the diffusion barrier is not a rate limiting step.

Next, we measure the signal at other intermediate laser powers, at a fixed optical pumping duration of 4800 s, with the data shown in Fig. 6.6. The duration of 4800 s is chosen since it lies in the linear regime, and we cannot reach the steady state of the process within our experimental times. The data is consistent with the expectation that the polarization increases with laser power.

6.3.2 ^{31}P driven ^{29}Si polarization

In order to study the influence of the ^{31}P defect on the bulk ^{29}Si polarization under the resonant matching condition at 6.7 T, we adopt a pump-probe approach similar to that

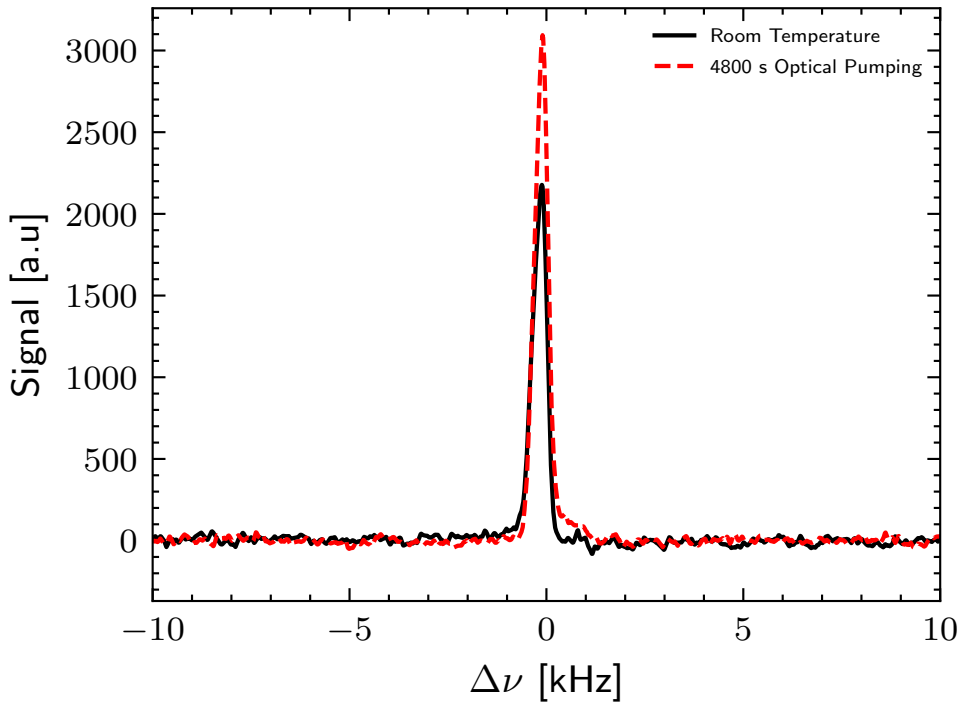

Figure 6.3: Comparison of the real part of the ^{29}Si spectra measured after a) polarizing at room temperature overnight followed by cooling to 4 K (black, solid) and b) initializing in the fully mixed state using a saturation train, followed by 4800 s of optical pumping at maximum laser power. The amplitude of the signals was used to estimate a lower bound of 6×10^{-6} on the laser induced polarization. Both spectra were acquired within 2 hours of each other, and the probe tuning/matching was verified to be stable and unchanged after each measurement. The signals were Fourier transformed with the same zeroth order phase correction. Since the measurement is phase sensitive, this allows us to conclude that the sign of the optical pumping driven polarization process is negative, the same as the thermal polarization.

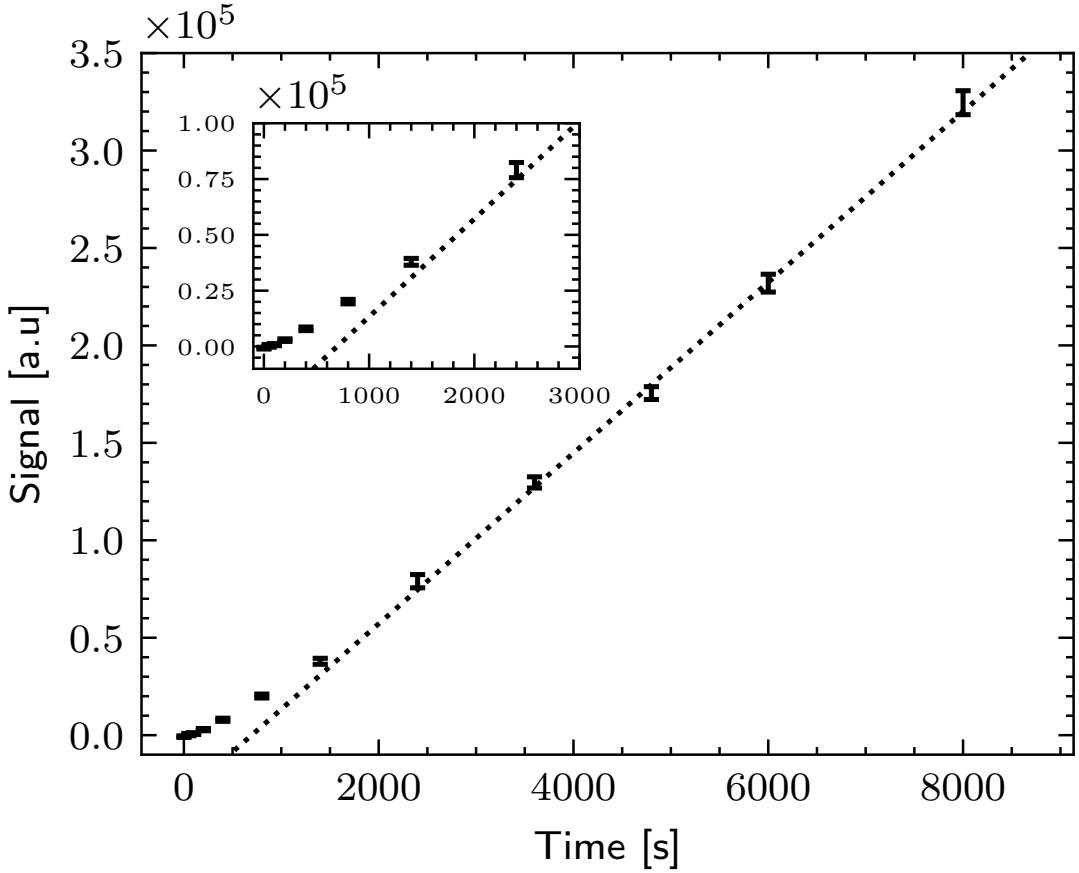

Figure 6.4: ^{29}Si Signal as a function of optical pumping duration, at 4.2 K and 6.6 T. The maximal laser power (430 mW) has been used. The dashed line is a linear fit to the measurements taken after irradiation for $\geq$ 2400 s, resulting in an x-intercept at 696 s. Inset: zoom in on the initial buildup of the polarization. The slow growth at short timescales is indicative of a second order process with a timescale of 100-1000 s, consistent with our model where the polarization originates from the ^{31}P defect and is transferred to the bulk through spin diffusion.

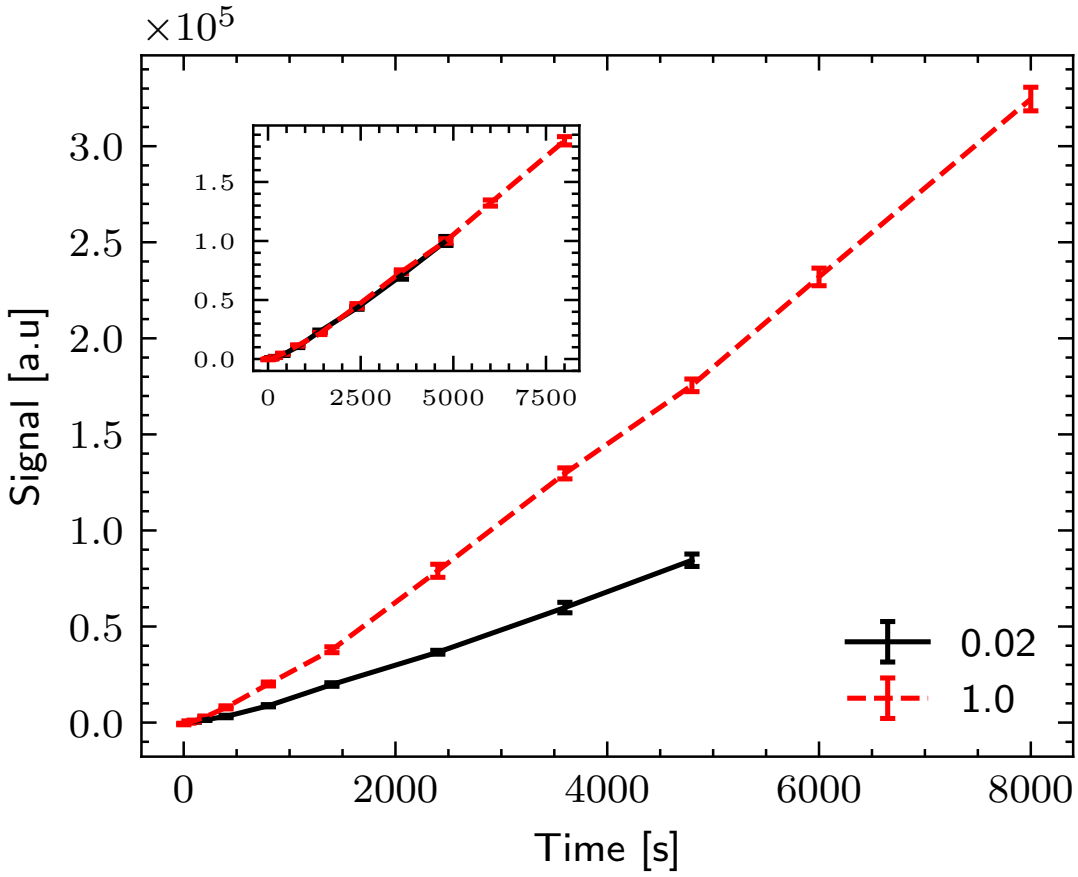

Figure 6.5: ^{29}Si buildup at 4.2 K and 6.6 T, for maximal laser power (red, dashed) compared to 2.37% laser power (black, solid). Inset shows the two curves individually normalized to their respective 4800 s points. The excellent overlap of the two curves in the inset indicates that the timescale of the second order process is independent of laser power. Since the lower bound on the spin diffusion rate is laser power dependent, we conclude that the true rate of spin diffusion across the barrier is faster than the lower bound.

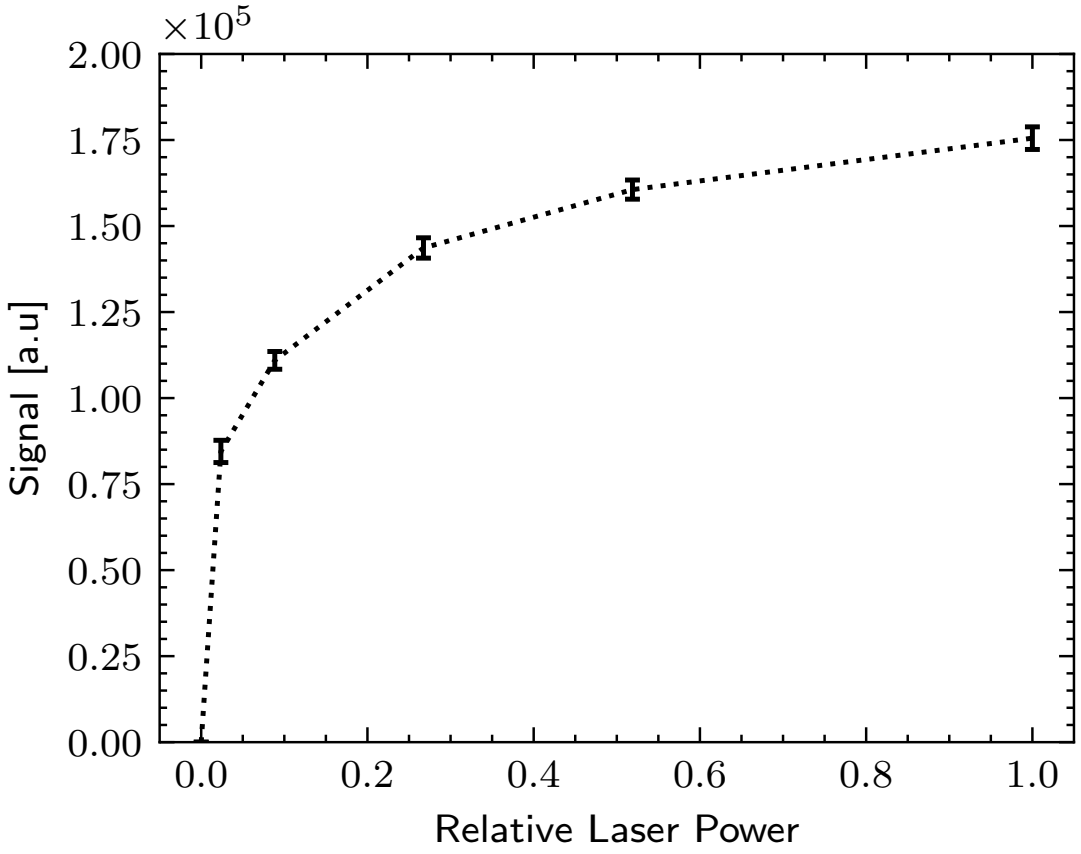

Figure 6.6: ^{29}Si Signal as a function of laser power, at 4.2 K and 6.6 T. The optical pumping duration was 4800 s. The power was varied using neutral density filters, whose attenuation is described in Table 4.1. The data demonstrates that the polarization rate grows as a function of laser power, as expected under the phononic process.

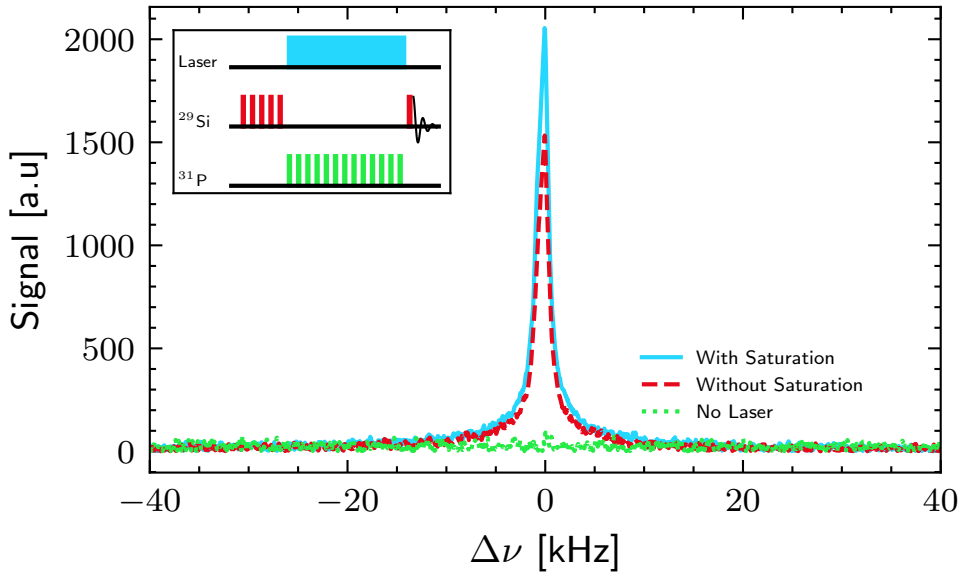

Figure 6.7: Comparison of ^{29}Si spectra at 6.7 T after initialization in the fully mixed state using a saturation train, followed by 4800 s of a) optical pumping at maximum laser power while simultaneously saturating the ^{31}P spins (blue, solid) b) optical pumping at maximum laser power without ^{31}P saturation (red, dashed) and c) no optical pumping (green, dotted). The data shows that the saturation of ^{31}P leads to greater polarization of ^{29}Si spins. A schematic representation of the pulse sequence used is shown in the inset to the figure. The sequence is composed of a ^{29}Si saturation train ($128 < \frac{\pi}{2}$ pulses, separated by 50 ms), followed by laser illumination for a fixed duration, and finally a $\frac{\pi}{2}$ pulse and FID detection of the silicon signal. For ^{31}P saturation, a continuous train of short, $< \frac{\pi}{2}$ deg. pulses (green) spread 20 ms apart is applied during the laser illumination period. We verified the effectiveness of our saturation trains by performing a measurement on each channel post saturation.

in Ch. 5, where we saturate the ^{31}P spin (D^0) and observe the effect on the ^{29}Si polarization. Fig. 6.7 shows that the saturation does indeed have an effect at 6.7 T, with the pulse program used illustrated in the inset. We verified that saturating off-resonance at 6.7 T and saturating on-resonance at 6.6 T has no effect, as seen in Fig. 6.8 and Fig. 6.9 respectively. This rules out the possibility of heating or other non-resonant effects playing a role.

In Fig. 6.10 we show the polarization buildup as a function the lasing time, with and without saturation of ^{31}P during the lasing. It is clear that saturation of the ^{31}P spins consistently results in an increase of the ^{29}Si polarization. This confirms that the contribution

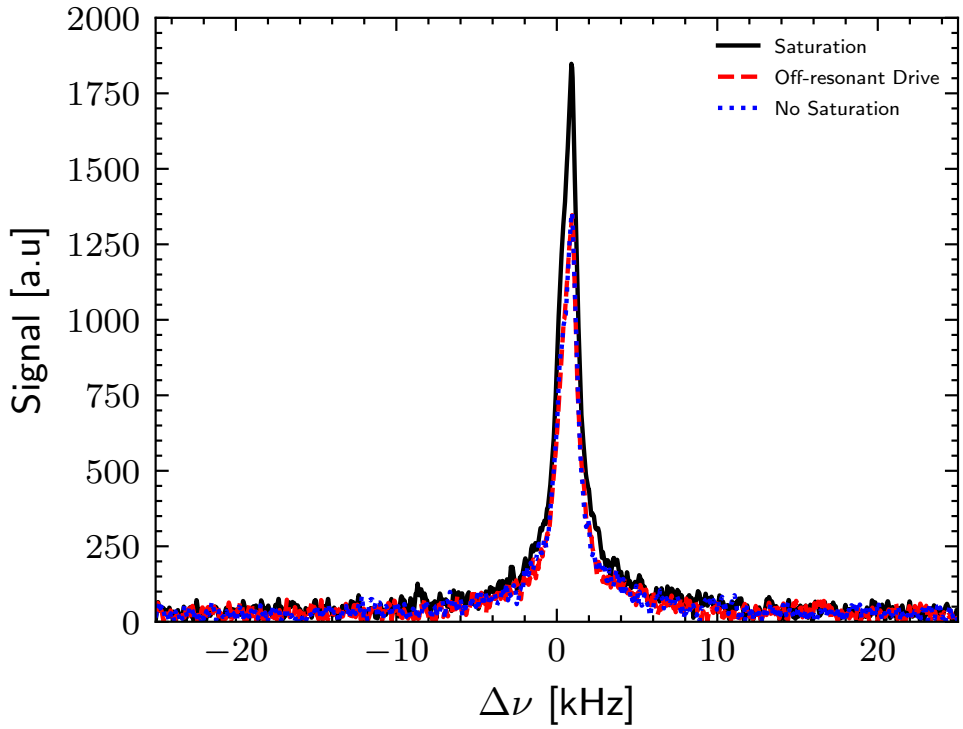

Figure 6.8: Comparison of ^{29}Si spectra at 6.7 T after initialization in the fully mixed state using a saturation train, followed by 4800 s of a) optical pumping at maximum laser power while simultaneously saturating the ^{31}P spins (black, solid) b) optical pumping at maximum laser power while pulsing with an identical saturation train as a), 10 MHz off resonance (red, dashed) and c) optical pumping at maximum laser power with no saturation (blue, dotted). The data shows that saturating off-resonance has no effect on the ^{29}Si polarization, while saturating on-resonance with ^{31}P leads to an increase in the ^{29}Si polarization. This, along with the data in Fig. 6.9 eliminates the possibility of heating or other non-resonant processes playing a role in the observed increase in the ^{29}Si polarization.

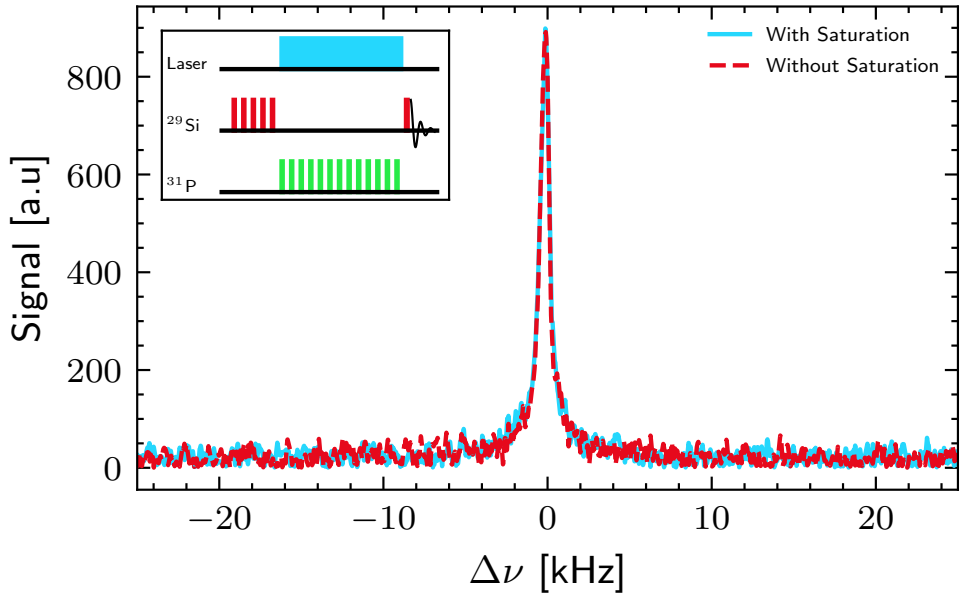

Figure 6.9: Comparison of ^{29}Si spectra at 6.6 T after initialization in the fully mixed state using a saturation train, followed by 4800 s of a) optical pumping at maximum laser power while simultaneously saturating the ^{31}P spins (blue, solid) and b) optical pumping at maximum laser power without ^{31}P saturation (red, dashed). A schematic representation of the pulse sequence used is shown in the inset to the figure. The data confirms that the ^{31}P-^{29}Si dipolar coupling is suppressed at 6.6 T.

of the ^{31}P is to polarize ^{29}Si in the opposite direction of the electron (and thermal) induced polarization, as predicted by the theory. The difference between the two, also shown in the figure, demonstrates the growth of the ^{31}P contribution with time. This contribution shows signatures of a second order/diffusion mediated process, similar to the electron contribution, where a linear fit to the long time points has a non-zero intercept. In our model, the ^{31}P driven polarization transfer to the bulk is determined by a combination of the ^{31}P-^{29}Si dipolar interaction $\{\mathbf{D}^{Pj}\}$ and the ^{29}Si-^{29}Si dipolar interaction $\{\mathbf{D}^{ij}\}$, whereas the electron driven transfer is determined by a combination of the hyperfine interaction term $\mathbf{A}^{ej}$ and $\{\mathbf{D}^{ij}\}$. Since $\mathbf{A}^{ej}$ and $\mathbf{D}^{Pj}$ are not monotonically related, the timescale associated with the two competing processes is expected to be different. This is consistent with the experimental data, where the curve for the contribution of ^{31}P does not overlap with the electron driven polarization curve when rescaled, unlike the ^{29}Si data in Fig. 6.5.

The laser power dependence of the ^{29}Si is shown in Fig. 6.11, where a lasing time of 4800 s was used. The data shows that the relative effect of the phosphorus induced polarization, as seen by the difference between the saturated and non-saturated polarization, becomes higher with laser power, leading to a larger effect of ^{31}P saturation on the observed ^{29}Si polarization. It also agrees qualitatively with the expected laser power dependence based on the increase in polarization rate and steady state from the phononic model and the laser power dependent measurements of ^{31}P shown in Fig. 6.12.

Finally, we take a look at the ^{31}P hyperpolarization under optical pumping. The time-dependent buildup at maximum laser power is shown in Fig. 6.13a, and the fit results in a time constant of 278 ± 13 s for the laser driven process. Fig. 6.13b shows the T_1^n decay of the polarization at 4.2 K, after optical pumping for 200 s. The extracted $T_1^n = 572 \pm 152$ s differs significantly from the value of 178 s reported for ^{31}P in natural abundance silicon at 6.7 T and 4.2 K [7], but it is consistent with the reported value of 718 s in isotopically enriched ^{28}Si at 6.7 T and 4.2 K [4, 7]. This agrees with our expectation that the matching condition at 6.7 T results in an additional relaxation mechanism for the ^{31}P nuclear spin, shortening the T_1^n.

The time-dependent ^{31}P buildups at 6.7 T for two different laser powers are shown in Fig. 6.14. The fit to an exponential buildup yields time constants of 105 ± 7 s at maximal laser power and 266 ± 27 s with quarter laser power (O.D 0.6). The 266 s time constant at quarter laser power is contradictory to the observed decay T_1^n of 178 ± 47 s [7] under a naive rate equation model, where any observed time constant should be shorter than the T_1^n. However, we noted in the previous section that the efficiency of transfer between

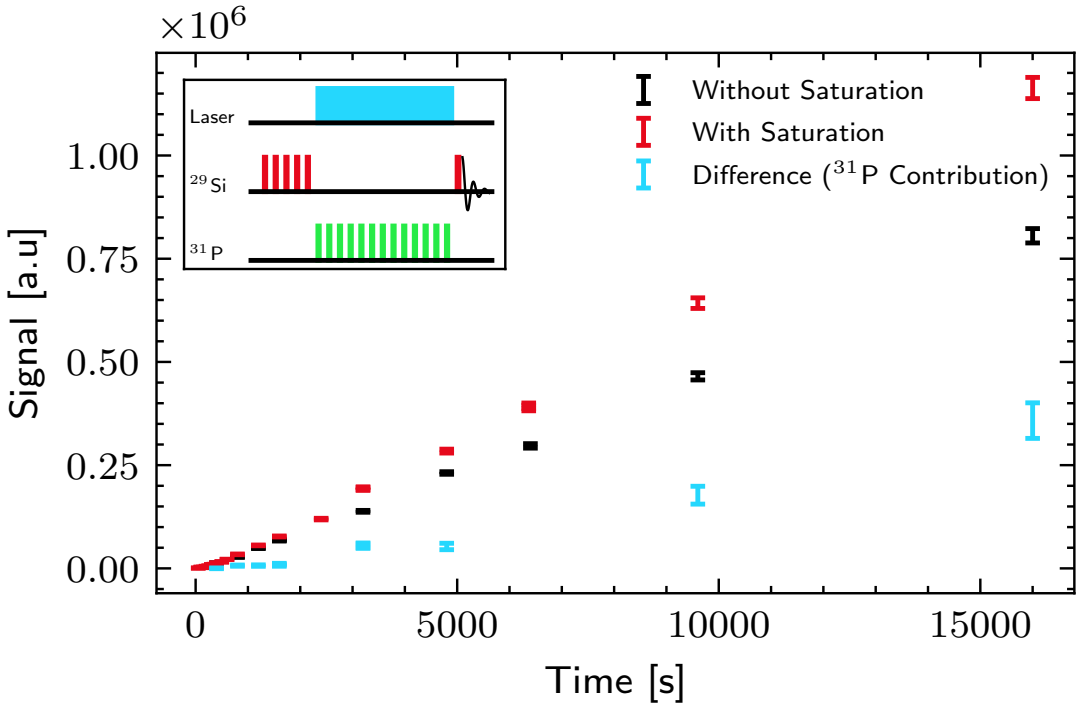

Figure 6.10: ^{29}Si polarization vs. laser irradiation time at 6.7 T, 4.2 K and maximal laser power. The measurement was performed with (red) or without (black) a saturation drive on the ^{31}P. The difference (blue) between the signals with and without saturation is the contribution of the ^{31}P driven process. The inset shows the pulse program used. The data shows that the phosphorus contribution also has a slow initial growth, but with a different timescale compared to the electron contribution. This leads us to believe that the ^{31}P-^{29}Si polarization transfer is mediated by a different subset of the core ^{29}Si as compared to the defect electron driven polarization process.

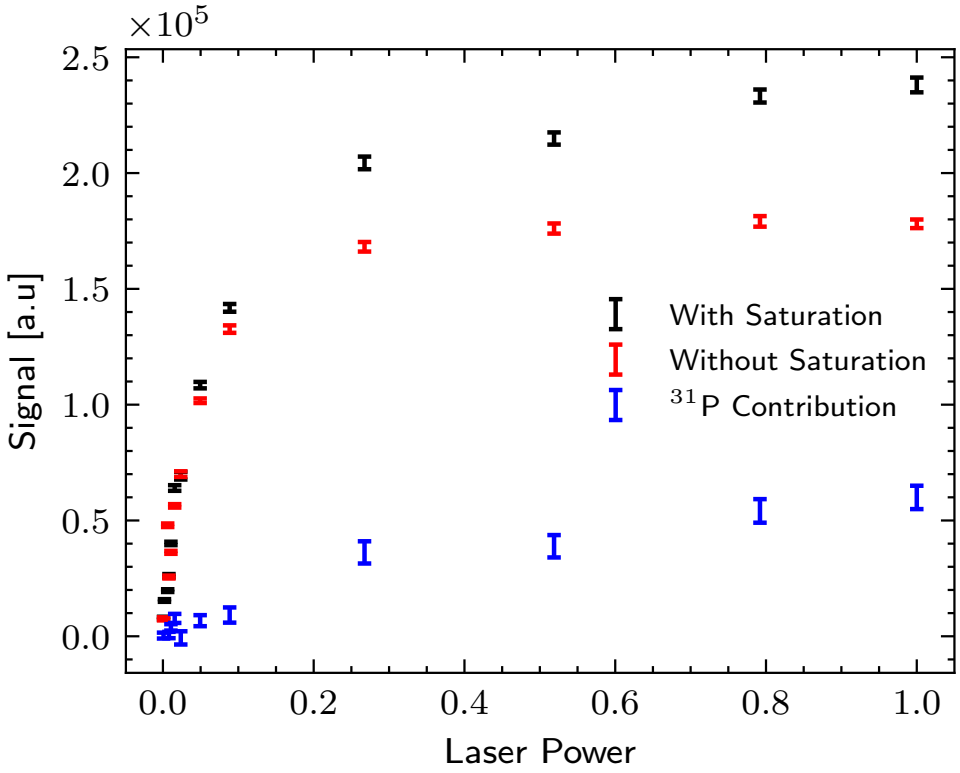

Figure 6.11: ^{29}Si Signal after optical pumping for 4800 s, as a function of laser power. The power was varied using neutral density filters, whose attenuation is described in Table 4.1. The data demonstrates that the ^{31}P contribution also grows as a function of laser power, which is expected since the ^{31}P nuclear spin polarization rate increases with laser power.

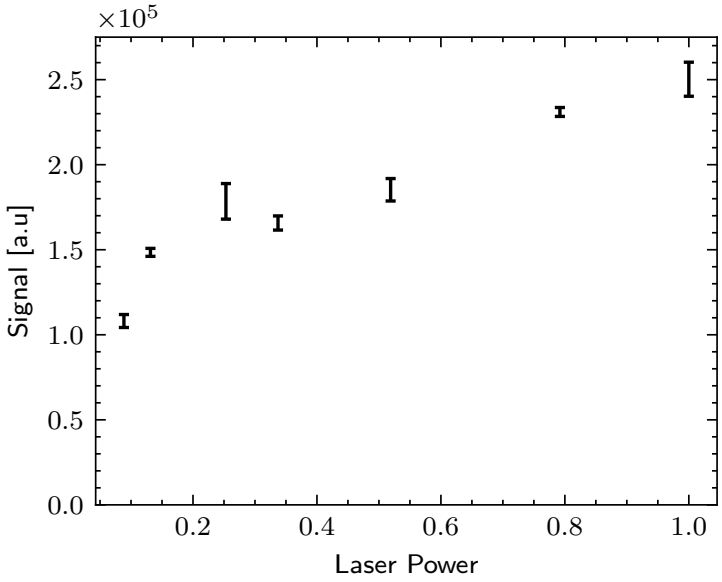

Figure 6.12: ^{31}P Signal after optical pumping for 1000 s at 6.7 T and 4.2 K, as a function of laser power. The power was varied using neutral density filters. The data agrees qualitatively with the ^{31}P contribution to the ^{29}Si signal in Fig. 6.11.

the ^{31}P and ^{29}Si is expected to reduce with laser power. This allows the buildup time constant under optical pumping to be longer than the decay T_1^n in the dark. Therefore, we conclude that the efficiency of the resonant transfer between ^{31}P and ^{29}Si is indeed laser power dependent, becoming less efficient at higher laser powers.

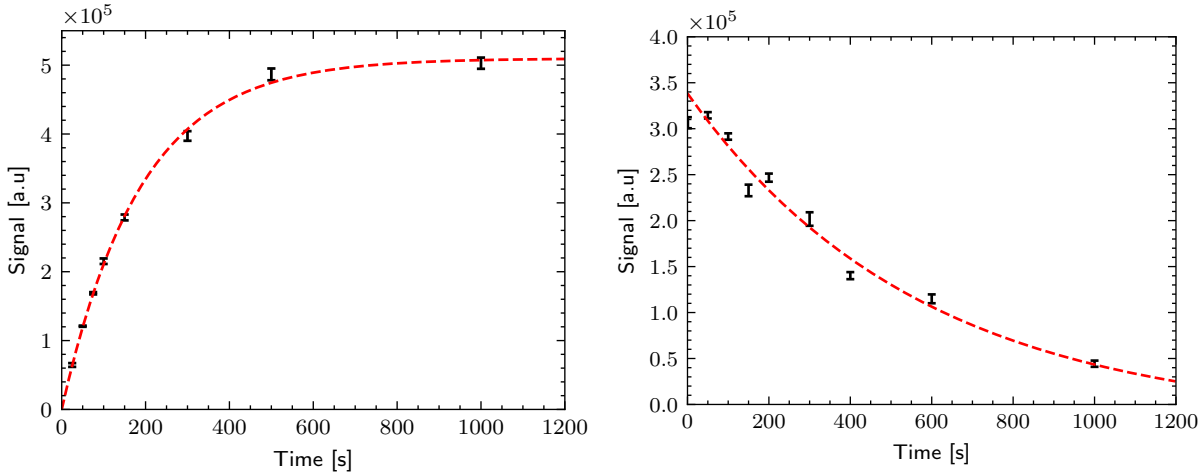

(a) Buildup at full laser power

(b) T_1 Decay after 200 s of optical pumping

Figure 6.13: Buildup and T_1^n decay of ^{31}P polarization at 6.6 T and 4.2 K. The red, dashed lines indicate fit to an exponential buildup/decay. The fit in Fig. 6.13b indicates that the T_1^n is 572 ± 152 s. This is much longer than the value of 178 ± 47 s measured at 6.7 T [7], but consistent with the reported value of 718 s in isotopically enriched ^{28}Si. The measurement demonstrates that the ^{31}P-^{29}Si coupling is the dominant decay process for the ^{31}P nuclear spin at 6.7 T. The fitted time constant for the buildup in Fig. 6.13a is 187 ± 5 s, resulting in a time constant of 278 ± 13 s for the laser driven process.

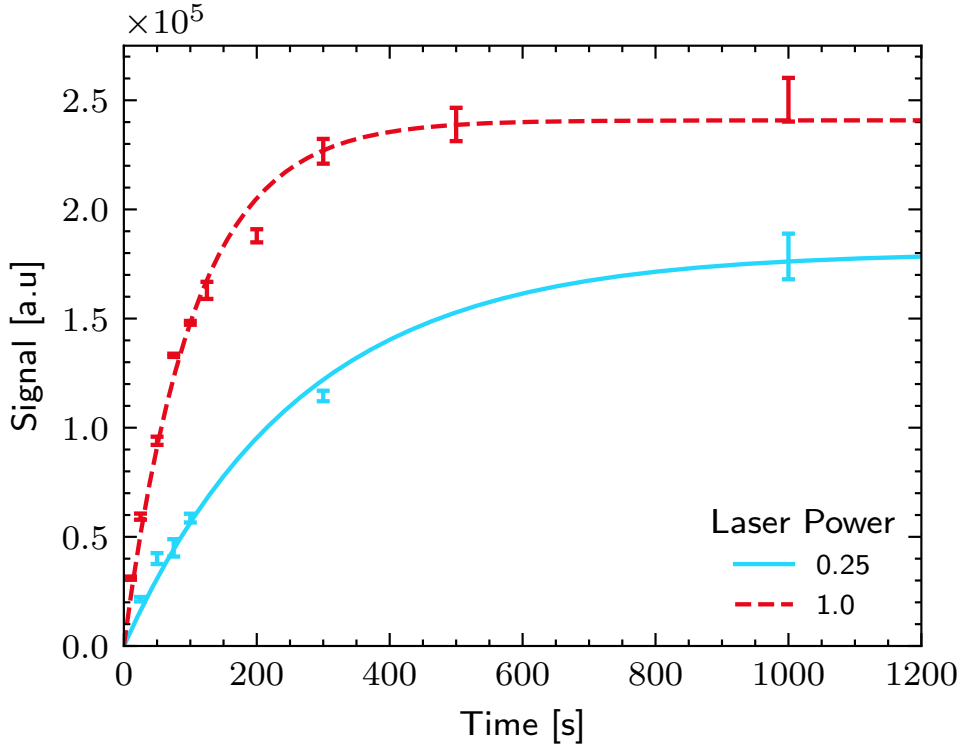

Figure 6.14: ^{31}P Signal vs. optical pumping time at 6.7 T for two different laser powers. The lines are fits to an exponential. The extracted time constants are 105 ± 7 s at maximal laser power (1.0) and 266 ± 27 s at quarter laser power (0.25). The quarter laser power time constant of 266 ± 27 is longer than the decay time constant of 178 ± 47 [7], driven primarily by the ^{31}P-^{29}Si resonant coupling. This indicates that the ^{31}P-^{29}Si polarization transfer rate reduces with laser power. We attribute this effect to the reduction in the electron T_1^e.

6.4 Numerical Simulations with Simplified Models

The qualitative analysis of experimental results in the previous section indicates that the ^{29}Si polarization originates from the defect site, with a contribution from both the defect electron spin as well as the ^{31}P nuclear spin. In this section, we will compare the data to two simplified numerical models, providing more insight into the processes involved.

6.4.1 Quantum Mechanical Model

Let us consider a model quantum mechanical system, comprising of the defect electron, ^{31}P, and three ^{29}Si spins, indexed by C_e (core, interacting with electron), C_P (core, interacting with phosphorus) and B (bulk). We focus on the effect at 6.7 T and comparison with the experimental data in this section. We consider the C_e spin to be in contact with the electron spin, the C_P spin to be coupled to the ^{31}P spin and the bulk ^{29}Si spin to be interacting with the two core spins. Therefore, $\{\mathbf{D}^{PC_P}, \mathbf{D}^{C_pB}, \mathbf{D}^{C_eB}, \mathbf{A}^{eC_e}\} \neq 0$ and $\{\mathbf{A}^{eB}, \mathbf{A}^{eC_P}, \mathbf{D}^{PB}, \mathbf{D}^{PC_e}\} = 0$. We can write the Hamiltonian as

$$\begin{aligned} H = &\frac{\omega_e}{2}\sigma_z^e + \frac{\omega_P}{2}\sigma_z^P + \frac{\omega_{Si}}{2}\left(\sigma_z^{C_e} + \sigma_z^{C_P} + \sigma_z^B\right) + \frac{A_{eP}}{4}\vec{\sigma}^e \cdot \vec{\sigma}^P + \frac{1}{4}\vec{\sigma}^e \cdot \mathbf{A}^{eC_e} \cdot \vec{\sigma}^{C_e} \\ &+ \frac{1}{4}\vec{\sigma}^P \cdot \mathbf{D}^{PC_P} \cdot \vec{\sigma}^{C_P} + \frac{1}{4}\vec{\sigma}^{C_e} \cdot \mathbf{D}^{C_eB} \cdot \vec{\sigma}^B + \frac{1}{4}\vec{\sigma}^{C_P} \cdot \mathbf{D}^{C_PB} \cdot \vec{\sigma}^B \ . \end{aligned} \tag{6.15}$$

Here, we treat the hyperfine interactions as time independent, and simulate the effect of the optical pumping with a cross-relaxation process induced by Lindblad dissipation operators. We consider the effect of saturation by adding a RF drive, applied at the transition frequency $\omega_P^{\downarrow} = \left(\omega_P - \frac{A_{eP}}{2}\right)$ of the ^{31}P nuclear spin in the ground state manifold of the electron spin. The total Hamiltonian can be simplified by going into the interaction frame of

$$H_0 = \frac{\omega_e}{2}\sigma_z^e + \frac{\omega_P}{2}\sigma_z^P + \frac{A_{eP}}{4}\sigma_z^e\sigma_z^P - \left(\frac{\omega_P}{2} + \frac{A_{eP}}{4}\right)\left(\sigma_z^{C_e} + \sigma_z^{C_P} + \sigma_z^B\right) \ . \tag{6.16}$$

After performing the rotating wave approximation, we get

$$\begin{aligned} H \simeq &\frac{\Delta_{Si}}{2}\left(\sigma_z^{C_e} + \sigma_z^{C_P} + \sigma_z^B\right) + \frac{A_{zz}^{eC_e}}{4}\sigma_z^e\sigma_z^{C_e} + \frac{D_{zz}^{PC_e}}{2}\sigma_z^P\sigma_z^{C_e} + \frac{D_{zz}^{PC_P}}{2}\sigma_z^P\sigma_z^C \\ &+ \left(\frac{D_+^{PC_P}}{2}\sigma_+^P\sigma_+^{C_P} + \frac{D_-^{PC_P}}{2}\sigma_-^P\sigma_-^{C_P}\right)|\uparrow_e\rangle\langle\uparrow_e| + \frac{D_{+-}^{C_eB}}{2}\left(\sigma_+^{C_e}\sigma_-^B + \sigma_-^{C_e}\sigma_+^B\right) \\ &+ \frac{D_{+-}^{C_PB}}{2}\left(\sigma_+^{C_P}\sigma_-^B + \sigma_-^{C_P}\sigma_+^B\right) \ , \end{aligned} \tag{6.17}$$

with $\Delta_{Si} = \frac{\omega_P}{2} + \frac{A_{eP}}{4} + \omega_{Si}$, $D_{+-}^{C_{P/e}B} = D_{xx}^{C_{P/e}B} + D_{yy}^{C_{P/e}B}$ and $D_{\pm}^{PC_P} = D_{xx}^{PC_P} - D_{yy}^{PC_P} \mp 2iD_{xy}^{PC_P}$. For simplicity, we choose $D_{xy}^{PC_P} = 0$, such that $D_{+}^{PC_P} = D_{-}^{PC_P}$. In addition to the Hamiltonian, we need to consider the effect of relaxation, including the cross relaxation induced by optical pumping. We can write the master equation in Lindblad form as

$$\frac{d\rho}{dt} = i[H, \rho] + \sum_i L_i \rho L_i^\dagger \ , \tag{6.18}$$

where L_i are the operators corresponding to various relaxation processes. The primary relaxation processes involved are the electron T_1^e and the laser induced cross-relaxations. However, it is important to keep the effects of the frame transformation applied to the Hamiltonian in mind. For example, the electron T_1^e induces a ^{31}P T_2^n [4] since the nuclear spins have very different larmor precession frequencies in the two manifolds of the electron spin, between which it is driven by the electron T_1^e. This effect no longer occurs with the transformed Hamiltonian, since we are now in a rotating frame where these frequencies have been matched. Since the induced T_2^n has been calculated analytically [36], we include this using additional Lindblad dissipators. Therefore, the Lindblad dissipators are given by

$$L_+^e = \sqrt{\frac{1-p_e}{2\mathrm{T}_1^e}}\sigma_+^e \ , \qquad L_-^e = \sqrt{\frac{1+p_e}{2\mathrm{T}_1^e}}\sigma_-^e \ , \qquad p_e = \tanh\left(\frac{\hbar\omega_e}{2k_B T_e}\right),$$

$$L_+^P = \sqrt{\frac{1-p_P}{2\mathrm{T}_1^P}}\sigma_+^P \ , \qquad L_-^P = \sqrt{\frac{1+p_P}{2\mathrm{T}_1^P}}\sigma_-^P \ , \qquad p_P = \tanh\left(\frac{\hbar\omega_P}{2k_B T_e}\right),$$

$$L_{X,+}^{eP} = \sqrt{\frac{1-p_X^P}{2\mathrm{T}_X^{eP}}}\sigma_+^e\sigma_-^P \ , \qquad L_{X,-}^{eP} = \sqrt{\frac{1+p_X^P}{2\mathrm{T}_X^{eP}}}\sigma_-^e\sigma_+^P \ , \qquad p_X^P = \tanh\left(\frac{\hbar(\omega_e-\omega_P)}{2k_B T_p}\right),$$

$$L_{X,+}^{eC} = \sqrt{\frac{1-p_X^C}{2\mathrm{T}_X^{eC}}}\sigma_+^e\sigma_-^{C_e} \ , \qquad L_{X,-}^{eC} = \sqrt{\frac{1+p_X^C}{2\mathrm{T}_X^{eC}}}\sigma_-^e\sigma_+^{C_e} \ , \qquad p_X^C = \tanh\left(\frac{\hbar(\omega_e-\omega_{\mathrm{Si}})}{2k_B T_p}\right),$$

$$L_{Z,\downarrow_e}^P = \sqrt{\frac{1-p_e}{4\mathrm{T}_1^e}}\left|\downarrow_e\right\rangle\left\langle\downarrow_e\right|\sigma_z^P \ , \quad L_{Z,\uparrow_e}^P = \sqrt{\frac{1+p_e}{4\mathrm{T}_1^e}}\left|\uparrow_e\right\rangle\left\langle\uparrow_e\right|\sigma_z^P \ , \quad L_Z^B = \sqrt{\frac{1}{2\mathrm{T}_2^B}}\sigma_z^B \ .$$

Here, $L_\pm^e$ drive the electron spin-lattice relaxation and $L_\pm^P$ drive the ^{31}P spin-lattice relaxation, both to the bath/electron temperature T_e. $L_{X,\pm}^{eP}$ and $L_{X,\pm}^{eC}$ simulate the effect of the hyperfine coupling modulation under optical pumping, driving the electron-^{31}P and electron-^{29}Si cross-relaxation processes respectively, to effective temperature T_p. L_Z^B simulates the dipolar interaction driven spin-spin relaxation in the bulk. The electron T_1^e induced T_2^n is given by $L_{Z,\downarrow_e/\uparrow_e}^P$. Published values for T_1^e in ^{28}Si samples were used, which is justified since this is relatively unaffected by concentration and isotopic content below

Parameter	Value	Parameter	Value
T_p	11.17 K	T_e	4.2 K
$D_{\pm}^{PC_P}$	4.3 mHz	A_{eC}	1 Hz
$D_{+-}^{C_PB}$	13 mHz	$D_{+-}^{C_eB}$	0.1 Hz
T_X^{eC}	5.4×10^7 s	T_X^{eP}	44 s
T_1^e	10^{-3} s	T_2^B	12.5 ms

Table 6.1: Simulation parameters used in Fig. 6.15 for a five spin quantum mechanical simulation.

10^{16} cm^{-3} doping concentrations [102].

The results of the simulation are shown in Fig. 6.15. The values used are given in Table 6.1, with the parameters taken in order to get qualitative agreement with the experimental results, as seen in Fig. 6.10: the initial slow rise of the polarization, followed by a linear growth; and the increase in polarization when saturating the high frequency ^{31}P spin transition (in the electron ground state). The behaviour seen in the simulations agrees well with the qualitative arguments provided in the previous sections. The initial polarization timescale for the electron and ^{31}P contributions is governed by the value of D^{C_eB} and D^{C_PB} respectively. These are much faster than their respective core polarization rates, governed by T_x^{eC} and D^{PC_P}. The T_x^{eC} has to be much longer than the maximum experimental duration in order to result in the linear dependence of the polarization at the longer times.

6.4.2 Rate Equations Model

The model in the previous section is useful in demonstrating the quantum mechanical process that drives polarization transfer under the resonant matching condition, and provides good qualitative agreement with the data. However, it does not account for the fact that every electron / ^{31}P spin simultaneously polarizes many core ^{29}Si spins, and that there is more than one bulk spin per core spin. Since a full quantum mechanical simulation involving multiple core and bulk nuclei quickly becomes computationally expensive with increasing number of nuclei, we use a simplified rate-equation based description of the system instead. We divide the set $\{^{29}\text{Si}\}$ into three sets $\{C_e\}$, $\{C_P\}$ and $\{B\}$. $\{C_e\}$ corresponds to nearby ^{29}Si spins that see a significant hyperfine interaction and are pre-

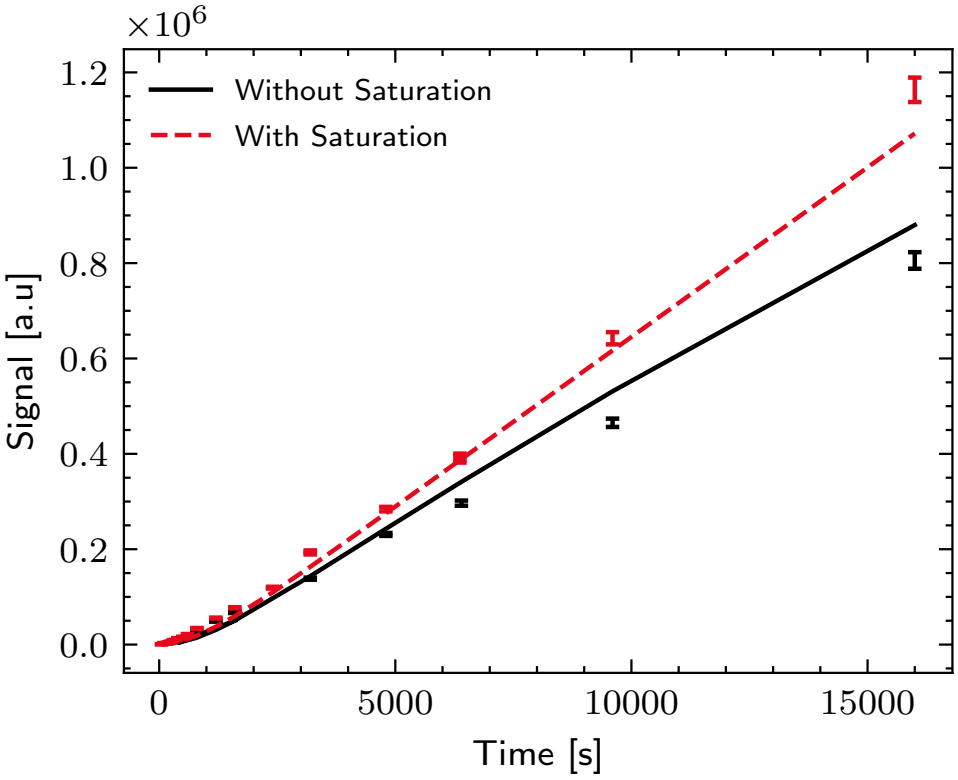

Figure 6.15: Bulk ^{29}Si polarization simulated with the five spin model, with parameters chosen for qualitative agreement with the experimental data. The parameters are listed in Table 6.1. The simulated bulk ^{29}Si polarization was scaled to experimental units by calibrating with the room temperature polarization signal.

dominantly polarized by the electron spin. $\{C_P\}$ corresponds to nearby ^{29}Si spins that see a smaller hyperfine interaction, and are polarized by the ^{31}P nuclear spin, and $\{B\}$ corresponds to the bulk ^{29}Si spins, which see a hyperfine shift ≤ 6.75 kHz (corresponding to the integration window for our measurement). The quantum-mechanically derived rate equation model [103] considers the time dependence of the polarizations, denoted by $\langle\sigma_z^P\rangle$, $\langle\hat{\sigma}_z^{C_e}\rangle$, $\langle\hat{\sigma}_z^{C_P}\rangle$ and $\langle\hat{\sigma}_z^B\rangle$, respectively. Note that the two sets of core ^{29}Si are not expected to be disjoint sets as assumed here. The model neglects differences in the hyperfine interactions seen by different core nuclei, which will in turn influence their polarization rates via the laser induced cross relaxation and ^{31}P. The model is also insensitive to diffusion within the core and how a trade-off between a stronger hyperfine interaction with the electron and faster spin diffusion may affect the relative contribution of various core nuclei. Instead, we obtain an average value for each of the rates. For each ^{31}P defect the model considers N_{C_e}, N_{C_P} and N_B spins in the three ^{29}Si sets. The temporal evolution of the polarization is given by:

$$\begin{pmatrix} \langle\sigma_z^P\rangle \\ \langle\hat{\sigma}_z^{C_e}\rangle \\ \langle\hat{\sigma}_z^{C_P}\rangle \\ \langle\hat{\sigma}_z^B\rangle \\ 1 \end{pmatrix}(t) = e^{Mt} \begin{pmatrix} 0 \\ 0 \\ 0 \\ 0 \\ 1 \end{pmatrix}, \tag{6.19}$$

where we start with all nuclear polarizations set to zero for simplicity. The rate matrix M is given by

$$M = \begin{pmatrix} -r_{1P} - r_{MW} - l_P - \frac{1}{2}d_{PC_P} & 0 & \frac{1}{2}d_{PC_P} & 0 & r_{1P}p_P + l_P p_e \\ 0 & -\frac{1}{2}d_{C_eB} - l_C & 0 & \frac{1}{2}d_{C_eB} & l_C p_e \\ \frac{1}{2N_{C_P}}d_{PC_P} & 0 & -\frac{1}{2N_{C_P}}d_{PC_P} - \frac{1}{2}d_{C_PB} & \frac{1}{2}d_{C_PB} & 0 \\ 0 & \frac{N_{C_e}}{2N_B}d_{C_eB} & \frac{N_{C_P}}{2N_B}d_{C_PB} & -\frac{N_{C_e}}{2N_B}d_{C_eB} - \frac{N_{C_P}}{2N_B}d_{C_PB} & 0 \\ 0 & 0 & 0 & 0 & 0 \end{pmatrix}, \tag{6.20}$$

where l_P and l_C are the laser induced polarization rates of the ^{31}P and C_e spins respectively. We assume, for simplicity, that this process drives the polarizations to the electron steady state p_e at $T_e = 4.2$ K. The ^{31}P spin-lattice relaxation rate is $r_{1P} = \mathrm{T}_1^{P-1}$, driving the ^{31}P to the thermal polarization p_P. The polarization transfer rate between the ^{31}P and C_P spins is d_{PC_P}. Similarly, the polarization transfer rate between the C_P and the bulk ^{29}Si spins is d_{C_PB}, and the rate between C_e spins and the bulk ^{29}Si spins is d_{C_eB}. Finally, the

Parameter	Value	Parameter	Value	Parameter	Value
N_B	3.9×10^5	$N_{C_{e/P}}$	1000	r_{RF}	10 s^{-1}
r_{1P}	1.7×10^{-3} s^{-1}	l_P	$3.6 \times 10^{-3} s^{-1}$	l_C	10^{-6} s^{-1}
d_{C_eB}	2.4×10^{-3} s^{-1}	d_{C_PB}	1.2×10^{-3} s^{-1}	d_{PC_P}	10^{-3} s^{-1}

Table 6.2: Parameters for the rate equation model, with the simulation shown in Fig. 6.16.

saturation rate of the ^{31}P nuclei is r_{RF}. We note that an implicit assumption in this model is that the "bath" (electron) is always polarized and unaffected by the number of core nuclei. This assumption is justified as long as $(N_{C_e} l_C + l_P)^{-1} \gg T_1^e$ i.e. the flow of polarization from the electron to the nuclei is not a significant contribution to its own relaxation.

The buildup of ^{29}Si bulk polarization was simulated for the experimental conditions experiments as seen in Fig. 6.10. This was done using Eq. 6.19, with the results shown in Fig. 6.16 and the parameters listed in Table 6.2. The following parameters were used based on known/assumed values: N_B was calculated based on the isotopic abundance of ^{29}Si (4.7%) and the doping concentration of ^{31}P in our sample. The ^{31}P laser induced polarization buildup and T_1^P decay measurements at 6.6 T, shown in Fig. 6.13, were used to calculate l_p and r_{1P}. The saturation rate r_{RF} was estimated from the saturation pulse length, Rabi frequency and duty cycle. The number of core ^{29}Si was assumed to be $N_{C_{e/P}} = 1000$. The remaining parameters d_{PC_P}, d_{C_PB}, d_{C_eB} and l_C were found by fitting the model to the data.

This (simplified) model captures the main features of the experimental data. It clearly shows the effect of the core to bulk ^{29}Si spin diffusion process on the initial ^{29}Si signal, and a linear growth at longer times. It also shows the decrease of the ^{29}Si polarization due to the ^{31}P induced polarization transfer, and its increase upon ^{31}P saturation. The fitted parameters are also consistent with our expectation that the limiting rate in the process is the polarization of the core.

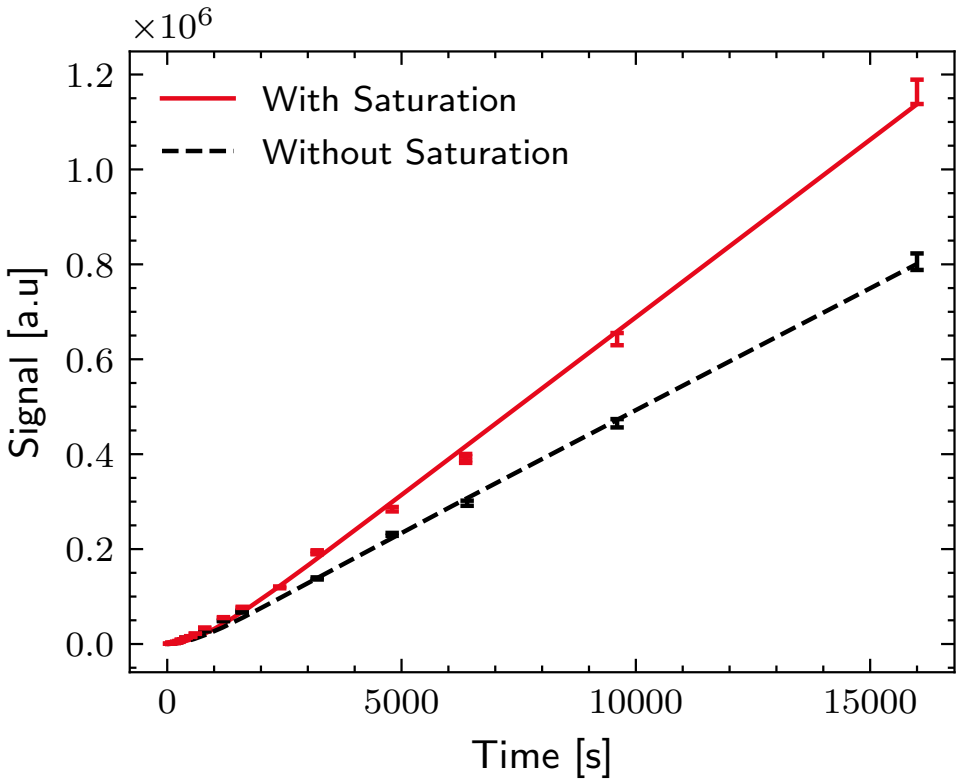

Figure 6.16: Rate equation based simulation of the ^{29}Si enhancement as a function of the lasing duration. The experimental data is also plotted. The simulation was performed using Eq. 6.19, with parameters given in Table 6.2. The simulated bulk ^{29}Si polarization was scaled to experimental units by calibrating with the room temperature polarization signal.

6.5 Conclusions

We have demonstrated that the polarization seen in ^{29}Si spins in bulk silicon under above-bandgap optical pumping originates from defect sites, in particular ^{31}P defects. We have isolated two processes which can contribute to it, associated with the defect electron and the ^{31}P nuclear spin. The phononic model proposed in this chapter is consistent with the observed time dependence as well as the sign of the polarization, and agrees qualitatively with the laser power dependence. We have also verified that the spin diffusion barrier is not a rate limiting step in this process, and that the rate of polarization transfer from ^{31}P is dependent on laser power.

6.6 Future Directions

In this section, we discuss how the insights provided by our work can be applied towards creating highly polarized bulk ^{29}Si. Since the T_1^e of the electron is shorter, its effective polarization capacity is much higher than that of the ^{31}P, making it a natural choice as a resource. However, we have seen that the ^{29}Si that couple effectively to the electron are likely a different subset from the ^{29}Si that couple effectively to ^{31}P. Since the ^{31}P-^{29}Si resonant transfer at 2.3 T is a zero quantum (ZQ) transition, the contributions from the electron and ^{31}P to the ^{29}Si polarization add at this field. Therefore, it may be possible to augment a polarization scheme based on driving electron-^{29}Si cross-relaxation with one utilizing the ^{31}P-^{29}Si resonant matching at 2.3 T. We note that since the ^{31}P is also polarized by the electron, the final polarization rate of a combined approach will still be limited by the electron spin relaxation rate.

We have shown that the rate of polarization of the nearby ^{29}Si by the electron is the limiting step under above-bandgap optical pumping. Based on the rate equation model parameters, it takes $(N_{C_e} l_C)^{-1} \simeq 10^3$ s to polarize one ^{29}Si per defect electron. This makes it impractical in terms of achieving near-unity bulk polarization. However, electric field driven modulation of the hyperfine interaction (AC Stark effect), as proposed in Ch. 5 for ^{31}P, may also be able to hyperpolarize the ^{29}Si. In particular, an electric field at $\omega_E = \frac{\omega_e - \omega_{\mathrm{Si}}}{2}$ would drive the electron-^{29}Si cross-relaxation through a quadratic Stark effect, and at $\omega_E = \omega_e - \omega_{\mathrm{Si}}$, it would drive the electron-^{29}Si cross-relaxation through a linear Stark effect. Since experimental measurements of the Stark effect have not been reported for the hyperfine coupled ^{29}Si, the required electric field amplitudes and whether the linear

or quadratic effect is dominant on average is nontrivial to estimate. However, the predominantly isotropic nature of the experimentally reported ^{29}Si hyperfine couplings means that modest ($\sim 10^{-3}$) Stark shifts can drive sub-second polarization of the core ^{29}Si. This is much faster than the above-bandgap process, as well as traditional DNP methods using resonant magnetic fields, which are limited by the long cross-relaxation times (Overhauser effect) or the strength of the anisotropic dipolar component relative to the nuclear Zeeman splitting (solid effect).

Our experiments showed that spin diffusion is not a limiting step under above-bandgap optical pumping. However, the rate equation estimate of $(N_{C_e} d_{C_e B})^{-1} \simeq 0.4$ s to polarize one ^{29}Si per defect electron suggests that it will become a limiting step once a faster polarization scheme for the core ^{29}Si is implemented. Using a higher ^{31}P doping concentration, and using isotopically enriched ^{29}Si, can reduce this limitation [91]. However, it also leads to worse coherence and relaxation times. However, the idea of short-circuiting of the diffusion barrier through the D^+ state may allow us to increase spin diffusion on demand without compromising on coherence and thermal relaxation times. We have also demonstrated that the polarization transfer between ^{31}P and ^{29}Si under the resonant matching condition is suppressed by a shortening of the electron T_1^e or a decrease in the D^0 state lifetime. This may present a challenge in utilizing ^{31}P as a resource, since lowering T_1^e is desirable for driving the electron-^{29}Si process. The challenge is partly overcome, in the experiments of Dluhy et al. [78] at 2.3 T, by resonantly pumping selective bound exciton transitions to create an inverted electron polarization. This keeps the ^{31}P-^{29}Si coupling on for a majority of the time, allowing for a more efficient transfer. However, the thermal electron T_1^e process limits the maximum lifetime of the excited state. As a result, the suppression of the ^{31}P-^{29}Si resonant coupling will not be eliminated with an inverted electron spin temperature generated by resonant optical pumping. If the temperature of the electron spins is inverted, the cross-relaxation is now always driven to a lower temperature, resulting in a ^{29}Si polarization in the $|\uparrow_{\mathrm{Si}}\rangle$ state. Similarly, the ^{31}P is also driven to the $|\uparrow_{\mathrm{P}}\rangle$ state by its cross-relaxation process. While the AC Stark drive as proposed above will increase the cross-relaxation temperature by saturating the transition, it remains lower than the negative electron spin temperature, resulting in much faster polarization of the nearby core spins. The resonant optical pumping scheme also drives defect ionization by an Auger recombination process, resulting in a short circuit of the diffusion barrier. We believe that such an approach, combining optical pumping with resonant electric fields, is required to create highly polarized bulk ^{29}Si.

Chapter 7

Hydrostatic Strain

In the previous chapters, we have seen that the hyperfine interaction of the electron with the nuclear spin is affected by changes to the electron wavefunction caused by strain. The experiments in Ch. 5 and Ch. 6 exploit this for hyperpolarization using incoherent processes. However, if the hyperfine interaction is modulated in a coherent manner, using strain [104] or electric fields [105], it can serve as a powerful tool for coherent control of the ^{31}P spins. In this chapter, we present some preliminary data that investigates the dependence of the hyperfine coupling in isotopically enriched ^{28}Si on hydrostatic strain.

7.1 Introduction

Investigations into the strain-^{31}P hyperfine coupling started with Feher's seminal work [106] and have generated renewed interest recently [6, 107]. These experiments induce hydrostatic as well as deviatoric strain by mechanical means [6] or through differential thermal contractions [107]. The results demonstrated a large linear dependence on the hydrostatic component, where the effect of the deviatoric component is symmetry constrained to be of quadratic or higher order [6]. The experiments relied on fitting to a generalized model accounting for a variety of simultaneous effects, including hyperfine shifts from the deviatoric component as well as a shift in the electron g-factor. In this section, we show preliminary measurements demonstrating that the sensitivity of NMR may allow us to measure the hyperfine shift dependence in a cleaner, more precise manner, by applying purely hydrostatic stress through changes in bath pressure.

7.2 Theory

The applied pressure P is equivalent to a negative hydrostatic stress. In the Voight notation, introduced in Ch. 1, it is written as

$$\vec{\sigma}_P = -P \times (1, 1, 1, 0, 0, 0) \tag{7.1}$$

The strain induced by this can be calculated from Hooke's law for continuous media, given by Eq. 1.21. The stiffness tensor for silicon is [108]

$$\mathbf{C} = \begin{pmatrix} c_{11} & c_{12} & c_{12} & & & \\ c_{12} & c_{11} & c_{12} & & & \\ c_{12} & c_{12} & c_{11} & & & \\ & & & c_{44} & & \\ & & & & c_{44} & \\ & & & & & c_{44} \end{pmatrix} \tag{7.2}$$

where $c_{11} = 165.7$ GPa, $c_{12} = 63.9$ GPa and $c_{44} = 79.6$ GPa. The strain induced by the hydrostatic stress is

$$\vec{\epsilon}_P = \epsilon_{hs} \, (1, 1, 1, 0, 0, 0)$$
$$\epsilon_{hs} = -\frac{P}{c_{11} + 2c_{12}}$$

where ϵ_{hs} is the hydrostatic strain. At $P = 1$ atm, this corresponds to a strain of -3.45×10^{-7}. Therefore, the infinitesimal strain assumption is justified. We saw in Ch. 2 that the ^{31}P hyperfine interaction up to first order in strain is

$$A_{eP}(\vec{\epsilon}) = A_{eP}(0) \, (1 + K\epsilon_{hs}) \tag{7.3}$$

where K is a constant. The NMR peak in our experiments is at the resonance frequency of the ^{31}P in the ground state manifold of the electron spin,

$$\omega_P^{\downarrow e} = \gamma_P B_0 + \frac{A_{eP}}{2}$$

The strain is not expected to introduce an observable chemical shift on the nuclear spin, and any change in the resonance frequency of the hyperfine shifted ^{31}P can be attributed to the change in the hyperfine interaction itself. Therefore, we can write

$$\omega_P^{\downarrow e}(\epsilon_{hs}) = \left(\gamma_P B_0 + \frac{A_{eP}(0)}{2}\right) + \frac{A_{eP}(0)}{2} K\epsilon_{hs} \tag{7.4}$$

The hydrostatic strain dependence K can now be extracted from a linear fit of the data to the above equation. Previous experiments [6] report the value to be $K = 79 \pm 25$. Therefore, the strain of -3.45×10^{-7} corresponding to 1 atm pressure is expected to generate a shift of 1.6 ± 0.5 kHz in $\omega_P^{\downarrow e}$. In comparison, the best linewidth achieved in our experiments is ~ 300 Hz.

7.3 Experimental Results

The measurements were performed in a liquid helium bath. The temperature of the bath is almost inextricably linked with the pressure, since the heat capacity of the helium liquid is small compared to various heat loads, such that a change in pressure leads to an almost immediate change in temperature. However, Fig. 7.1 shows that the heat capacity has a sharp peak at the superfluid transition of ^{4}He at 2.17 K. As a result, variations in pressure do not lead to an immediate change in temperature around 2.17 K. Therefore, the measurements were performed at this temperature, with the desired pressure achieved by venting the cryostat to a helium gas bottle after pumping to a lower pressure, and was measured using an analog pressure gauge. The analog pressure gauge uses ambient pressure, which may vary by 4% over a few hours, as a reference. We utilize the weather data [109] to verify that pressure variation over the course of our experiment duration was $\sim 0.2\%$. The ^{31}P were first hyperpolarized with optical pumping at 1.3 K and a small tip angle was used for the detection pulse in order to perform all measurements with a single shot of hyperpolarization.

The results of the measurements are plotted in Fig. 7.2, with a fit to a linear dependence which yields the parameter

$$K = 40 \pm 1$$

This is slightly lower than the previously measured value of $K = 79.2 \pm 25.7$ [6], and has a higher precision. However, we caution that this was a preliminary, proof-of-principle experiment, and is not guaranteed to be more accurate. In the next section, we discuss a setup design which allows us to minimize systematic errors.

We also noted the presence of a frequency shift $\sim$ 1 kHz between 4.2 K and 2.2 K at 1 atm pressure. Steger et al [110] have reported a difference of 3116 Hz between the hyperfine interaction at 4.2 K/1 atm and 1.3 K/1 Torr, consistent with our observations.

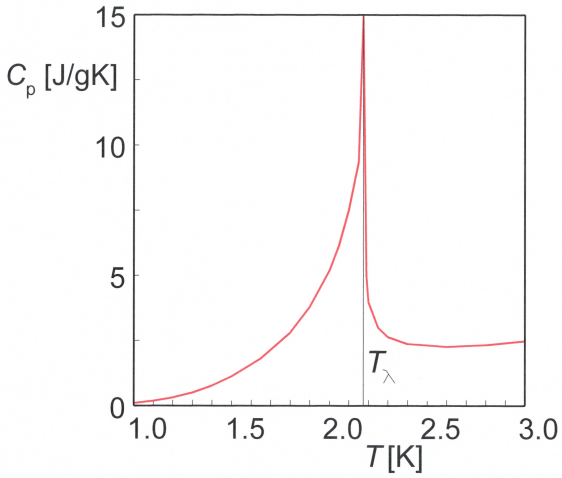

Figure 7.1: Heat capacity of Helium at low temperatures. The sharp peak at 2.17 K corresponds to the superfluid transition, and is called the λ-point. Figure reproduced without modification from Wikimedia Commons under CC-BY-3.0

This suggests that there may be a temperature dependence to the hyperfine shift as well. Temperature dependent measurements with constant pressure are necessary to study this effect.

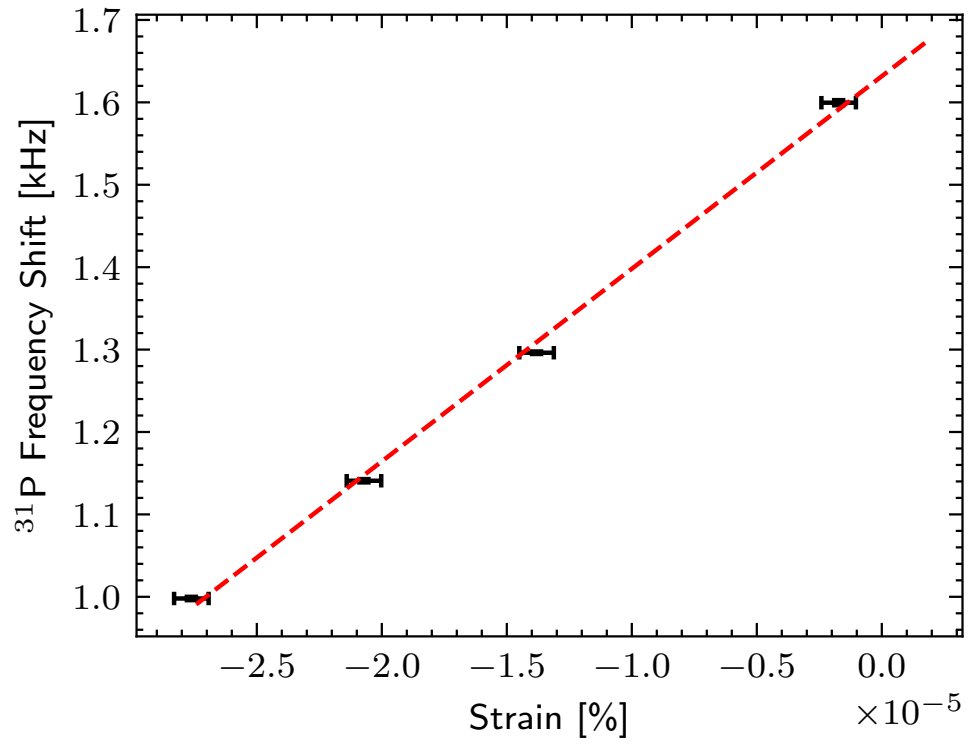

Figure 7.2: The frequency of the ^{31}P NMR peak (relative to the spectrometer frequency of 174.104 MHz), as a function of hydrostatic strain. The peak frequency and error bars were calculated based on a least squares fit of the Fourier transform of the FID with a matched exponential filter to a Lorentzian lineshape. The error bars on the strain are based on the resolution of the analog pressure gauge. The red dashed line is a linear fit to the data.

7.4 Conclusions and Future Directions

We have demonstrated that inductively detected NMR with hyperpolarized ^{31}P can be used to measure the change in the hyperfine coupling with hydrostatic strain and temperature. The obtained value $K = 40 \pm 1$ is lower than previous measurements. While the precision in this preliminary measurement is high, a few improvements are necessary to ensure its accuracy, which we detail below.

In order to isolate the strain and temperature dependence of the hyperfine interaction, it is important to be able to change the pressure and temperature independently, and minimize any drifts over time. For this, we suggest a setup outlined in Fig. 7.3, where the sample and coil sit inside a sealed copper cell. Laser illumination may be provided through an optical window or fiber. The temperature of the cell walls (and therefore the liquid helium inside) is determined by the temperature of the external bath. However, the pressure inside is controlled by the back pressure regulator and regulated supply assembly connected to the cell. Therefore, it is possible to perform measurements at a desired combination of temperature and pressure, as long as it corresponds to a liquid state on the helium phase diagram. An absolute pressure sensor should be used to log the ambient pressure for each measurement.

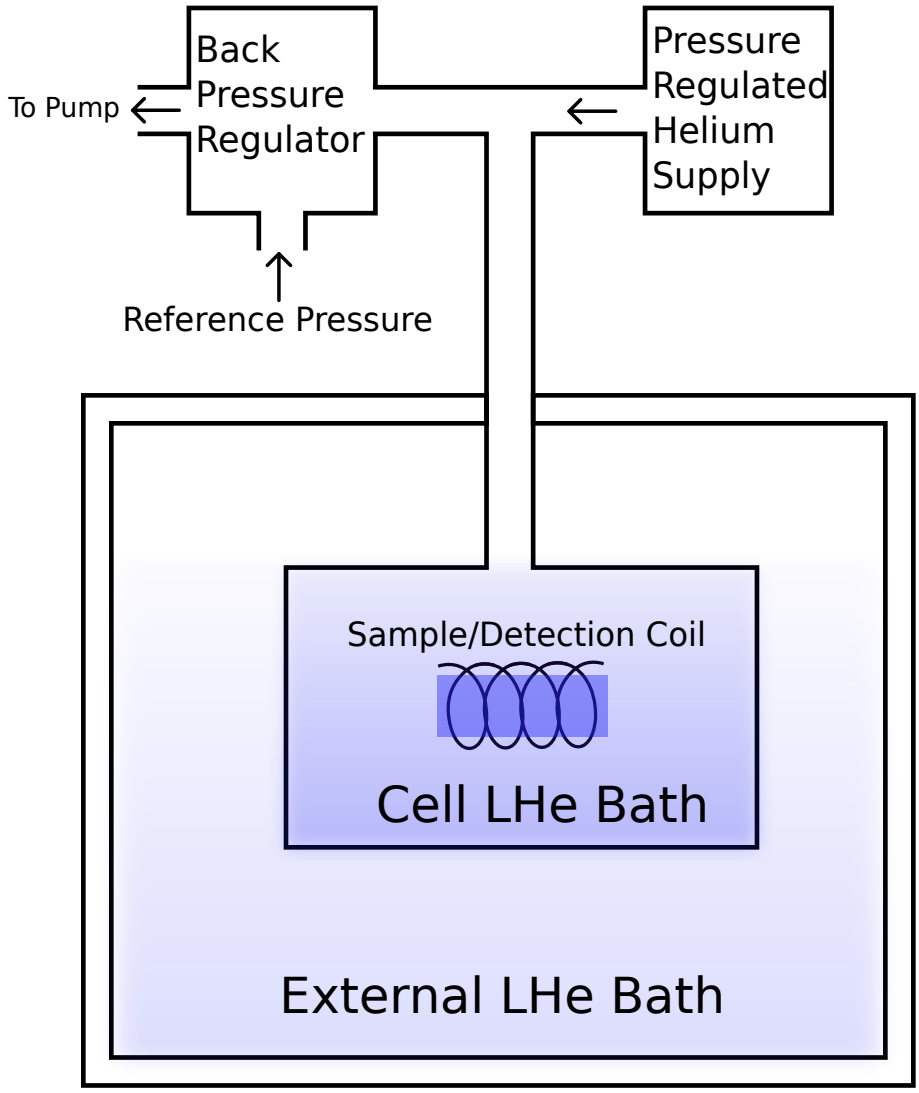

Figure 7.3: Schematic of setup for separate control of temperature and hydrostatic strain. The temperature is set by the temperature of the external LHe bath, while the hydrostatic strain is determined by the pressure settings on the supply and back pressure regulator. The reference pressure is typically ambient pressure, but may be modified to increase the range of operation of the back pressure regulator.

Chapter 8

Conclusions

In this thesis, we have explored polarization and relaxation processes which are driven by above-bandgap optical pumping in phosphorus-doped silicon at low temperatures. We have demonstrated that the ^{31}P nuclear spins in isotopically enriched ^{28}Si are hyperpolarized by phononic modulation of the hyperfine interaction, which drives the electron-^{31}P cross-relaxation to a higher effective temperature compared to that of the electron spin-lattice relaxation process. Our analysis suggests that the limiting rate in this process is the cross-relaxation, and shows that a resonant modulation of the hyperfine interaction with electric fields, using the quadratic Stark effect, may allow us to hyperpolarize the nuclear spins at a millisecond timescale, much faster than is currently possible with optical methods. We have proposed a future experiment to implement this approach, and elaborated on some practical considerations and suitable parameter regimes for such an experiment.

Our experiments in natural abundance silicon have demonstrated that the polarization of the bulk ^{29}Si spins generated by optical pumping originates from the ^{31}P defect. We used a pump-probe type experiment to isolate two processes which contribute to this polarization. The first is driven by the defect electron-^{29}Si hyperfine coupling, which results in a ^{29}Si polarization aligned with its thermal polarization, corresponding to a positive spin temperature. The second is driven by the ^{31}P-^{29}Si dipole-dipole interaction, which is able to transfer polarization from the ^{31}P under a resonant matching condition satisfied at 2.3 T and 6.7 T. We have proposed a phononic model for the electron-^{29}Si hyperfine interaction driven polarization process, and shown that the limiting step in this mechanism is the electron-^{29}Si cross-relaxation timescale. We have shown that the defect ionization and photoneutralization cycle driven by optical pumping modifies the spin diffusion process across the so-called diffusion barrier in the vicinity of the defect. Based on the ionization and

photoneutralization rates, we have calculated a lower bound on the diffusion rate under a classical diffusion model. Our analysis and experiments show that the ^{31}P-^{29}Si polarization transfer competes with the defect electron driven process at the 6.7 T matching condition, driving the ^{29}Si to a negative temperature, but is expected to drive the ^{29}Si to a positive spin temperature at 2.3 T, in the same direction as the electron driven polarization. The analysis also suggests that the efficiency of the ^{31}P-^{29}Si polarization transfer is a function of the electron spin-lattice relaxation time T_1^e, which is itself a function of laser power. While the rate of polarization under continuous, above-bandgap optical pumping are slow, the insight provided by our results suggests that a combination of electric field modulation and optical pumping may be used to optimize the rate and contribution of the two resources i.e. the electron and ^{31}P spins, and also minimize the effect of the spin diffusion barrier.

The experiments in this thesis have also further demonstrated the well known utility of inductively detected NMR as a highly sensitive probe of the local environment. In particular, we have performed a pump-probe type experiment with the ^{31}P nuclear spin to measure defect ionization and photoneutralization rates under optical pumping, as well as a previously unreported paramagnetic shift on the ^{31}P nuclear spin in the ionized (D^+) state. Our simulations show that with the addition of a magnetic field sweep, this approach may be able to measure the hyperfine interaction between the hole and ^{31}P nuclear spin. It will also allow us to extract bound exciton formation/recombination rates, as well as the efficiency of Auger electron driven impact ionizations. Finally, we have demonstrated, through preliminary measurements, that NMR can be used to measure the dependence of the ^{31}P hyperfine interaction on hydrostatic strain with high precision, induced by changes to the bath pressure. This measurement is sensitive to changes in strain of the order of 10^{-7}.

References

[1] K. Saeedi, S. Simmons, J. Z. Salvail, P. Dluhy, H. Riemann, N. V. Abrosimov, P. Becker, H.-J. Pohl, J. J. L. Morton, and M. L. W. Thewalt, "Room-temperature quantum bit storage exceeding 39 minutes using ionized donors in silicon-28," *Science*, vol. 342, pp. 830–833, Nov 2013.

[2] J. T. Muhonen, J. P. Dehollain, A. Laucht, F. E. Hudson, R. Kalra, T. Sekiguchi, K. M. Itoh, D. N. Jamieson, J. C. McCallum, A. S. Dzurak, and A. Morello, "Storing quantum information for 30 seconds in a nanoelectronic device," *Nature Nanotechnology*, vol. 9, pp. 986–991, Dec 2014.

[3] A. Ajoy and P. Cappellaro, "Stable three-axis nuclear-spin gyroscope in diamond," *Physical Review A*, vol. 86, p. 062104, Dec 2012.

[4] P. Gumann, O. Patange, C. Ramanathan, H. Haas, O. Moussa, M. Thewalt, H. Riemann, N. Abrosimov, P. Becker, H.-J. Pohl, K. Itoh, and D. Cory, "Inductive measurement of optically hyperpolarized phosphorous donor nuclei in an isotopically enriched silicon-28 crystal," *Physical Review Letters*, vol. 113, p. 267604, Dec 2014.

[5] A. S. Verhulst, I. G. Rau, Y. Yamamoto, and K. M. Itoh, "Optical pumping of ^{29}Si nuclear spins in bulk silicon at high magnetic field and liquid helium temperature," *Physical Review B*, vol. 71, Jun 2005.

[6] J. Mansir, P. Conti, Z. Zeng, J. J. Pla, P. Bertet, M. W. Swift, C. G. Van de Walle, M. L. W. Thewalt, B. Sklenard, Y. M. Niquet, and J. J. L. Morton, "Linear hyperfine tuning of donor spins in silicon using hydrostatic strain," *Physical Review Letters*, vol. 120, p. 167701, Apr 2018.

[7] P. Gumann, H. Haas, S. Sheldon, L. Zhu, R. Deshpande, T. Alexander, M. L. W. Thewalt, D. G. Cory, and C. Ramanathan, "NMR study of optically hyperpolarized phosphorus donor nuclei in silicon," *Physical Review B*, vol. 98, p. 180405, Nov 2018.

[8] H. M. McConnell, "Reaction rates by nuclear magnetic resonance," *The Journal of Chemical Physics*, vol. 28, no. 3, pp. 430–431, 1958.

[9] A. Abragam, *The principles of nuclear magnetism*. International series of monographs on physics, London: Oxford University Press, 1961.

[10] R. H. Dicke, "Discussion on, how does a crossed-coil nmr spectrometer work?," *Spectroscopy Letters*, vol. 1, pp. 415–419, Dec 1968.

[11] R. Annabestani, D. Cory, and J. Emerson, "Quantum model of spin noise," *Journal of Magnetic Resonance*, vol. 252, pp. 94 – 102, Mar 2015.

[12] D. Hoult and N. Ginsberg, "The quantum origins of the free induction decay signal and spin noise," *Journal of Magnetic Resonance*, vol. 148, pp. 182 – 199, Feb 2001.

[13] G. Lindblad, "On the generators of quantum dynamical semigroups," *Communications in Mathematical Physics*, vol. 48, no. 2, pp. 119–130, 1976.

[14] W. E. Roth, "On direct product matrices," *Bulletin of the American Mathematical Society*, vol. 40, pp. 461–468, Apr 1934.

[15] F. Bloch, "Nuclear induction," *Physical Review*, vol. 70, pp. 460–474, Oct 1946.

[16] J. H. Van Vleck, "The dipolar broadening of magnetic resonance lines in crystals," *Physical Review*, vol. 74, pp. 1168–1183, Nov 1948.

[17] J. Nečas and I. Hlaváček, "Generalized hooke's law," in *Mathematical Theory of Elastic and Elasto-Plastic Bodies*, vol. 3 of *Studies in Applied Mechanics*, pp. 41 – 55, Elsevier, 1981.

[18] G. L. Belen'kiĭ, É. Y. Salaev, and R. A. Suleĭmanov, "Deformation effects in layer crystals," *Soviet Physics Uspekhi*, vol. 31, pp. 434–455, May 1988.

[19] W. Voigt, *Lehrbuch der Kristallphysik*. Vieweg+Teubner Verlag, 1966.

[20] B. E. Kane, "A silicon-based nuclear spin quantum computer," *Nature*, vol. 393, pp. 133–137, May 1998.

[21] K. M. Itoh and H. Watanabe, "Isotope engineering of silicon and diamond for quantum computing and sensing applications," *MRS Communications*, vol. 4, p. 143–157, Nov 2014.

[22] B. Andreas, Y. Azuma, G. Bartl, P. Becker, H. Bettin, M. Borys, I. Busch, M. Gray, P. Fuchs, K. Fujii, H. Fujimoto, E. Kessler, M. Krumrey, U. Kuetgens, N. Kuramoto, G. Mana, P. Manson, E. Massa, S. Mizushima, A. Nicolaus, A. Picard, A. Pramann, O. Rienitz, D. Schiel, S. Valkiers, and A. Waseda, "Determination of the avogadro constant by counting the atoms in a ^{28}Si crystal," *Physical Review Letters*, vol. 106, p. 030801, Jan 2011.

[23] T. Sekiguchi, M. Steger, K. Saeedi, M. L. W. Thewalt, H. Riemann, N. V. Abrosimov, and N. Notzel, "Hyperfine structure and nuclear hyperpolarization observed in the bound exciton luminescence of Bi donors in natural Si," *Physical Review Letters*, vol. 104, Apr 2010.

[24] G. Pica, G. Wolfowicz, M. Urdampilleta, M. L. W. Thewalt, H. Riemann, N. V. Abrosimov, P. Becker, H.-J. Pohl, J. J. L. Morton, R. N. Bhatt, S. A. Lyon, and B. W. Lovett, "Hyperfine stark effect of shallow donors in silicon," *Physical Review B*, vol. 90, p. 195204, Nov 2014.

[25] T. Sekiguchi, A. M. Tyryshkin, S. Tojo, E. Abe, R. Mori, H. Riemann, N. V. Abrosimov, P. Becker, H.-J. Pohl, J. W. Ager, E. E. Haller, M. L. W. Thewalt, J. J. L. Morton, S. A. Lyon, and K. M. Itoh, "Host isotope mass effects on the hyperfine interaction of group-V donors in silicon," *Physical Review B*, vol. 90, p. 121203, Sep 2014.

[26] M. Cassidy, *Hyperpolarized Silicon Particles as In-vivo Imaging Agents*. Ph.D. thesis, Harvard University, 2012.

[27] T. F. Rosenbaum, R. F. Milligan, M. A. Paalanen, G. A. Thomas, R. N. Bhatt, and W. Lin, "Metal-insulator transition in a doped semiconductor," *Physical Review B*, vol. 27, pp. 7509–7523, Jun 1983.

[28] D. J. Lépine, "Spin resonance of localized and delocalized electrons in phosphorus-doped silicon between 20 and 30 °K," *Physical Review B*, vol. 2, pp. 2429–2439, Oct 1970.

[29] C. Kittel, *Introduction to Solid State Physics*. Wiley, 1996.

[30] W. Kohn and J. M. Luttinger, "Theory of donor states in silicon," *Physical Review*, vol. 98, pp. 915–922, May 1955.

[31] B. Koiller, X. Hu, and S. Das Sarma, "Exchange in silicon-based quantum computer architecture," *Physical Review Letters*, vol. 88, p. 027903, Dec 2001.

[32] C. J. Wellard and L. C. L. Hollenberg, "Donor electron wave functions for phosphorus in silicon: Beyond effective-mass theory," *Physical Review B*, vol. 72, p. 085202, Aug 2005.

[33] L. Greenman, H. D. Whitley, and K. B. Whaley, "Large-scale atomistic density functional theory calculations of phosphorus-doped silicon quantum bits," *Physical Review B*, vol. 88, p. 165102, Oct 2013.

[34] J. S. Smith, A. Budi, M. C. Per, N. Vogt, D. W. Drumm, L. C. L. Hollenberg, J. H. Cole, and S. P. Russo, "Ab initio calculation of energy levels for phosphorus donors in silicon," *Scientific Reports*, vol. 7, July 2017.

[35] G. Feher, "Nuclear polarization via "hot" conduction electrons," *Physical Review Letters*, vol. 3, pp. 135–137, Aug 1959.

[36] H. Haas, *Engineering Effective Hamiltonians for Magnetic Resonance*. Ph.D. thesis, University of Waterloo, 2019.

[37] A. Yang, H. Lian, M. Thewalt, M. Uemura, A. Sagara, K. Itoh, E. Haller, J. Ager, and S. Lyon, "Isotopic mass dependence of the lattice parameter in silicon determined by measurement of strain-induced splitting of impurity bound exciton transitions," *Physica B: Condensed Matter*, vol. 376-377, pp. 54 – 56, Apr 2006.

[38] G. Feher, J. P. Gordon, E. Buehler, E. A. Gere, and C. D. Thurmond, "Spontaneous emission of radiation from an electron spin system," *Physical Review*, vol. 109, pp. 221–222, Jan 1958.

[39] E. Hale, *An Investigation of Shallow Donor Impurities in Silicon by ENDOR*. Ph.D. thesis, Purdue University, 1968.

[40] G. Feher, "Donor wavefunctions in silicon by the ENDOR technique," *Journal of Physics and Chemistry of Solids*, vol. 8, p. 486, Jan 1959.

[41] E. B. Hale and R. L. Mieher, "Shallow donor electrons in silicon. I. Hyperfine interactions from ENDOR measurements," *Physical Review*, vol. 184, pp. 739–750, Aug 1969.

[42] J. Haase, N. Curro, and C. Slichter, "Double resonance probes for close frequencies," *Journal of Magnetic Resonance*, vol. 135, pp. 273–279, Dec 1998.

[43] M. E. Stoll, A. J. Vega, and R. W. Vaughan, "Simple single coil double resonance NMR probe for solid state studies," *Review of Scientific Instruments*, vol. 48, pp. 800–803, Mar 1977.

[44] T. Alexander, "Above bandgap hyperpolarization mechanism in isotopically purified silicon and optimal bayesian experiment design for T_1 estimation," Master's thesis, University of Waterloo, 2018.

[45] Y. Chen and S. Lyon, "Photoluminescence and diffusivity of free excitons in doped silicon," *IEEE Journal of Quantum Electronics*, vol. 25, pp. 1053–1055, May 1989.

[46] H.-Y. Hao and H. J. Maris, "Dispersion of the long-wavelength phonons in Ge, Si, GaAs, quartz, and sapphire," *Physical Review B*, vol. 63, p. 224301, May 2001.

[47] G. G. Macfarlane, T. P. McLean, J. E. Quarrington, and V. Roberts, "Fine structure in the absorption-edge spectrum of Si," *Physical Review*, vol. 111, pp. 1245–1254, Sep 1958.

[48] E. L. Hahn, "Spin echoes," *Physical Review*, vol. 80, pp. 580–594, Nov 1950.

[49] S. Meiboom and D. Gill, "Modified spin-echo method for measuring nuclear relaxation times," *Review of Scientific Instruments*, vol. 29, pp. 688–691, Jun 1958.

[50] R. Lefort, J. W. Wiench, M. Pruski, and J.-P. Amoureux, "Optimization of data acquisition and processing in Carr–Purcell–Meiboom–Gill multiple quantum magic angle spinning nuclear magnetic resonance," *The Journal of Chemical Physics*, vol. 116, pp. 2493–2501, Jan 2002.

[51] R. Siegel, T. T. Nakashima, and R. E. Wasylishen, "Signal-to-noise enhancement of NMR spectra of solids using multiple-pulse spin-echo experiments," *Concepts in Magnetic Resonance Part A*, vol. 26A, pp. 62–77, Jun 2005.

[52] D. R. McCamey, J. van Tol, G. W. Morley, and C. Boehme, "Fast nuclear spin hyperpolarization of phosphorus in silicon," *Physical Review Letters*, vol. 102, Jan 2009.

[53] P. Yu and M. Cardona, *Fundamentals of Semiconductors, Physics and Materials Properties, 4th edition.* Graduate Texts in Physics, Berlin: Springer-Verlag, 2010.

[54] R. B. Hammond and R. N. Silver, "Temperature dependence of the exciton lifetime in high-purity silicon," *Applied Physics Letters*, vol. 36, pp. 68–71, Jan 1980.

[55] M. Thewalt, "Details of the structure of bound excitons and bound multiexciton complexes in Si," *Canadian Journal of Physics*, vol. 55, pp. 1463–1480, Sep 1977.

[56] W. Schmid, "Auger lifetimes for excitons bound to neutral donors and acceptors in Si," *Physica Status Solidi (b)*, vol. 84, pp. 529–540, Dec 1977.

[57] A. S. Verhulst, *Optical Pumping Experiments to Increase the Polarization in Nuclear-spin based Quantum Computers*. Ph.D. thesis, Stanford University, 2005.

[58] K.-M. C. Fu, T. D. Ladd, C. Santori, and Y. Yamamoto, "Optical detection of the spin state of a single nucleus in silicon," *Physical Review B*, vol. 69, p. 125306, Mar 2004.

[59] A. Yang, M. Steger, T. Sekiguchi, M. L. W. Thewalt, J. W. Ager, and E. E. Haller, "Homogeneous linewidth of the ^{31}P bound exciton transition in silicon," *Applied Physics Letters*, vol. 95, p. 122113, Sep 2009.

[60] A. Schweiger and G. Jeschke, *Principles of Pulse Electron Paramagnetic Resonance*. Oxford University Press, 2001.

[61] G. Feher and E. A. Gere, "Electron spin resonance experiments on donors in silicon. II. Electron spin relaxation effects," *Physical Review*, vol. 114, pp. 1245–1256, Jun 1959.

[62] M. Nakayama and H. Hasegawa, "Relaxation effects on donor spins in silicon and germanium," *Journal of the Physical Society of Japan*, vol. 18, pp. 229–239, Feb 1963.

[63] D. Pines, J. Bardeen, and C. P. Slichter, "Nuclear polarization and impurity-state spin relaxation processes in silicon," *Physical Review*, vol. 106, pp. 489–498, May 1957.

[64] H. Breuer and F. Petruccione, *The Theory of Open Quantum Systems*. OUP Oxford, 2007.

[65] H. S. Gutowsky, D. W. McCall, and C. P. Slichter, "Nuclear magnetic resonance multiplets in liquids," *The Journal of Chemical Physics*, vol. 21, pp. 279–292, Feb 1953.

[66] H.-W. Hübers, S. G. Pavlov, S. A. Lynch, T. Greenland, K. L. Litvinenko, B. Murdin, B. Redlich, A. F. G. van der Meer, H. Riemann, N. V. Abrosimov, P. Becker, H.-J.

Pohl, R. K. Zhukavin, and V. N. Shastin, "Isotope effect on the lifetime of the $2p_0$ state in phosphorus-doped silicon," *Physical Review B*, vol. 88, p. 035201, Jul 2013.

[67] N. Q. Vinh, P. T. Greenland, K. Litvinenko, B. Redlich, A. F. G. van der Meer, S. A. Lynch, M. Warner, A. M. Stoneham, G. Aeppli, D. J. Paul, C. R. Pidgeon, and B. N. Murdin, "Silicon as a model ion trap: Time domain measurements of donor rydberg states," *Proceedings of the National Academy of Sciences*, vol. 105, pp. 10649–10653, Aug 2008.

[68] V. V. Tsyplenkov, K. A. Kovalevsky, and V. N. Shastin, "Effect of uniaxial stress on intervalley phonon-assisted relaxation of excited shallow-donor states in silicon," *Semiconductors*, vol. 43, p. 1410, Nov 2009.

[69] G. W. Morley, D. R. McCamey, H. A. Seipel, L.-C. Brunel, J. van Tol, and C. Boehme, "Long-lived spin coherence in silicon with an electrical spin trap read-out," *Physical Review Letters*, vol. 101, p. 207602, Nov 2008.

[70] A. Yang, M. Steger, T. Sekiguchi, M. L. W. Thewalt, T. D. Ladd, K. M. Itoh, H. Riemann, N. V. Abrosimov, P. Becker, and H.-J. Pohl, "Simultaneous subsecond hyperpolarization of the nuclear and electron spins of phosphorus in silicon by optical pumping of exciton transitions," *Physical Review Letters*, vol. 102, p. 257401, Jun 2009.

[71] J. Baugh, Y. Kitamura, K. Ono, and S. Tarucha, "Large nuclear overhauser fields detected in vertically coupled double quantum dots," *Physical Review Letters*, vol. 99, p. 096804, Aug 2007.

[72] S. Tarucha and J. Baugh, "Magnetic and electrical control of electron-nuclear spin coupling in GaAs double quantum dots," *Journal of the Physical Society of Japan*, vol. 77, pp. 031011–031011, Mar 2008.

[73] C. C. Lo, C. D. Weis, J. van Tol, J. Bokor, and T. Schenkel, "All-electrical nuclear spin polarization of donors in silicon," *Physical Review Letters*, vol. 110, p. 057601, Jan 2013.

[74] A. J. Sigillito, A. M. Tyryshkin, T. Schenkel, A. A. Houck, and S. A. Lyon, "All-electric control of donor nuclear spin qubits in silicon," *Nature Nanotechnology*, vol. 12, Oct 2017.

[75] S. Asaad, V. Mourik, B. Joecker, M. A. I. Johnson, A. D. Baczewski, H. R. Firgau, M. T. Mądzik, V. Schmitt, J. J. Pla, F. E. Hudson, K. M. Itoh, J. C. McCallum,

A. S. Dzurak, A. Laucht, and A. Morello, "Coherent electrical control of a single high-spin nucleus in silicon," *Nature*, vol. 579, pp. 205–209, Mar 2020.

[76] A. J. Sigillito, A. M. Tyryshkin, and S. A. Lyon, "Anisotropic stark effect and electric-field noise suppression for phosphorus donor qubits in silicon," *Physical Review Letters*, vol. 114, p. 217601, May 2015.

[77] F. A. Zwanenburg, A. S. Dzurak, A. Morello, M. Y. Simmons, L. C. L. Hollenberg, G. Klimeck, S. Rogge, S. N. Coppersmith, and M. A. Eriksson, "Silicon quantum electronics," *Rev. Mod. Phys.*, vol. 85, pp. 961–1019, Jul 2013.

[78] P. Dluhy, J. Z. Salvail, K. Saeedi, M. L. W. Thewalt, and S. Simmons, "Switchable resonant hyperpolarization transfer to ^{29}Si spins in natural silicon," *Physical Review B*, vol. 91, p. 195206, May 2015.

[79] M. Niknam, *Dynamics of Quantum Information of the Central Spin Problem*. Ph.D. thesis, University of Waterloo, 2018.

[80] M. Mirkamali, *Resources Needed for Entangling Two Qubits through an Intermediate Mesoscopic System*. Ph.D. thesis, University of Waterloo, 2019.

[81] M. C. Cassidy, H. R. Chan, B. D. Ross, P. K. Bhattacharya, and C. M. Marcus, "In vivo magnetic resonance imaging of hyperpolarized silicon particles," *Nature Nanotechnology*, vol. 8, pp. 363 EP –, May 2013.

[82] N. Whiting, J. Hu, N. M. Zacharias, G. L. R. Lokesh, D. E. Volk, D. G. Menter, R. Rupaimoole, R. Previs, A. K. Sood, and P. Bhattacharya, "Developing hyperpolarized silicon particles for in vivo MRI targeting of ovarian cancer," *Journal of Medical Imaging*, vol. 3, pp. 1 – 9, Aug 2016.

[83] K. M. Itoh, "An all-silicon linear chain NMR quantum computer," *Solid State Communications*, vol. 133, pp. 747 – 752, Mar 2005.

[84] S. Takahashi, R. Hanson, J. van Tol, M. S. Sherwin, and D. D. Awschalom, "Quenching spin decoherence in diamond through spin bath polarization," *Physical Review Letters*, vol. 101, p. 047601, Jul 2008.

[85] G. Lampel, "Nuclear dynamic polarization by optical electronic saturation and optical pumping in semiconductors," *Physical Review Letters*, vol. 20, pp. 491–493, Mar 1968.

[86] G. R. Khutsishvili, "Spin diffusion," *Soviet Physics Uspekhi*, vol. 8, pp. 743–769, May 1966.

[87] G. W. Leppelmeier and J. Jeener, "Measurement of the nuclear spin diffusion coefficient in CaF_2," *Physical Review*, vol. 175, pp. 498–502, Nov 1968.

[88] J. V. Gates and W. H. Potter, "Measurement of the spin-diffusion constant in caf_2," *Physical Review B*, vol. 15, pp. 4143–4148, May 1977.

[89] W. Zhang and D. G. Cory, "First direct measurement of the spin diffusion rate in a homogenous solid," *Physical Review Letters*, vol. 80, pp. 1324–1327, Feb 1998.

[90] B. Christensen and J. Price, "NMR line shape of ^{29}Si in single-crystal silicon," *Physical Review B*, vol. 95, Apr 2017.

[91] H. Hayashi, K. M. Itoh, and L. S. Vlasenko, "Nuclear magnetic resonance linewidth and spin diffusion in ^{29}Si isotopically controlled silicon," *Physical Review B*, vol. 78, p. 153201, Oct 2008.

[92] H. Hayashi, T. Itahashi, K. M. Itoh, L. S. Vlasenko, and M. P. Vlasenko, "Dynamic nuclear polarization of ^{29}Si nuclei in isotopically controlled phosphorus doped silicon," *Physical Review B*, vol. 80, p. 045201, Jul 2009.

[93] J. Crank, *The Mathematics of Diffusion*. Oxford science publications, Clarendon Press, 1979.

[94] N. Bloembergen, "On the interaction of nuclear spins in a crystalline lattice," *Physica*, vol. 15, pp. 386 – 426, May 1949.

[95] J. Ramakrishna and F. N. H. Robinson, "A transient effect in dynamic nuclear polarization," *Proceedings of the Physical Society*, vol. 87, pp. 945–951, Apr 1966.

[96] T. J. Schmugge and C. D. Jeffries, "High dynamic polarization of protons," *Physical Review*, vol. 138, pp. A1785–A1801, Jun 1965.

[97] D. Tse and I. J. Lowe, "Nuclear spin-lattice relaxation in CaF_2 crystals via paramagnetic centers," *Physical Review*, vol. 166, pp. 292–302, Feb 1968.

[98] A. R. King, J. P. Wolfe, and R. L. Ballard, "NMR of nuclei near a paramagnetic impurity in crystals," *Physical Review Letters*, vol. 28, pp. 1099–1102, Apr 1972.

[99] C. Ramanathan, "Dynamic nuclear polarization and spin diffusion in nonconducting solids," *Applied Magnetic Resonance*, vol. 34, p. 409, Aug 2008.

[100] W. M. Itano, D. J. Heinzen, J. J. Bollinger, and D. J. Wineland, "Quantum Zeno effect," *Physical Review A*, vol. 41, pp. 2295–2300, Mar 1990.

[101] J. S. Waugh, L. M. Huber, and U. Haeberlen, "Approach to high-resolution NMR in solids," *Physical Review Letters*, vol. 20, pp. 180–182, Jan 1968.

[102] A. M. Tyryshkin, S. A. Lyon, A. V. Astashkin, and A. M. Raitsimring, "Electron spin relaxation times of phosphorus donors in silicon," *Physical Review B*, vol. 68, p. 193207, Nov 2003.

[103] Y. Hovav, I. Kaminker, D. Shimon, A. Feintuch, D. Goldfarb, and S. Vega, "The electron depolarization during dynamic nuclear polarization: measurements and simulations," *Physical Chemistry Chemical Physics*, vol. 17, pp. 226–244, 2015.

[104] M. Ha, A. N. Thiessen, I. V. Sergeyev, J. G. Veinot, and V. K. Michaelis, "Endogenous dynamic nuclear polarization NMR of hydride-terminated silicon nanoparticles," *Solid State Nuclear Magnetic Resonance*, vol. 100, pp. 77 – 84, Aug 2019.

[105] A. Laucht, J. T. Muhonen, F. A. Mohiyaddin, R. Kalra, J. P. Dehollain, S. Freer, F. E. Hudson, M. Veldhorst, R. Rahman, G. Klimeck, K. M. Itoh, D. N. Jamieson, J. C. McCallum, A. S. Dzurak, and A. Morello, "Electrically controlling single-spin qubits in a continuous microwave field," *Science Advances*, vol. 1, Apr 2015.

[106] D. K. Wilson and G. Feher, "Electron spin resonance experiments on donors in silicon. III. Investigation of excited states by the application of uniaxial stress and their importance in relaxation processes," *Physical Review*, vol. 124, pp. 1068–1083, Nov 1961.

[107] J. J. Pla, A. Bienfait, G. Pica, J. Mansir, F. A. Mohiyaddin, Z. Zeng, Y. M. Niquet, A. Morello, T. Schenkel, J. J. L. Morton, and P. Bertet, "Strain-induced spin-resonance shifts in silicon devices," *Physical Review Applied*, vol. 9, p. 044014, Apr 2018.

[108] L. Zhang, R. Barrett, P. Cloetens, C. Detlefs, and M. Sanchez del Rio, "Anisotropic elasticity of silicon and its application to the modelling of X-ray optics," *Journal of Synchrotron Radiation*, vol. 21, pp. 507–517, May 2014.

[109] F. Seglenieks, "University of waterloo weather station data archives," 2018.

[110] M. Steger, T. Sekiguchi, A. Yang, K. Saeedi, M. E. Hayden, M. L. W. Thewalt, K. M. Itoh, H. Riemann, N. V. Abrosimov, P. Becker, and H.-J. Pohl, "Optically-detected NMR of optically-hyperpolarized ^{31}P neutral donors in ^{28}Si," *Journal of Applied Physics*, vol. 109, p. 102411, May 2011.

[111] P. Hertz, "Uber den gegenseitigen durchschnittlichen abstand von punkten, die mit bekannter mittlerer dichte im raume angeordnet sind," *Mathematische Annalen*, vol. 67, pp. 387–398, Sep 1909.

[112] S. Chandrasekhar, "Stochastic problems in physics and astronomy," *Reviews of Modern Physics*, vol. 15, pp. 1–89, Jan 1943.

Appendix A

Nearest Neighbour Distances

In this appendix, we derive the nearest neighbour distance distributions for various nuclear species in the sample.

A.1 The Nearest Neighbour Distribution

The continuous probability density function for the nearest neighbour, given a uniform random distribution of a particle in three dimensions, was first derived by Hertz [111](publication in German). A complete derivation in English was given by Chandrasekhar [112]. The crux of it is as follows: Given a particle at origin, an average number of particles per unit volume N_c and a probability density function $w(r)$, the probability that the nearest neighbour occurs between r and $r+dr$, given by $w(r)dr$, must be equal to the product of a) the probability that no other particle occurs between the origin and r, which is $\left(1-\int_0^r w(r')dr'\right)$ and b) the probability that a particle is present in the spherical shell between r and $r+dr$, which is $4\pi r^2 dr N_c$. Therefore,

$$w(r)dr = \left(1-\int_0^r w(r')dr'\right) 4\pi r^2 dr N_c \ . \tag{A.1}$$

This equation may be recast into a differential equation, with the normalized solution $\left(\int_0^\infty w(r)dr = 1\right)$ given by

$$w(r) = 4\pi r^2 N_c \exp\left(-\frac{4}{3}\pi r^3 N_c\right) \ . \tag{A.2}$$

The average distance to the nearest neighbour, given by $\int_0^\infty r w(r)dr$, can be calculated as

$$\begin{aligned} \langle r\rangle &= 6^{-\frac{2}{3}}\pi^{-\frac{1}{3}}\Gamma\left(1/3\right) N_c^{-\frac{1}{3}} \\ &\simeq 0.554 N_c^{-\frac{1}{3}} \ , \end{aligned} \tag{A.3}$$

where $\Gamma(z) = \int_0^\infty x^{z-1}e^{-x}dx$ is the gamma function, and $\Gamma(1/3) \simeq 2.679$. Substituting $N_c = 1.5 \times 10^{15}$ cm^{-3} for the ^{31}P doping concentration in the isotopically enriched sample, we get $\langle r \rangle_{\mathrm{P}} = 48.393$ nm. Similarly, for the ^{31}P doping concentration of $N_c = 6 \times 10^{15}$ cm^{-3} in the natural abundance sample, we get $\langle r \rangle_{\mathrm{P}} = 30.486$ nm. For the ^{29}Si in the sample with 4.7 % natural abundance ($N_c = 2.35 \times 10^{21}$ cm^{-3}), we get $\langle r \rangle_{\mathrm{Si}} = 0.417$ nm, and for the isotopically purified sample with 46 ppm abundance ($N_c = 2.3 \times 10^{18}$ cm^{-3}), $\langle r \rangle_{\mathrm{Si}} = 4.197$ nm. We note that the average distance is the same irrespective of which particle we place at the origin i.e the mean distance to the nearest ^{29}Si is $\langle r \rangle_{\mathrm{Si}}$ for both ^{29}Si and ^{31}P, and the mean distance to the nearest ^{31}P is $\langle r \rangle_{\mathrm{P}}$ for both ^{29}Si and ^{31}P as well.

The nearest neighbour distribution function assumes a continuous set of possible positions, which is not true since the crystal structure only allows for a discrete set of positions for the nuclei. This is not expected to be an issue for calculating distances to the nearest ^{31}P defects in natural abundance or for any inter-nuclear spacing in the isotopically enriched ^{28}Si sample, which are much greater than the distance between adjacent atoms (0.235 nm) in the crystal. However, the average distance to the nearest ^{29}Si, as calculated from Eq. A.2 is 0.417 nm, which is comparable to this inter-atomic spacing. In the next section, we will compute the nearest neighbour distances more accurately by numerical simulation of the discrete crystal structure.

A.2 The Discrete Distribution for Silicon

Silicon has a diamond cubic crystal structure, similar to diamond and germanium. This is not a lattice in the mathematical sense, and can be thought of as a pair of intersecting face-centered cubic (FCC) lattices, with their origins separated by 1/4 of the unit cell width in each dimension. Therefore, we can write it mathematically with a set of primitive vectors and a two point basis. The primitive lattice vectors are given by

$$\vec{a}_1 = \frac{a_0}{2}(0,1,1) \ , \qquad \vec{a}_2 = \frac{a_0}{2}(1,0,1) \ , \qquad \vec{a}_3 = \frac{a_0}{2}(1,1,0) \ , \tag{A.4}$$

and the basis points are $(0,0,0)$ and $\frac{a_0}{4}(1,1,1)$, where $a_0 = 0.543$ nm is the lattice constant. Therefore, for a $N \times N \times N$ lattice, the set of the distance of lattice points from the origin

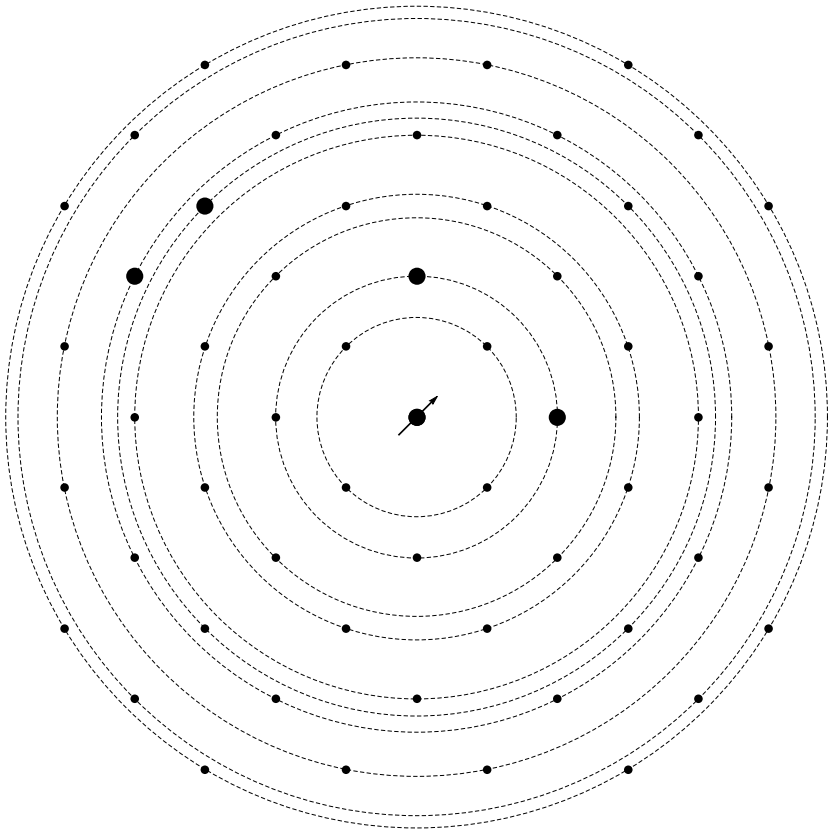

Figure A.1: Concentric shells in a 2D slice of the silicon crystal structure, assuming a ^{31}P at origin (indicated by arrow). Large dots elsewhere indicate neighbouring nuclei, generated assuming a uniform probability p = 0.047 at each lattice site, corresponding to the ^{29}Si distribution in natural abundance silicon

is generated by

$$\left\{ \frac{a_0}{\sqrt{2}} \left(\sqrt{ij+ik+jk+i^2+j^2+k^2}, \sqrt{\frac{3}{4}+i+j+k+ij+ik+jk+i^2+j^2+k^2} \right) \right. \tag{A.5}$$
$$\left. \mid \{i,j,k\} \in \left\{ -\frac{N-1}{2}, ..., \frac{N-1}{2} \right\} \right\}$$

This may be generated with Mathematica, with a $800 \times 800 \times 800$ lattice requiring $\sim$ 8 GB memory. We can divide the lattice into concentric shells by counting sets of equidistant points, as shown in Fig. A.1. This gives us a discrete set of possible distances $\{r_i\}$ and the number of atoms in the corresponding shell $\{n_i\}$. In order to calculate the nearest neighbour distances, we use a slightly different line of reasoning compared to that

in the derivation of Eq. A.1. Assuming that the first particle sits at the lattice point at origin, and a uniform probablity p_0 that any given lattice site has a particle, the probability that the nearest particle to the one at origin is in a specific shell j must be equal to the difference in the probability that there is no particle in all shells upto the $j-1^{\text{th}}$ shell and the probability that there is no particle in all the shells upto the j^{th} shell. Therefore,

$$p(r_j) = (1-p_0)^{\sum_{i=1}^{j-1} n_i} - (1-p_0)^{\sum_{i=1}^{j} n_i} \tag{A.6}$$

The validity of the infinite lattice assumption can be verified by checking that $\sum_j p(r_j) = 1$. With the $800 \times 800 \times 800$ lattice, we verified that this is true for the lowest doping concentration in our samples (1.5×10^{15} cm^{-3}). The probability p_0 can be calculated from the doping concentration N_c as

$$p = \frac{N_c M_{\text{Si}}}{\rho_{\text{Si}} N_{\text{A}}} \tag{A.7}$$

where M_{Si} is the atomic mass of silicon, ρ_{Si} is the density and N_{A} is the Avogadro constant. In case of isotopic abundance (% or ppm), p_0 is trivially equal to the abundance.

With this simulation, the distances can be calculated to be $\langle r \rangle_{\text{P}} = 30.444$ nm and $\langle r \rangle_{\text{Si}} = 0.433$ nm for the natural abundance sample and $\langle r \rangle_{\text{P}} = 48.328$ nm, $\langle r \rangle_{\text{Si}} = 4.198$ nm for the ^{28}Si enriched sample. The agreement with the values from the previous section is high for the longer distances. This is expected, since the continuous distribution is a good approximation at these scales and the $800 \times 800 \times 800$ lattice size is also large enough to approximate an infinite lattice. On the other hand, the value of $\langle r \rangle_{\text{Si}} = 0.433$ nm for natural abundance silicon is expected to be more accurate since the continuous distribution assumption is not justified at these length scales. Therefore, we use the numerically computed values from this section in the thesis.